Plasma density structures in the polar-cap ionosphere during magnetic storms

A dissertation for the degree of PhD in Science

Jun Sakai

Graduate School of Informatics and Engineering

The University of Electro-Communications

March 2014

Plasma density structures in the polar-cap ionosphere during magnetic storms

Screening Committee:

Chief Examiner: Prof. Satoshi Taguchi

Members: Associate Prof. Keisuke Hosokawa

Prof. Kazuhiko Honjo

Prof. Yoshio Karasawa

Prof. Masahisa Yanagisawa

磁気嵐に伴う極冠電離圏でのプラズマ密度構造に関する研究

坂井　純

概要

磁気嵐は、太陽活動の過渡的な変動に起因し、地球の超高層大気に巨大なエネルギーが注入されて発生する現象である。本論文では極冠電離圏に発生するプラズマ密度構造と磁気嵐の関係について考究する。

第 1 章では極冠を含む高緯度電離圏と磁気嵐の基礎的かつ特徴的な事項を整理する。第 2 章では 2000 年 10 月 14 日に発生した磁気嵐中に極冠域昼側で観測された急激な電子密度変動について、その発生に惑星間空間磁場の東西成分の変動が関与しているという先行研究での仮説への観測的証拠を初めて示した。第 3 章では、極冠域を移動するプラズマ密度構造（極冠パッチ）に伴う赤色大気光の発光強度と磁気嵐の関係について考察し、磁気嵐時には、発光高度の上昇、発光層の厚さの増加、発光強度の増加が見られることを示す。第 4 章では研究全体を総括し、今後の展望を述べる。

Abstract

The polar-cap ionosphere is directly coupled with the magnetosphere, which makes the region unique compared with the low- and mid-latitude ionosphere. Because of this coupling with the magnetosphere, the polar cap ionosphere is disturbed during magnetic storms. In this thesis, we examine ionospheric plasma density structures in the polar cap during magnetic storms. In Chapter 1, after reviewing the solar-terrestrial environment in general, we present some important features of the polar upper atmosphere and ionosphere with special attention to magnetic storms. Following this general introduction, Chapters 2 and 3 are dedicated to specific researches.

In Chapter 2, *Steep plasma depletion in dayside polar cap during a CME-driven magnetic storm*, we investigate a horizontal structure of dayside polar cap ionosphere during a magnetic storm. A series of steep plasma depletions was observed in the dayside polar cap during an interval of highly enhanced electron density on 14 October 2000 through EISCAT Svalbard Radar (ESR) field-aligned measurements and northward-directed low-elevation measurements. Each depletion started with a steep dropoff to as low as 10^{11} m^{-3} from the enhanced level of $\sim 3 \times 10^{12}$ m^{-3} at F2 region altitudes, and it continued for 10–15 min before returning to the enhanced level. These depletions moved poleward at a speed consistent with the observed ion drift velocity. DMSP spacecraft observations over an extended period of time which includes the interval of these events indicate that a region of high ion densities extended into the polar cap from the equatorward side of the cusp, i.e., a tongue of ionization existed, and that the ion densities were very low on its prenoon side. Solar wind observations show that

a sharp change from IMF $B_Y > 0$ to $B_Y < 0$ is associated with each appearance of the ESR electron density dropoff. These facts present the first observational evidence for some of the previously speculated theories on patch formation. In addition, we propose a scenario that the series of plasma density depletions is a result of the poleward drift of the undulating boundary of the tongue of ionization; this undulating boundary is created in the cusp roughly 20 min before the ESR observation by the azimuthal intrusion, in response to the rapid prenoon shift of the footprint of the reconnection line, of the low-density plasmas originating in the morning sector.

In Chapter 3, *Storm-time enhancements of 630.0-nm airglow associated with polar cap patches*, we study the vertical structures of both neutral and ionized gases in the polar cap. We examined the brightness of 630.0-nm airglow, I_{630}, associated with polar cap patches observed during a magnetic storm that occurred on 22 January 2012. Brightness was measured using an all sky imager (ASI) located at Longyearbyen, Svalbard. The observed I_{630} was compared with the F-region electron density observed by the EISCAT Svalbard Radar (ESR). The I_{630} was positively correlated with the F2-layer peak electron density, NmF2, and inversely correlated with the altitude of the F2-layer peak electron density, hmF2, as expected from the known relationship between these parameters. To estimate the altitude of the peak emission of the airglow, we performed model calculations of the volume emission rate, V_{630}, under quiet and disturbed conditions, using MSIS-modelled neutral gas profiles and the electron density profile obtained from the ESR data. In order to validate the V_{630} calculation, I_{630} was calculated by integrating the V_{630} along altitude, and then compared with the ASI-observed I_{630}. During the observation periods the measured brightness frequently exceeded the calculated I_{630}; we infer that, in most cases, low energy particle precipitation is responsible for the extra brightness. However, when there was less particle precipitation, the observed values were in good agreement with the calculated values. Under the magnetically disturbed conditions during our observations, the model calculation showed that the altitude of V_{630} peak increases, the thickness of the emission

layer increases, and patch brightness increases. The results clearly show the previously unknown vertical structure of polar-patch airglow under magnetic storms.

Acknowledgements

The author wishes to express his sincere thanks to Prof. Satoshi Taguchi at The University of Electro-communications (UEC) for his kind supervision and valuable suggestions throughout the whole process of this work. The author also wishes to express his thanks to Prof. Keisuke Hosokawa at UEC for his thorough guidance to the science of polar cap ionosphere. The author would like to thank Prof. Kazuhiko Honjo at UEC for his continued encouragement to the author to complete this work. The author is grateful to Prof. Yasunobu Ogawa at National Institute of Polar Research for his continuous support and experienced suggestions to IS radar data. The optical data used in this thesis were obtained from the instrument that was made through the research supported by JSPS KAKENHI Grant Number (B) 22340143.

Contents

Preliminaries

The polar-cap ionosphere is directly coupled with the magnetosphere, which makes the region unique compared with the low- and mid-latitude ionosphere. In this thesis we examine plasma density structures in the polar cap ionosphere during magnetic storms. One of the most important features in the polar-cap ionosphere is ionospheric convection (detailed in 1.4.1) of which a flow transports plasma structures from the dayside to the nightside of the polar cap. During a magnetic storm, the convection flow is accelerated and the structuring of plasma density becomes significant. As a result, a number of transient or localized phenomena are observed in the polar-cap ionosphere during magnetic storms. Although the effects of magnetic storms on the ionosphere have been studied for decades, these transient or localized phenomena have not been well understood. In this thesis, we study two distictive features of plasma structures, one in the dayside and the other in the night-side of the polar cap, during magnetic storms. In this chapter, after reviewing the solar-terrestrial environment in general, we present some important features of the polar upper atmosphere and ionosphere with special attention to magnetic storms. The aims of two separate studies in this thesis are briefly described in 1.5. Following this general introduction, Chapters 2 and 3 are dedicated to specific researches.

In Chapter 2, we investigate a horizontal structure of dayside polar cap ionosphere during a magnetic storm. A series of steep plasma depletions was observed in the dayside polar cap during an interval of highly enhanced electron density through EISCAT Svalbard Radar (ESR) measurements. Each depletion started with a steep decrease of

electron density at F2 region altitudes, and it continued for 10–15 min before returning to the enhanced level. These depletions moved poleward at a speed consistent with the observed ion drift velocity. DMSP spacecraft observations indicate that a region of high ion densities extended into the polar cap from the equatorward side of the cusp, and that the ion densities were very low on its prenoon side. Solar wind observations show that a sharp changes in interplanetary magnetic field (IMF) B_Y polarity is associated with an sharp decrease of electron density. These facts present the first observational evidence for some of the previously speculated theories on patch formation.

In Chapter 3, we study the vertical structures of both neutral and ionized gases in the polar cap. We examined the brightness of 630.0-nm airglow, I_{630}, associated with polar cap patches observed during a magnetic storm using an all sky imager (ASI) in Svalbard. The observed I_{630} showed a good correlation with the F-region electron density observed by ESR. To estimate the brightness and the altitude of the airglow, we performed model calculations of the volume emission rate, V_{630}, under quiet and disturbed conditions, using MSIS-modelled neutral gas profiles and the electron density profile obtained from the ESR data. The calculations revealed that, under disturbed conditions, (1) the altitude of V_{630} peak is increased, (2) the thickness of the emission layer is increased, and (3) the magnitude of V_{630} peak is increased. The results clearly show the previously unknown vertical structure of polar-patch airglow under magnetic storms.

These two studies will not only enrich our understanding of polar cap ionosphere but also add important basis for further studies. The scope of current and future studies is briefly introduced in 1.5, and fully described in Chapter 4.

Chapter 1

Introduction

1.1 An overview of the Earth's space environment

1.1.1 Solar wind and inter-planetary magnetic field

The Sun emits energy in the form of electromagnetic radiation as well as material transportation. The former includes a wide range of spectrum from very low-frequency radio waves to extremely high-frequency, hence high-energy, gamma rays. The latter involves a high-speed plasma flow called the *solar wind*. Although each form of the energy transfer is responsible for the various processes which affect the Earth's environment including the upper atmosphere and the magnetosphere, the solar wind plays a dominant role in the formation of short-term, and sometimes severe, geophysical phenomena.

The solar wind plasma consists of electrons and positive ions; ions are mainly protons, but about 5% are Helium ions. The speed of the solar wind is typically about 500 km/s, but it may vary between 300 km/s and 1500 km/s depending on the solar activity. At the orbit of the Earth, the density and temerature of the solar wind electons are $N_e \approx 5 \times 10^6$ m^{-3} and $T_e \approx 10^5$ K (~ 10 eV), respectively.

The solar-wind plasma is fully ionized and therefore electrically highly conductive. According to magnetohydrodynamics (MHD), a flow of high-conductivity plasma car-

ries magnetic field drawn from its origin; the resulting field is called *frozen-in magnetic field*. The solar wind brings the solar magnetic field out into the interplanetary space and the field is called the *interplanetary magnetic field (IMF)*. The strength of the IMF at the orbit of the Earth is typically a few nanotesla (nT), but it may extend upto a few tens of nT. One of the frequently-used coordinate systems to measure the IMF is called the *geocentric solar magnetospheric (GSM) system*. The GSM system has its x-axis along the line which connects the Earth and the Sun, with the positive axis directs toward the Sun. The y-axis is perpendicular to the x-axis and to the Earth's magnetic dipole, with the positive axis direct toward the east (evening). The z-axis is perpendicular to both the x- and y- axes and the positive z-axis is in the same sense as the northern magnetic pole.

1.1.2 Earth's magnetosphere

The Earth has its own magnetic field (the *main field*) which is approximately a dipole field with its magnetic south pole located near the North Pole. The main field and the IMF interact with each other and form the *magnetosphere*, which is a region around the Earth where the solar wind can not penetrate directly. The magnetosphere sheilds the near-earth environment from the high-energy particle flow of the solar wind. Figure 1.1 schematically illustrates the structure of the magnetosphere. Some important features in connection with this thesis are summarized below.

Bow shock. As the solar wind is a supersonic flow, a shock front, called the *bow shock*, is formed in front of the Earth; the distance from the Earth to the bow shock is $\sim$13 R_E toward the Sun, where R_E denotes the radius of the Earth. There are discontinuous changes in the properties of the solar wind and the IMF at this position.

Magnetopause. The *magnetopause* is a boundary surface within which the Earth's magnetic field is confined. At $\sim 10R_E$ from the Earth on the Sun-Earth line, the solar-

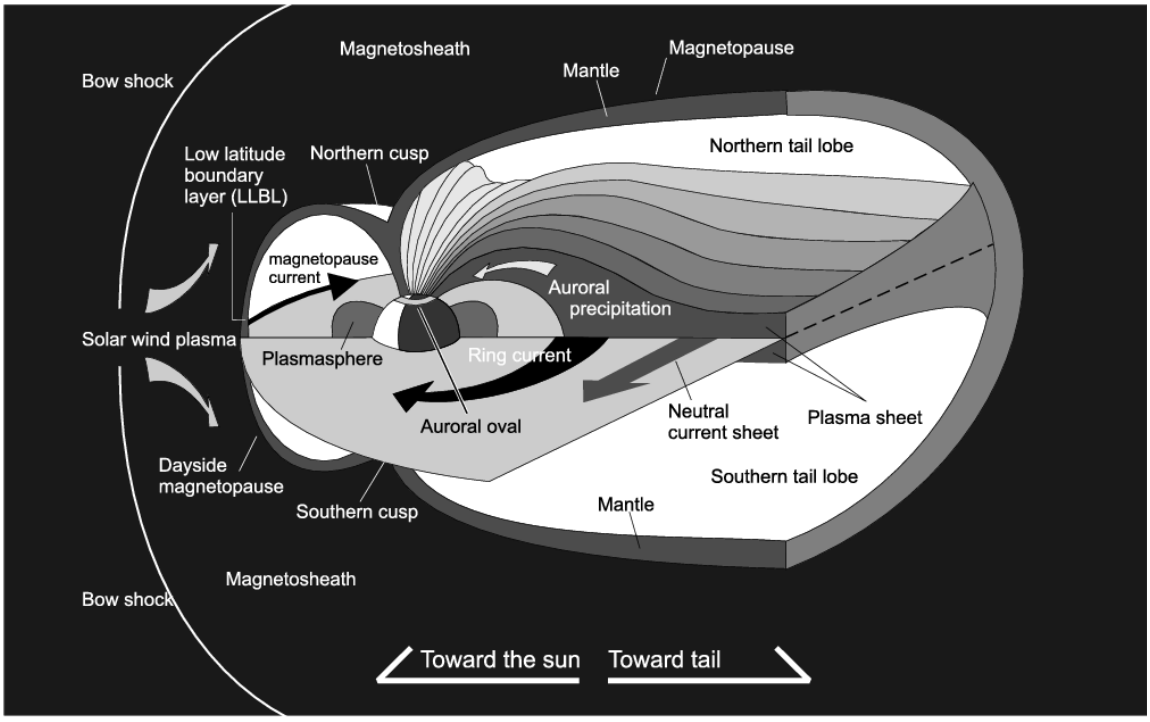

Figure 1.1: Schematic illustration of the magnetosphere seen from the evening side of the earth. (Courtesy of Keisuke Hosokawa.)

wind pressure and the magnetic pressure of the Earth's magnetic field are balanced. This point is called the *stagnation point* and is on the magnetopause surface. The region between the bow shock and the magnetopause is called the *magnetosheath*.

Open and closed field lines. A magnetic field line which has two footprints on the surface of the Earth is called the *closed (magnetic) field line*. The field lines of an ordinary dipole field is closed, except for the field line paralell to the dipole moment vector. A field line which has only one footprint on the surface of the Earth is called the *open field line*; the other end of the field line is connected to the IMF. Open field lines occur in the polar regions (see 1.2.3) as a result of *dayside reconnection*, or *field line merging* [*Dungey*, 1961], when the IMF is southward.

Cusp regions. The *magnetospheric cusp* is a region in the magnetosphere where a transition from closed field lines to open field lines occurs. The *ionospheric cusp* is a region onto which the magnetospheric cusp is mapped along the field liens. The

magnetospheric cusp is a unique region in the magnetosphere because the high energy solar wind particles are able to enter this region directly. These particles then move down to the ionospheric cusp along the field lines (*cusp precipitation*). As a result, particles whose energy is comparable to the magnetosheath particles are often observed in the ionospheric cusp region.

1.2 Polar upper atmosphere

1.2.1 Structure of the Earth's upper atmosphere

The vertical structure of the Earth's atmosphere can be classified in several ways. Widely used classification methods are (a) by temperature profile, (b) by vertical transport profile, and (c) by composition profile [*Rishbeth and Garriot*, 1969; *Prölss*, 2003]. These classifications and nomenclature are summarized in Figure 1.2. In these systems, the regions are named with a suffix *-sphere* and their upper boundaries are named with a suffix *-pause* [*Chapman*, 1950]; for example, in the system which classifies the atmosphere by temparature profile, the lowest region is called the *troposphere* and its upper boundary is called the *tropopause*.

The state of the Earth's neutral atmospheric gas is described by its pressure, temperature, density, composition, and bulk-drift velocity. In this section we describe the altitude profiles of temperature and number densities of constituent gases.

Starting from the surface of the Earth, atmospheric temperature gradually decreases with altitude from the ground temperature of $\sim$ 300 K. At about 10 km (the tropopause) the temperature records minimum and it begins to increase until the altitude reaches $\sim$ 50 km (the stratopause). Above the stratopause, the temperature decreases again before reaching $\sim$80-90 km (the mesopause). The region above the mesopause is called the thermosphere where the temperature increases steeply upto about 300 km, and more gradually above that altitude.

The behavior of the atmospheric gases above $\sim$100 km is significantly different from

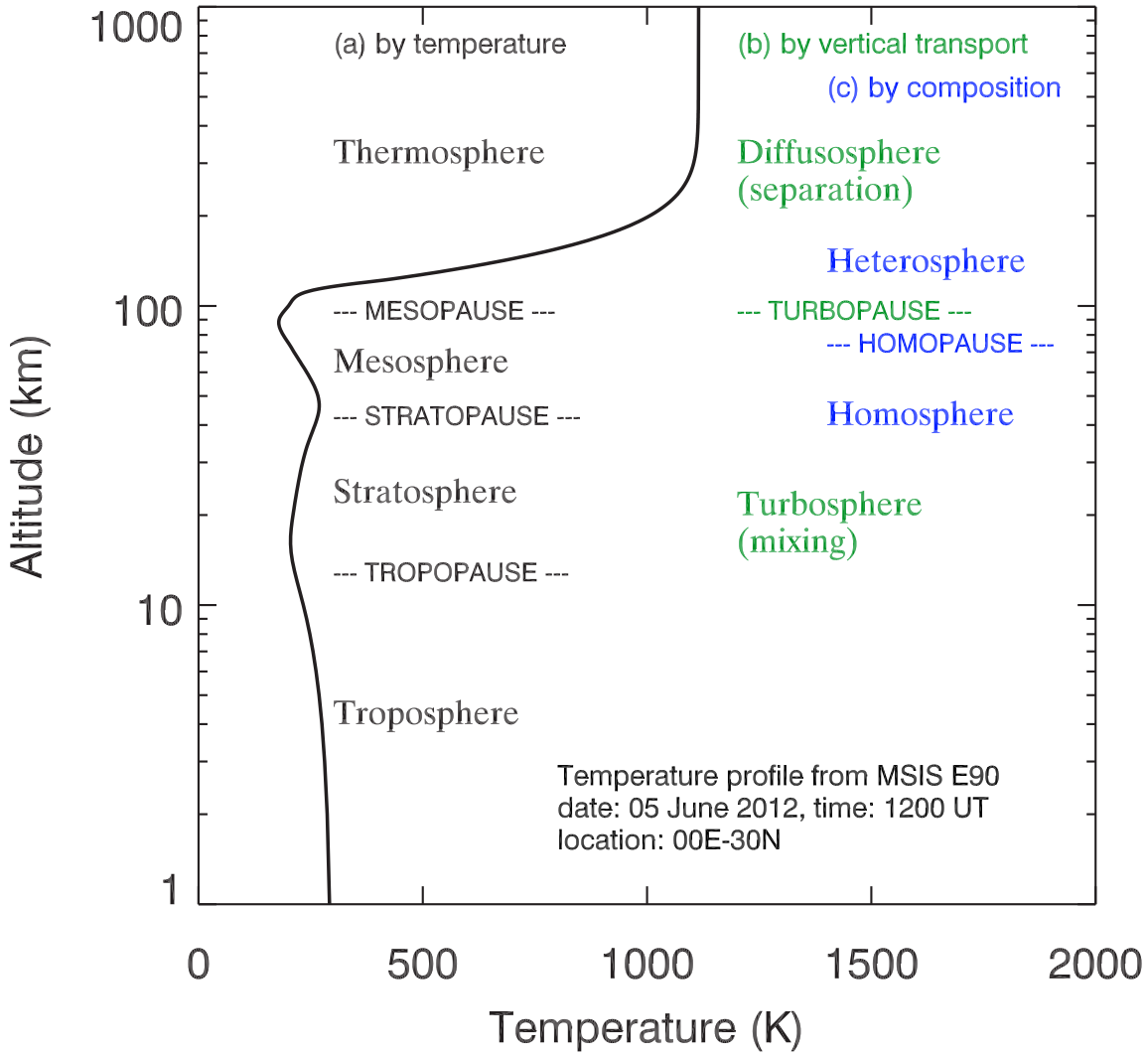

Figure 1.2: Vertical structure of the Earth's neutral atmosphere.

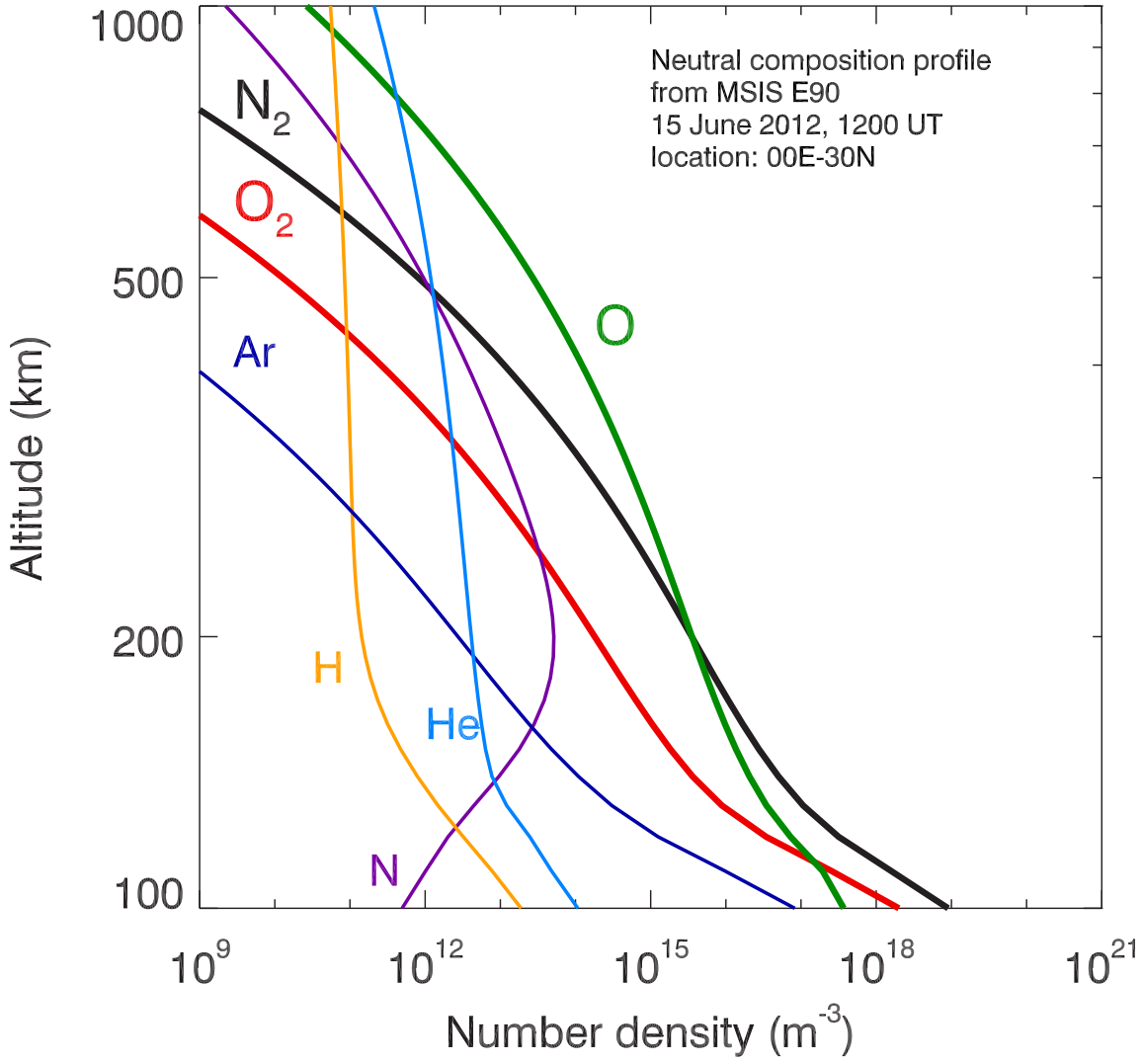

Figure 1.3: Composition profile of the neutral atmosphere.

the one below ∼100 km. At lower altitudes, the gases are well mixed by turbulance and behave like a single gas. At higher altitudes, species are no more mixed and each constituent gas behaves separately. The boundary is called the *turbopause* and the region below this boundary is called the *turbosphere*. The boundary is also called the *homopause* because the mixing ceases at this level. The region below the homopause is called the *homosphere*, and the region above homopause is called the *heterosphere*.

In this thesis our focus is on the regions above 200 km, hence it is important to know the behavior of each constituent of the neutral atmosphere. Figure 1.3 illustrates the altitude profiles of various gas species above 100 km. Of particular importance in

this study are the altitude profiles of molecular nitrogen (N_2), molecular oxygen (O_2), and atomic oxygen (O). Above 200 km, the dominant species is atomic oxygen, which is the major source of ionized gas in this region. Note that, in this thesis, a symbol [x](h) denotes the number density of a species x at the altitude h km. For example, $[O_2](300)$ means the number density of molecular oxygen at 300 km.

As a first approximation for these number-density profiles, it is often assumed that each gas species is in hydrostatic equilibrium. Under this assumption, the variation of pressure, $p(h)$, and number density, $n(h)$, at height h are expressed as

$$\frac{p(h)}{p_0} = \frac{n(h)T(h)}{n_0 T_0} = \exp\left(-\int_{h_0}^{h} \frac{dz}{H(h)}\right) \tag{1.1}$$

where p_0, n_0, and T_0 are respectively the pressure, the number density, and the temperature at a convenient reference height, h_0. The expression $H(h)$ is called the *scale height* and is given by

$$H(h) = \frac{kT(h)}{mg(h)} \tag{1.2}$$

where k is the Boltzmann constant, m is the mass of the gas particle, and $g(h)$ is the gravitational acceleration at h. Over the altitude range of our interest (below ∼800 km), the height dependence of $g(h)$ can be neglected. The temperature in the upper thermosphere (above ∼200-300 km) can be supposed to be a constant, as shown in Figure 1.2. These approximations simplify the integral in Equation (1.1), and the number density is expressed as

$$n(h) = n_0 \exp\left(-\frac{h - h_0}{H}\right), \quad H = \frac{kT}{mg} \tag{1.3}$$

where g and T are taken at the altitude of interest. As the name *scale height* implies, H determines the range of heights over which the number density and the pressure of a gas decrease by a factor of e, i.e., $n(h + H) = n(h)/e \approx 0.37n(h)$. Since H depends

on m, the scale height of each constituent gas of the upper atmosphere differs from species to species, as illustrated in Figure 1.2.

1.2.2 Ionosphere

The upper atmosphere is slightly ionized mainly by the solar extreme ultraviolet (EUV) radiation. The region of this ionization is called the *ionosphere*. The ionosphere is a region of *weakly ionized plasma*, which is a mixture of neutral gas, positive ions, and electrons. About 0.1% of the neutral particles are ionized in the region of maximum ionization. Figure 1.4 shows the typical altitude profiles of electron number density (or *electron density profiles* in short) at lower mid latitude. An electron density profile is also called an *ionization profile*, or a *plasma density profile*, because complete charge neutrality is almost always kept in a plasma. However, note that the density profile of a specific ion species is not the same as the electron density profile because the ionospheric plasma contains several ion species.

The ionization profile of the ionosphere is determined by the altitude profiles of the rate of *production of ionization*, $Q(h)$, and the rate of *loss of ionization*, $L(h)$. Neglecting the transportation of plasma, the electron density $n(h)$ at an altitude of h is determind by the *density balance equation*

$$\frac{d}{dt}n(h) = Q(h) - L(h). \tag{1.4}$$

The production of ionization, $Q(h)$, is determined by the neutral gas density and the penetrated solar EUV energy at h; the participating neutral species vary with altitude. The loss of ionization is due to collisions between charged particles and neutral gas particles, but the controlling process varies with altitude. The loss rate, $L(h)$, is determined by the electron density and the neutral gas densitity at h. A thorough treatment of the formation of the ionosphere is found in [*Rishbeth and Garriot*, 1969]; more recent advances are elucidated in [*Schunk and Nagy*, 2009].

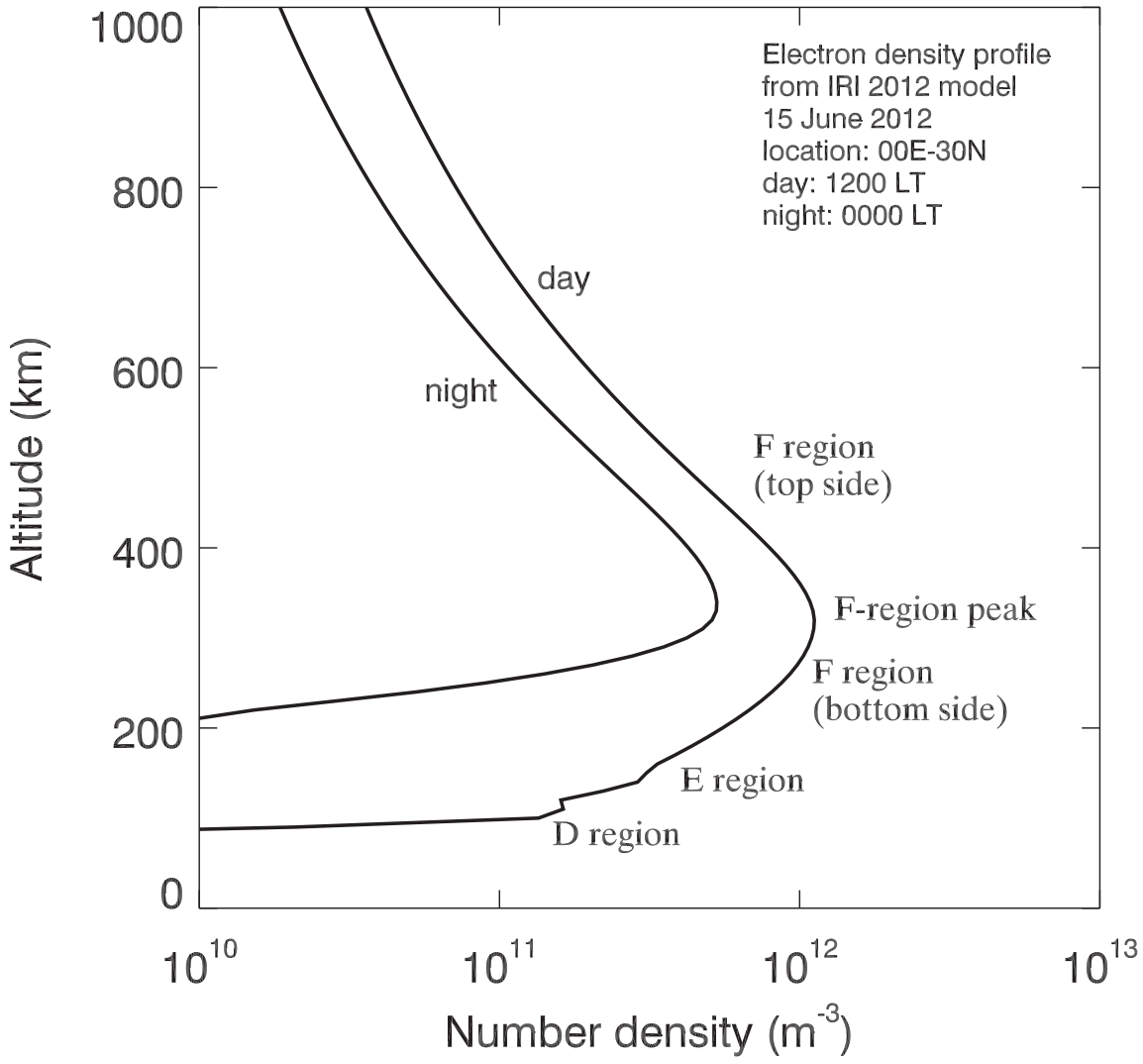

Figure 1.4: Typical electron density profile of the ionosphere.

As illustrated in Figure 1.4, a typical daytime electron density profile has its peak at around 250 km, though the peak altitude may vary from time to time. The region around this peak, roughly corresponds to the altitude range between ∼170 km and 1000 km, is called the *F region* or the *F layer*. Below F region are the *E region* (90-170 km), and the *D region* (below 90 km). During night-time, the D and E regions cease to exist because the neutral gases, particularly molecular nitrogen and oxygen, are dense in these regions. However, as shown in Figure 1.3, the number density of molecular nitrogen in the F region (∼300 km) is about 10^{-4} times smaller than that of in the E region (∼100 km). As a resut, a considerable amount of F-region plasma continues to exist at night.

Being a plasma, the ionosphere displays several electromagnetic phenomena such as elctrical conduction and electromagnetic-wave refraction and reflection. As the ionospheric plasma is immersed in the Earth's magnetic field, the ionosphere acts as the *magnetized plasma*. Some notable features are plasma transport by drift motion, anisotropic electrical conductivities, and various plasma waves in an anisotropic dispersive media. Since the direction of th Earth's magnetic field varies with latitude, i.e. almost vertical in the polar region and almost horizontal in the equatorial region, the behavior of the ionospheric plasma varies with latitude significantly.

The Earth's ionosphere is often divided into three regions according to their geomagnetic latitude, namely low-latitude, mid-latitude, and high-latitude regions. Factors that characterize these regions are magnetic dip angle, solar zenith angle, and the degree of magnetosphere-ionosphere coupling (MI coupling). The mid-latitude region, a zone roughly between 30° and 60° geomagnetic latitudes, has been most studied and is relatively well understood. The ionization in this region is produced mainly by solar EUV radiation and reduced by chemical reaction with neutral and ionized particles.

The processes in the mid-latitude ionosphere also work in the high- and low-latitude regions. However, in those regions, additional processes which are specific to those regions are operating and characterize the each region. In the low-latitude region which

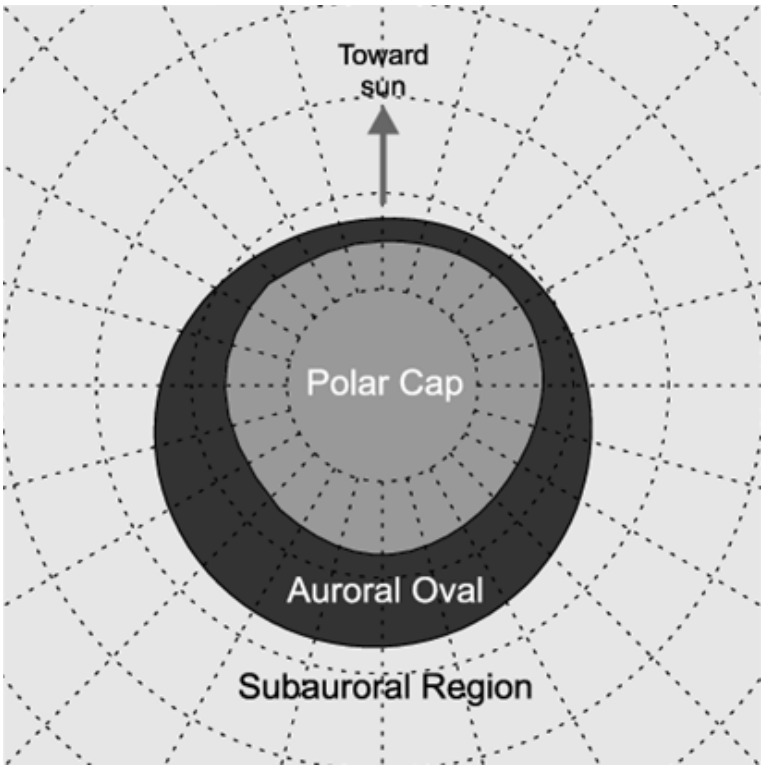

Figure 1.5: A schematic representation of the structure of the high-latitude ionosphere.

spans $\sim 30^\circ$ either side of the magnetic equator, the magnetic field lines are almost horizontal, solar radiation enters from the zenith, and there is virtually no direct MI coupling. Significant features in this region are twin-peaked distribution of high density plasma across the equator (the *equatorial anomaly*), vertical lifting of plasma across the field-lines (*electrodynamic lifting*), extremely large electrical conductivity, and a strong electric current (the *equatorial electrojet*) in the E region. In the high-latitude region, which is the region roughly above 60° geomagnetic latitude, the magnetic field lines are almost vertical, the solar zenith angle is large, and MI coupling is strong. These factors make the ionosphere significantly different at high latitude. Some of the high-latitude ionospheric features are described in the following sections.

1.2.3 High-latitude ionosphere

The high-latitude ionosphere can be further devided into the *polar cap*, the *auroral oval*, and the *subauroral region* as shown in Figure 1.5. The auroral oval is an annular

zone where visible auroral display occurs in response to energetic particle precipitation from the magnetosphere. The polar cap is a circular area inside the auroral oval. The subauroral region is an area outside the auroral oval. Note that there are two polar caps on the earth, one in the northern hemisphere and the other in the southern hemisphere; the same is true for the auroral ovals and the subpolar regions. The above division is based on the way by which the ionosphere couples to the magnetosphere via magnetic field lines which pass through the ionosphere (see Figure 1.1). The sizes of these regions and the positions of their boundaries are not fixed but vary with the IMF conditions.

Auroral oval. The auroral oval is the most dynamic region in the high-latitude ionosphere. The magnetic field lines whose footprints are on the nightside auroral oval are connected to the tail plasma sheet. In other words, the nightside auroral oval maps to the tail plasma sheet. The energetic particles in the tail plasma sheet move along these field lines and penetrate into the ionosphere. These energetic particles, mainly electrons, not only stimulate auroral emission but also enhance the ionization in the ionosphere in addition to the ionization by solar EUV radiation. Particle precipitation also increases the temperature of the upper atmosphere. The dayside auroral oval maps to the cusp and magnetospheric boundary layer. In particular, the ionospheric region which maps to the cusp is also called the *(ionospheric) cusp* region. The ionospheric cusp is unique because it is the only place in the ionosphere where direct access of solar-wind particles is possible. As in the nightside auroral oval, particle precipitation in the cusp region also stimulates auroral emission and enhances the ionization in the cusp ionosphere, but the effect is localized and less easy to detect compared with the nightside auroral emission.

Polar cap. The polar cap ionosphere is connected to the magnetotail via open magnetic field lines. The size of the polar cap is roughly proportional to the number of open field lines. This means that polar cap expands when the IMF B_Z is negative (southward) because the number of open field lines increases when $B_Z < 0$ through

dayside reconnections. Consequently, the auroral oval moves equatorward when the IMF B_Z is negative. This is true both in dayside and nightside auroral oval. For example, *Newell et al.* [1989] showed that the ionospheric cusp is located at $\sim 77^\circ$ geomagnetic latitude (MLAT) when $B_Z \sim 0$, but moves equatorward when $B_Z < 0$. In the polar cap ionosphere, the plasma density depends not only on the production and loss of ionization but also on horizontal transportation of plasma due to the *ionospheric convection*, which will be explained in 1.4.1.

Subauroral region. Unlike the polar cap and the auroral oval regions, the magnetic field lines in the subauroral region are closed. This region maps to inner magnetosphere and connected to the trapped particles in the inner magnetosphere. The subauroral ionosphere is less dynamic compared with the auroral oval because the subauroral region is not directly affected by the solar wind or outer-magnetospheric particles. However, during a major magnetic storm (section 1.3), an electric field with a wide spatial extent and a large potential difference appears in the subauroral region and affects the dynamics of the higher latitude ionosphere [*Foster and Burke*, 2002].

1.3 Magnetic storms

Changes in solar activity cause various geophysical effects through the changes in the solar radiation, the solar wind, and the IMF. Changes in the Sun are classified as either regular variations or transient activities, of which we are interested in the latter in this thesis. On the surface of the Earth, the most notable feature caused by solar transient activities is called the *magnetic storm*. Historically, magnetic storms were first perceived as sudden changes in geomagnetic field, thus termed as the magnetic storms. By 1925, studies had revealed that the fluctuations in the geomagnetic field are correlated with the changes in solar activity, the magnetic field fluctuations are caused by changes in electric currents flowing through the Earth's atmosphere (now known as

the ionosphere), and thus the changes in solar activity directly affect the electric current system in the Earth's upper atmosphere. Later studies have brought more detailed information, now collectively known as physics of the *solar-terrestrial environment* or *geospace*. It is known that both the thermosphere and the ionosphere are disturbed during a magnetic storm. These disturbances are called the *thermospheric storm* and the *ionospheric storm*, but the term *magnetic storm* is frequently used to represent these disturbances collectively. In this section we review some key features of magnetic storms.

1.3.1 Magnetic indices in various regions

Magnetic disturbances are characterized by *magnetic indices* which represent the deviations of ground-level magnetic recordings from their regular variations. Frequently used indices are the Dst, AE, and Kp indices which respectively represent low-, high-, and mid-latitude magnetic disturbances. The processes of deriving these indices are detailed in [*Campbell*, 2003]. Figure 1.6 (panels d–e) shows the variations of these indices during a 30-day period in July 2012. During this period, a major magnetic storm occurred on 15 July 2012 (day 197) after a minor magnetic storm on 9 July (day 191). Figure 1.6 also shows the variations of solar-terrestrial environment (panels a–c) including sunspot number (panel a, SSN), solar-wind velocity (panel b, V_{SW}), and the IMF B_Z (panel c). The sunspot number roughly indicates the level of solar activity, a positive change in V_{SW} suggests the arrival of "stormy" solar wind, and the (negative) amplitude of B_Z roughly corresponds to the amount of dayside reconnection.

Dst index. The Dst (means *stormtime disturbance*) index (Figure 1.6d) is derived from the magnetic field data obtained at four observatories in lower magnetic latitude regions. The Dst index represents the variation of the *equatorial ring current*. During a magnetic storm, a strong westward current flows above the equator, which decreases the horizontal component of the magnetic field on the surface of the Earth, and the

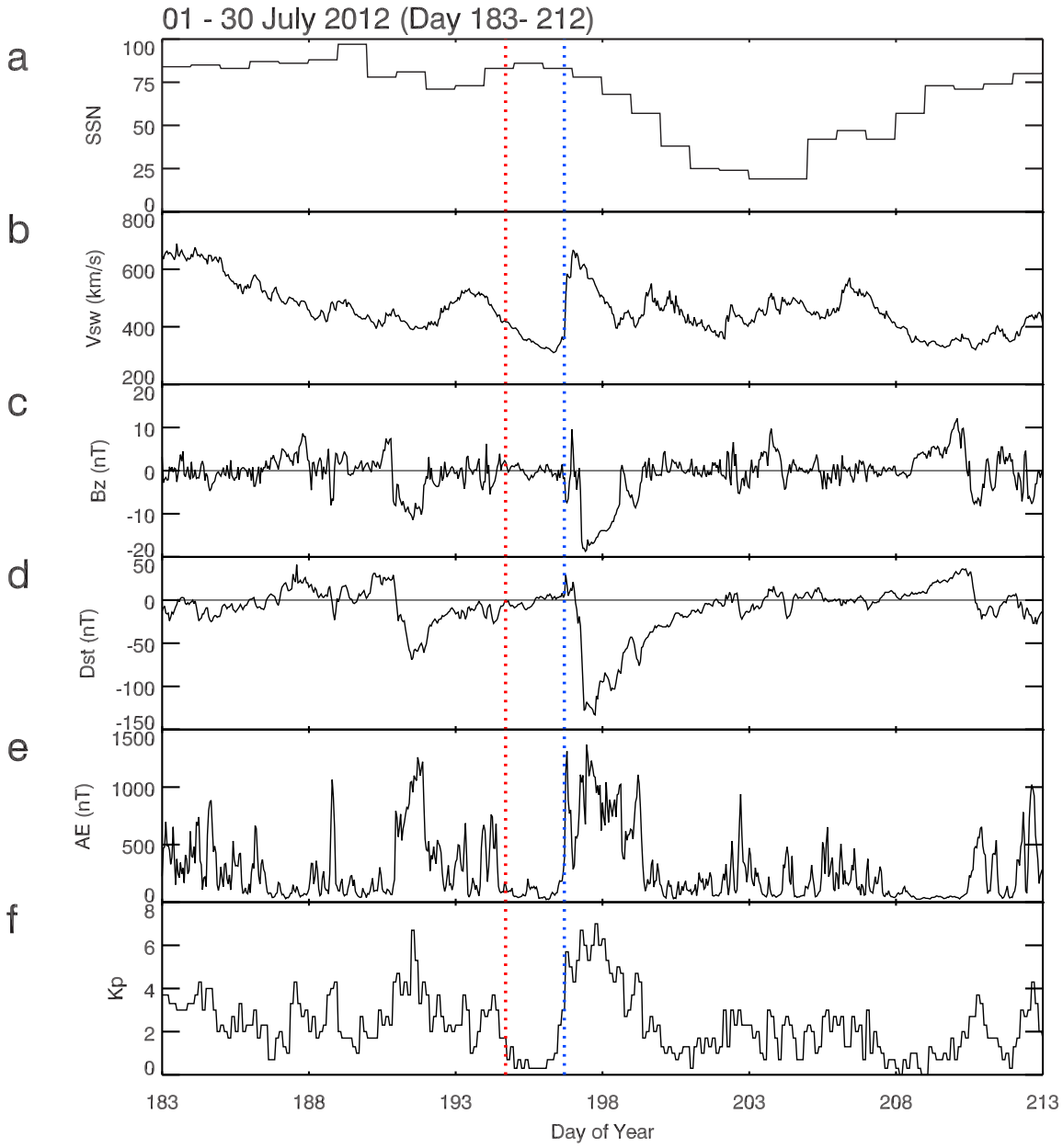

Figure 1.6: Thirty-day solar wind and magnetic disturbance indices. Panels a–f are explained in Section 1.3.1. The vertical dotted lines (in red and blue) are explained in Section 1.3.2.

Dst index decreases accordingly.

AE index. The AE (means *auroral electrojet*) index indicates the geomagnetic activity which is related to auroral activity around the auroral oval of the Northern hemisphere. The AE index is derived from the magnetic field data obtained at 10 to 12 observatories distributed in high latitude regions in Northern hemisphere.

Kp index. The Kp (from the German *Kennzahl, planetar*) index is derived from data obtained in the mid to subauroral latitudes in the Northern hemisphere. The derivation process of Kp index is complicated and it lacks the association with specific current systems. However, the Kp index gives a sufficiently good measure of geomagnetic activity and is widely used to indicate the general level of magnetic disturbance, especially in the mid-latitudes.

1.3.2 Temporal evolution of a magnetic storm

A magnetic storm can be predicted by monitoring solar activity, and can be traced by examining the magnetic indices. A wide range of electromagnetic spectrum, which travels with the speed of light, brings the information about solar activity. For example, a solar flare event accompanied by a coronal mass ejection (CME) event can be observed optically (EUV and X-ray) from spacecraft. This information arrives in the Earth within ten minutes after the event. On the other hand, the solar wind is much slower than the speed of light, at most ~ 750 km s^{-1} during a CME event. As a result, it takes about 2-3 days for the solar-wind particles to arrive in the Earth's magnetosphere.

In the example shown in Figure 1.6, a significant CME event occurred at about 1700 UT on 12 July 2012 (day 194) (indicated by dotted red line). Two days later, the near-Earth solar-wind speed suddenly increased from ~ 300 km s^{-1} to ~ 600 km s^{-1} (panel b), which indicates the arrival of the CME-origin fast solar wind (indicated by dotted blue line). Almost the same time as the arrival of the fast solar-wind particles,

B_Z goes to negative ~ -7 nT (panel c) and an immeadiate response of the AE index is observed (panel e). The Kp index also seems to have responded quickly, but the coarse time resolution of Kp (3 h) does not allow us to determine the exact response. Twelve hours after the arrival of fast solar wind, B_Z suddenly became extremely negative, close to -20 nT, and continued to be negative for more than a day. Following this, the Dst index decreased down to about -140 nT, kept almost the same value for about 10 h, and then gradually increased. It took more than 5 days for Dst to recover from this extreme condition. This means that the ring current did not cease to exist after the solar-wind condition had returned to the ordinary state (compare panels b, c, and d). Unlike the Dst index, AE index returned to low (the *quiet* state) when the solar wind and the IMF returned to the normal state.

1.3.3 Polar upper-atmospheric effects of magnetic storms

During a magnetic storm, a large energy dissipation occurs in the high-latitude ionosphere, especially in the auroral oval. We will examine the energy dissipation process later in this chapter, but here we just mention that the total power input is in the order of TW (10^{12} W). As a result of this huge energy input, neutral gas in the thermosphere is heated and, in response to this heating, the constituent gases redistribute vertically. In the lower thermosphere, gases redistribute according to Equation (1.3) to form a new hydrostatic equilibrium. From Equation (1.3), the scale height of a gas increases in proportion to the temperature, which results in an increase in number density at a specific height.

Figure 1.7 shows an example of thermospheric response to a magnetic storm during the same period shown in Figure 1.6. The figure shows the 30-day variation of the AE index and the high-latitude neutral gas parameters derived from the MSIS-E90 model. The neutral gas parameter values are daily representative values; the input parameters are: geographic latitude = 75° N, geographic longitude = 180° E, universal time = 0000 UT, and altitude = 300 km. As shown in panels a and b, the AE index and

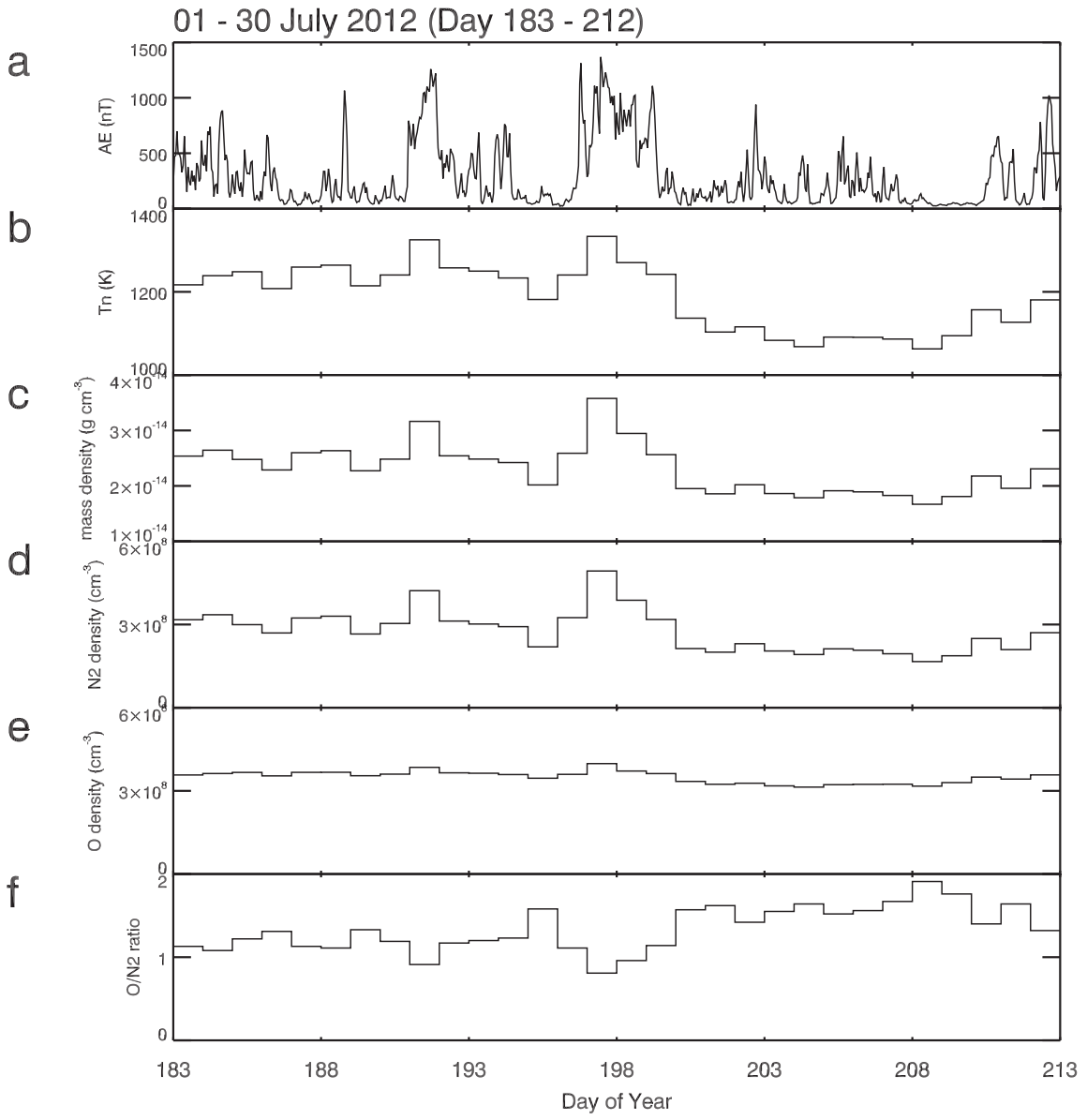

Figure 1.7: Thirty-day variations in thermospheric parameters derived from the MSIS-E90 model. Input parameters are: Coordinate type = Geographic, latitude= 75., longitude= 180., and height= 300.

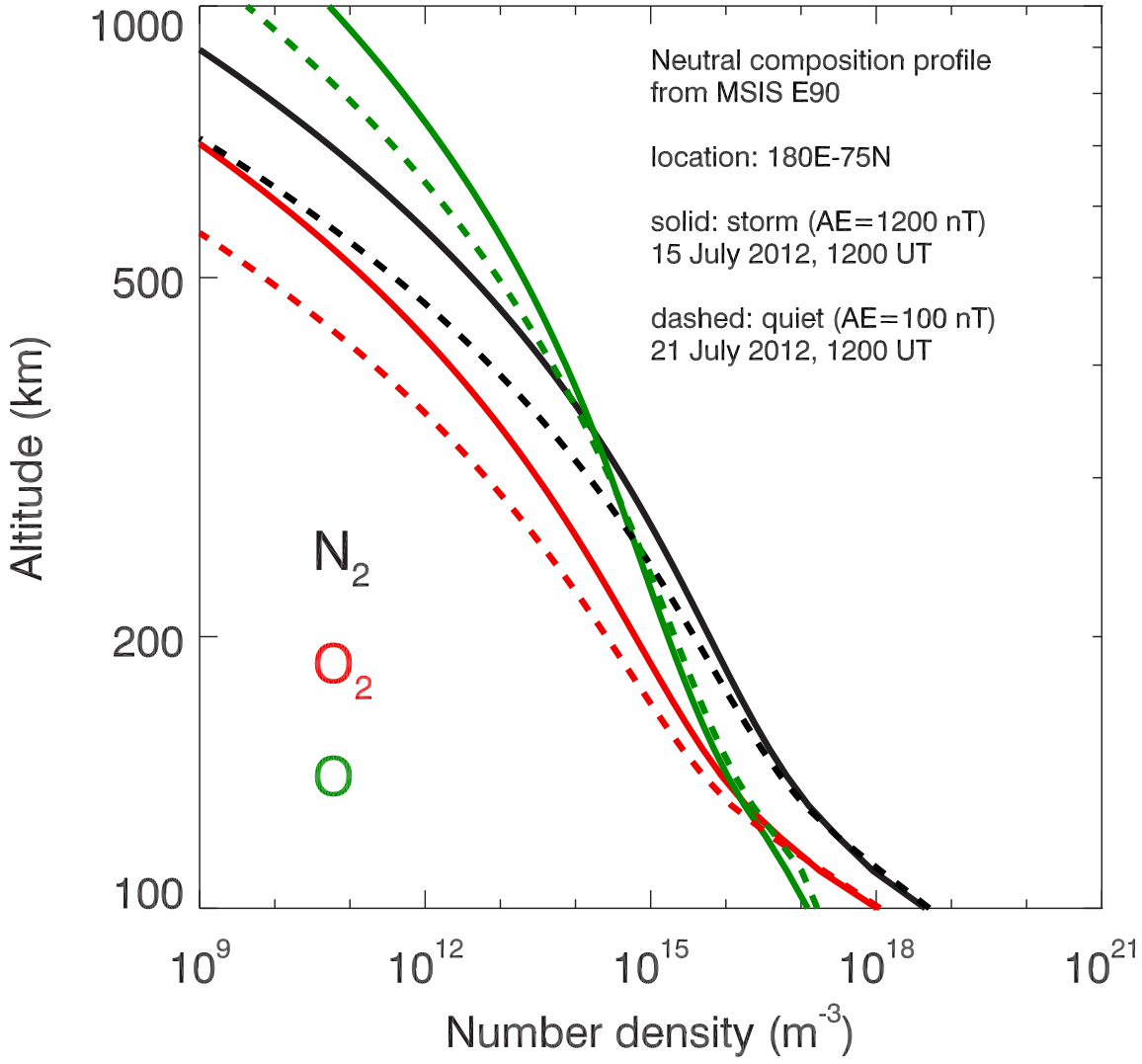

Figure 1.8: Changes in neutral gas densities during a magnetic storm.

the neutral gas temperature, T_n, are well correlated. This indicates that the increase in the neutral gas temperature is due to Joule heating by the auroral electrojet current. The neutral mass density (panel c) and the number density of molecular nitrogen, $[N_2]$ (panel d), responded to the temperature change with clear positive correration. However, the response of the atomic oxygen (panel e) is less significant. Figure 1.8 shows how neutral-gas densities change during a magnetic storm. Both $[O_2]$ and $[N_2]$ respond to the change in the AE index clearly. The response of [O] is less significant at F regin altitudes ($\sim$ 300 km). Consequently, the ratio $[O]/[N_2]$ decreases during a magnetic storm, as shown in Figure 1.7f. Observations of storm-time change in $[O]/[N_2]$

ratio, measured by spacecraft, are reported, for example, in [*Prölss*, 1982]. This effect leads to the depression of ionospheric plasma density, as described in 1.3.4.

1.3.4 Ionospheric storms in the high-latitude regions

Changes in the thermosphere directly affect the ionosphere. Atomic oxygen ion, O^+, is the dominant ion component of F-region ionospheric plasma. As explained in 1.2.2, the ionization production rate is proportional to the density of source neutral gas, in this case [O]. On the other hand, the ionization loss rate in the F region is controlled by $[N_2]$ and $[O_2]$. Assuming $[O_2]_{storm}/[O_2]_{quiet}$ is approximately equal to $[N_2]_{storm}/[N_2]_{quiet}$, the following relation about electron density, [e], is obtained [*Prölss*, 1995]:

$$\frac{[e]_{storm}}{[e]_{quiet}} \simeq \frac{[O]_{storm}/[O]_{quiet}}{[N_2]_{storm}/[N_2]_{quiet}} = \frac{[O]_{storm}/[N_2]_{storm}}{[O]_{quiet}/[N_2]_{quiet}} = \frac{([O]/[N_2])_{storm}}{([O]/[N_2])_{quiet}}. \tag{1.5}$$

In other words, when $[O]/[N_2]$ decreases during a magnetic storm, the F-region plasma density decreases. This effect is called the *negative (ionospheric) storm* [*Seaton*, 1955].

Figure 1.9 illustrates the development of a negative ionospheric storm during a major magnetic storm in July 2012. Each polar plot at the bottom of the figure represents the two-dimensional distribution of total electro content (TEC) in the northern hemisphere at a specific time. These TEC maps are obtaind by gathering the TEC data measured by a network of global positioning system (GPS) receivers [*Foster*, 2005]. As indicated by the AE index (panel a), day 195 (A) was quiet, and the ratio $[O]/[N_2]$ in F region was relatively high. The corresponding TEC map (A) shows that the TEC was between 5 to 12 TEC unit (TECU). On day 197 (B), due to the high AE index value, $[O]/[N_2]$ decreased significantly and reached below 1.0. The TEC map (B) shows that TEC decreased to $\sim$ 2 TECU in the nightside polar cap. The morning-sector TEC also decreased. The high TEC observed below 60° is supposed to be the result of *positive ionospheric storm*, which is an enhancement of ionization during a magnetic storm [*Jones and Rishbeth*, 1971]. Two days later, on day 199 (C), $[O]/[N_2]$ recovered slightly

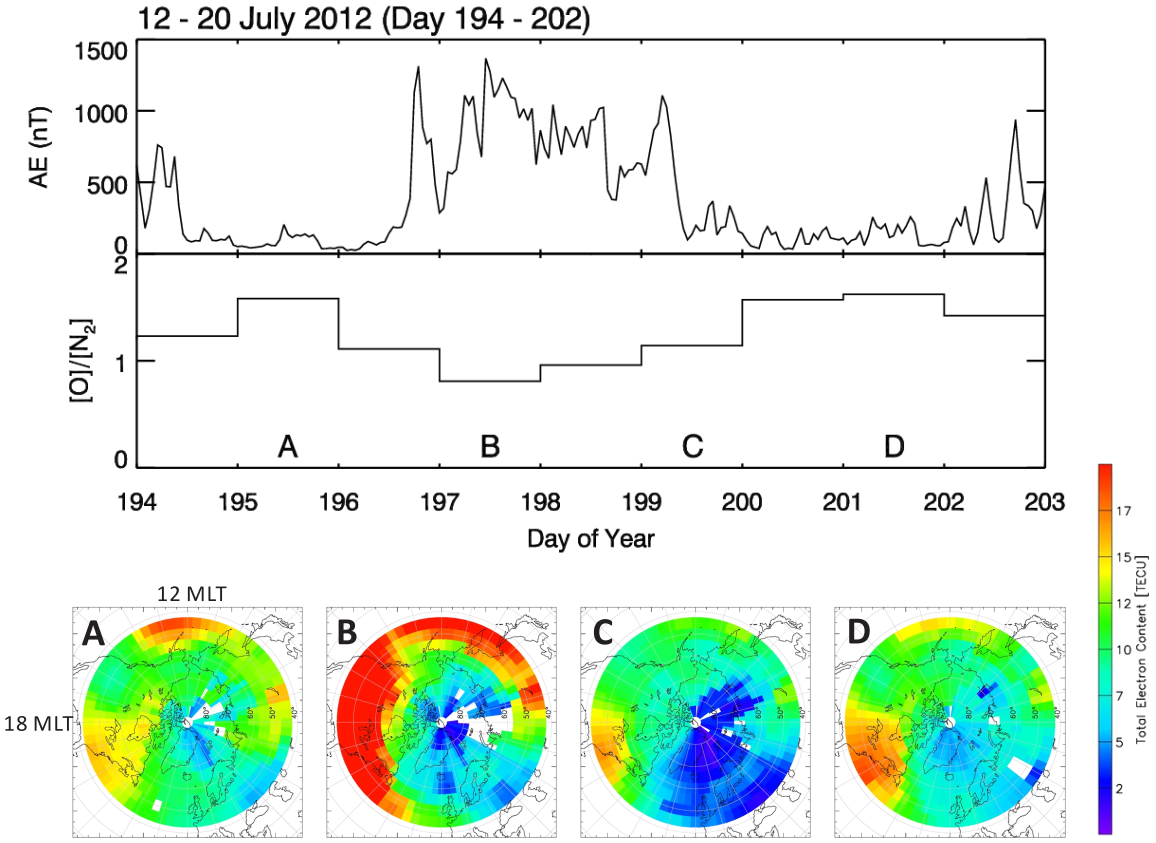

Figure 1.9: GPS TEC variation during a magnetic storm.

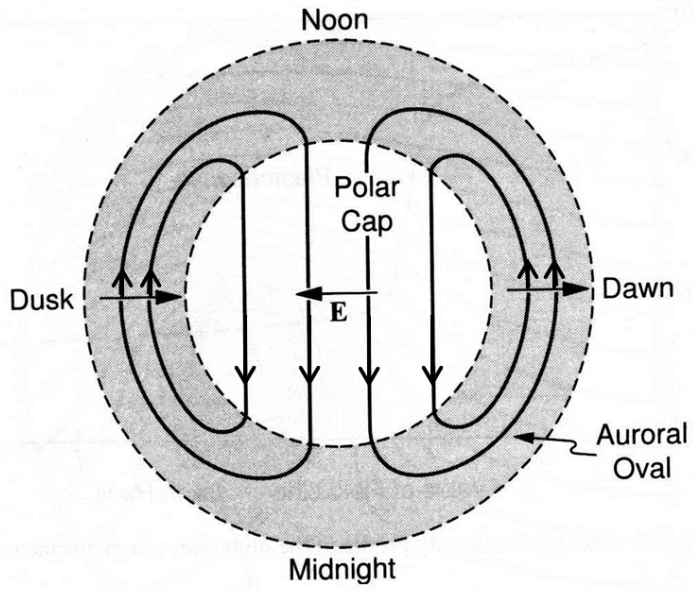

Figure 1.10: An idealized sketch of ionospheric convection in the northern hemisphere. Arrows on the closed loops represent the direction of convection flow. The horizontal arrows aligned with the dawn-dusk line represent the polar-cap elctric field mapped down from the magnetosphere. Adapted from [*Baumjohann and Treumann,* 1997]
.

but was still around unity. The TEC depression extended to mid latitude region in the night and morning side. On day 201 (D), the TEC depression ceased and the TEC map became similar to pre-storm state (A). As described above, a negative ionospheric storm usually lasts for a few days.

1.4 Plasma structuring in the polar ionosphere

1.4.1 Ionospheric convection in the polar cap

One of the important features of high-latitude ionosphere is the *ionospheric convection* or the *plasma convection*. Ionospheric convection is a process which consists a set of circulating horizontal plasma flows in the polar region. An idealized sketch of ionospheric convection is displayed in Figure 1.10, which corresponds to the IMF condition with $B_Y = 0$ and $B_Z < 0$. In this figure, two circulating cells in the polar cap are presented, and these two cells are merged in the center of the polar cap along the Sun-

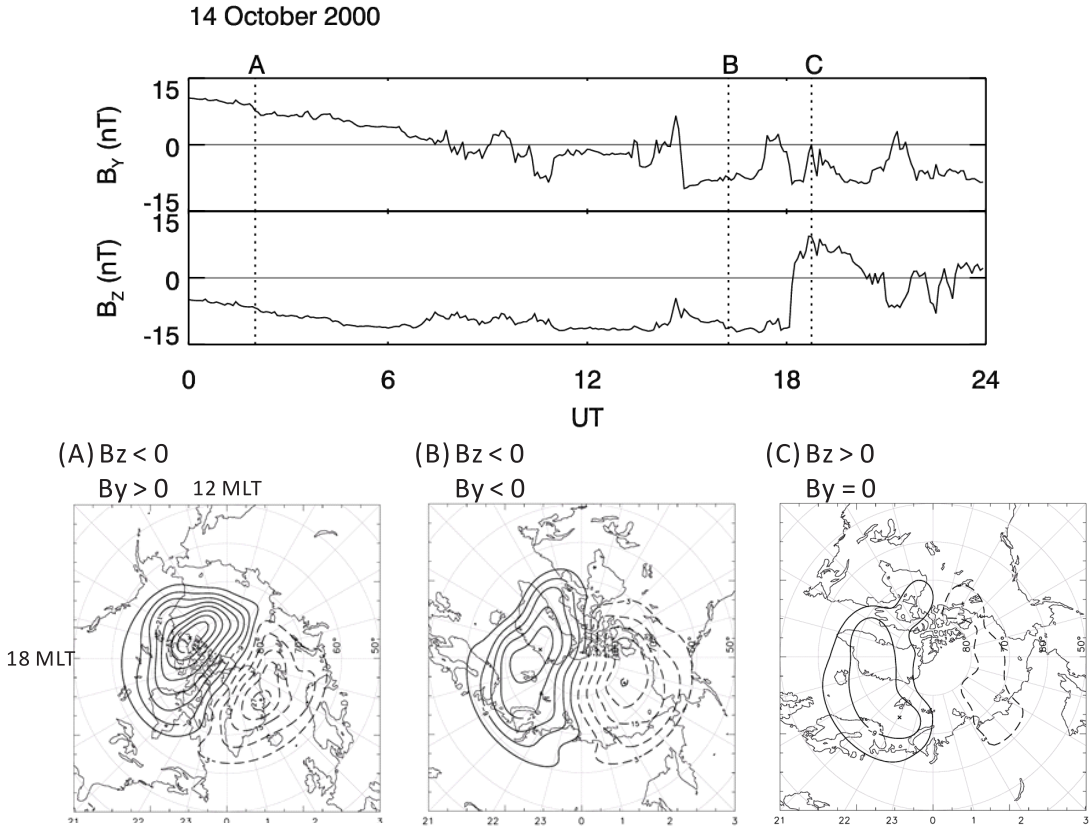

Figure 1.11: Ionospheric convection patterns in the northern hemisphere on 14 October 2000. The top two panels show the IMF B_Y and B_Z taken from OMNI database. The bottom two polar maps show the convection patterns corresponding to (A) $B_Z < 0$ and $B_Y > 0$, (B) $B_Z < 0$ and $B_Y < 0$, and (C) $B_Z > 0$. These convection patterns are calculated with the aid of a tool provided by Evan Thomas, at http://vt.superdarn.org/tiki-index.php?page=DaViT+TEC+Four+Plot.

Earth line to form an antisunward plasma flow. This two-cell pattern usually appears when IMF B_Z is negative, a condition which causes the *reconnection-driven magnetospheric convection*, and this magnetospheric convection in turn drives the ionospheric convection [*Dungey*, 1961]. The physical mechanism of the ionospheric convection is explained later in this section. Several models of ionospheric convection have been proposed to explain a variety of observational facts [*Heelis*, 1984; *Heppner and Maynard*, 1987; *Cowley et al.*, 1991]. Figure 1.11 shows the result of model calculation, based on Heppner-Maynard model, for typical convection patterns under different IMF conditions . As shown in the lower panels in this figure, both IMF B_Y and B_Z affect the two-dimensional shape of ionospheric convection. When B_Z is negative, two-cell

convection pattern appears; when B_Z is positive, cells almost disappear. While B_Z controls the existence of convection cells, B_Y controls the alignment of antisunward flow, as shown in (A) and (B) in the figure.

To explain the physical mechanism of ionospheric convection, we note that the coupling of the magnetosphere and the ionosphere is formed through magnetic lines of force; magnetic filed lines which pass through the polar cap ionosphere extend to the magnetosphere. Plasma physics tells us that such a field line behaves like a conducting wire with high conductivity [*Prölss*, 2004]. In other words, field lines act as equipotential lines along which the magnetospheric electric field maps to the ionosphere. As a result, an electric field appears in the polar cap ionosphere as shown in Figure 1.10. This electric field, with prevailing almost vertical magnetic field, drives a horizontal drift motion ($\vec{E} \times \vec{B}$ *drift* [see plasma physics text, e.g., *Chen*, 1974]) of ionospheric plasma which circulates in the polar region. The speed of this drift motion varies with the strength of the electric field and is roughly between a few 100 m/s and 1.5 km/s. Under disturbed conditions, the magnetospheric electric field, and hence the ionospheric electric field, is enhanced, and this results in the acceleration of ionospheric convection.

1.4.2 Polar-cap patches

Polar-cap patches (or *patches* in short) are islands of high-density plasma occuring in the F region of the ionosphere inside the polar cap. No precise definition of a polar-cap patch has been available to date, but widely accepted features which characterize a polar-cap patch are as follows [e.g., *Crowley*, 1996; *Roger*, 1998; *Carlson*, 2012]: plasma density is more than a factor of two higher than the background level; the horizontal scale varies from 100 km to more than 1000 km; patches appear when the IMF is southward ($B_Z < 0$); patches occur in the dayside ionosphere around cusp region and drift antisunward; patches emit 630 nm airglow and can be observed optically; patches can be also observed with radio tecniques such as ionosondes, incoherent scatter radars

(ISR), and HF radars.

1.4.3 Source of the plasma

Electron number density of a polar-cap patch is in the order of 10^{12} m^{-3}, which is comparable to that of well-sunlit (solar EUV-produced) dayside F-region plasam in the mid-latitude region. The electron temperature is usually similar to the ion temperature, which is also typical of sunlit plasma. From these facts, it is supposed that the plasma of polar-cap patches is sunlit origin. It is also possible that the particle precipitation in the dayside cusp creates relatively high-density plasma, and indeed some patches are believed to be precipitation origin. However, as the electron temperature of such a plasma is usually higher than the ion temperature, plasmas created by cusp particle precipitation can be distinguished from sunlit plasma. Although particle precipitations may enhance or modify the density of sunlit plasma to form patches, we limit our focus on patches of purely sunlit plasma in this study.

Under magnetically disturbed conditions, the electron density of a patch occasionally exceeds 10^{12} m^{-3}, up to $\sim 3 \times 10^{12}$ m^{-3} [*Sakai et al*, 2013], which is much higher than ordinary sunlit plasma. The source of this extraordinarily enhanced plasma is known as storm enhanced density (SED) [*Foster*, 1993]. A plume of high-density plasma is first created in the mid-latitude afternoon sector in the early stage of a magnetic storm. The plume is then transported toward noon by electric fields, known as subauroral polarization streams (SAPS). As the direction of the stream is opposite to the direction of the Earth's rotation, the plume is exposed to solar EUV radiation for more than six hours. As a result, the electron density increases before the plume arrives in the cusp region and then is entrained in the polar cap by the antisunward convection flow.

When a plume of high-density plasma enters the polar cap through the cusp region, it is called the *tongue of ionization (TOI)*. If a TOI is chopped due to some external forces upon or after the entry, it becomes a series of polar cap patches. A TOI is

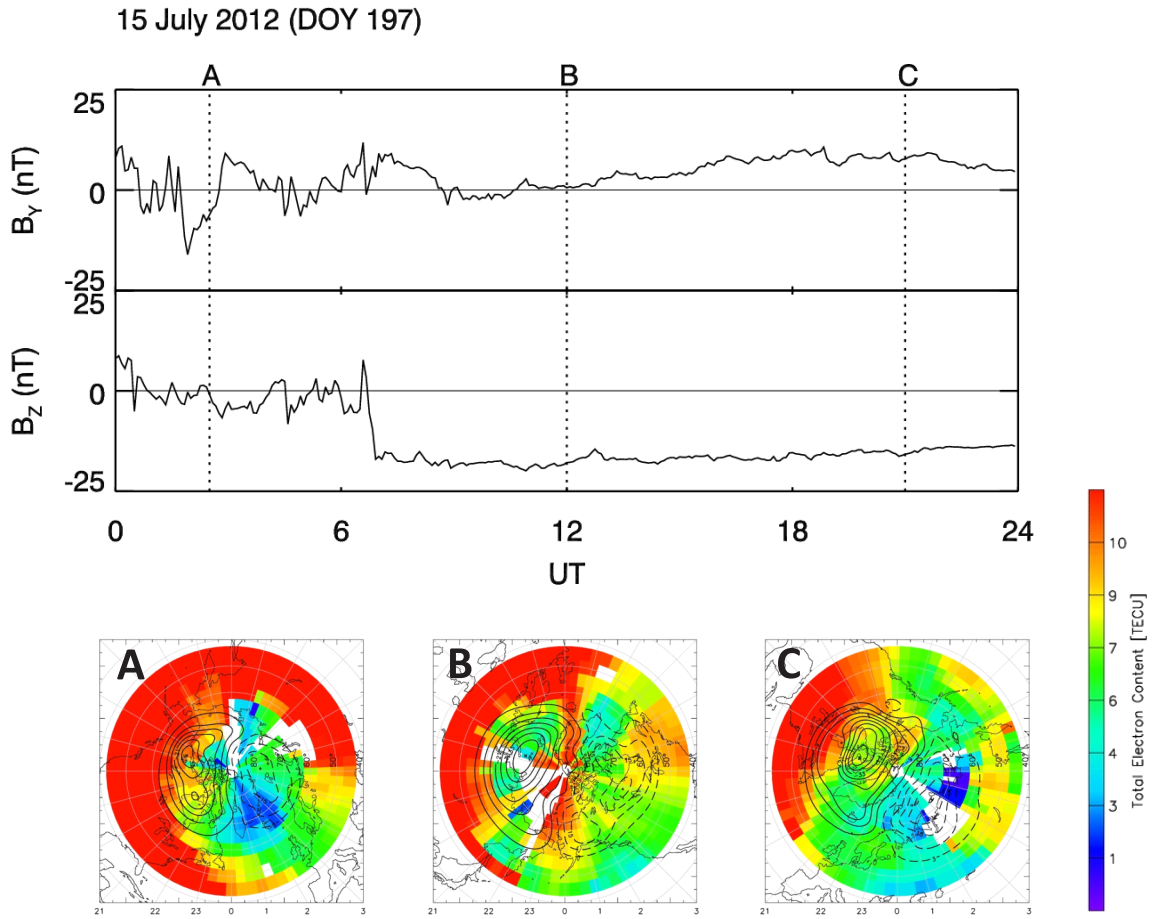

Figure 1.12: Tongue of ionization (TOI) under various IMF conditions.

expected to be seen when the IMF is southward ($B_Z < 0$). Polar maps in Figure 1.12 show TEC maps under various IMF conditions. When $B_Z \approx 0$ (A), under which no convection is expected, TEC is relartively low over the polar cap while the TEC in the subauroral region is high. After the IMF had turned to southward ($B_Z < 0$) (B), a clear signature of the antisunward flow appeared in the TEC map. A few hours later (C), B_Z was still negative, but B_Y became positive and the convection pattern has changed. The signature of the high density plasma flow became weak but still can be distinguised along the contour lines.

1.4.4 Mechanisms of patch formation

Several mechanisms have been proposed to explain how patches are created. *Carlson* [2012] summarized these mechanisms into six categories: (1) discrete changes in IMF B_Y, B_Z, and solar wind parameters (density, speed, and pressure); (2) time variation of average flow pattern models [e.g., *Anderson et al.*, 1988]; (3) plasma flow jet channels in which relative velocity-dependent recombination rates cut continuous TOI into segments [*Valladares et al.*, 1998]; (4) IMF reversals and plasma production by cusp particle precipitation [*Roger et al.*, 1994; *Millward et al.*. 1999]; (5) transient magnetopause reconnection [*Lockwood and Carlson*, 1992]; (6) transient magnetopause reconnection followed by Alfven wave coupling of the solar wind to the ionosphere [*Prikryl et al.*, 1999]. To date, no single mechanism has established dominance and it is supposed that every mechanism has opportunity to play under various conditions.

Recently, *Sakai et al.* [2013] showed that changes in IMF B_Y resulted in significant changes of radar-observed electron density in the polar cap. The event is described in detail in Chapter 2. It should be noted, however, that density changes observed at one site does not necessarily correspond to patches. In this example, it is probable that the changes in B_Y displaced the flow of high-density plasma, i.e. convecting TOI, only slightly and the TOI have not been chopped to form patches. To determine if the observed density changes represent patches, two dimensional observation techniques such as all-sky imaging or network of radio observations are necessary.

1.4.5 Transportation and decay of polar-cap patches

Once created in the dayside cusp region, polar-cap patches drift over the polar cap to nightside and exit from the auroral oval to subauroral region. As the drift speed is roughly $\sim$ 1 km/s, this trans-polar drift takes a few hours. During the travel, the ionization at the lower altitudes decays due to collisions with relatively dense neutral gas particles. At higher altitudes, above $\sim$ 250 km, since neutral densities are low, and

owing to the different ion chemistry from the lower altitudes, plasma will not decay within a few hours. *Hosokawa et al.* [2011] estimated the time constant of F-layer patch plasma to be $\sim$ 1 h at 250 km and $\sim$ 4 h at 295 km. This indicates that F-layer patches can be observed in the midnight sector, and this is indeed the case. It is also expected that patches continue to exist after exiting from the polar cap and drift back to the dayside floating on the sunward convection flow. The process is sometimes referred to as *patch recycling*, although the multiple recycling is unlikely to occur [*Pedersen et al.*, 1998].

1.5 Purpose and structure of the thesis

In the previous sections we have reviewed some important features of the polar-cap ionosphere under disturbed conditions. The polar cap is a unique region where the upper atmosphere directly interacts with the magnetosphere through the open magnetic filed lines. Studying the polar cap ionosphere not only brings new scientific insight in its own but also provides information about magnetosphere. In addition, it gives foundations for numerous technological applications such as transpolar communications, satellite navigation systems in the high latitude regions, and other *space weather* applications. Although decades of studies have revealed important features of the polar cap ionosphere, there still remain some unanswered questions, of which two are investigated in this thesis as follows.

In Chapter 2, we examine an event of extremely sharp depletions of F-region plasma observed in the polar cap. Plasma density fluctuations in the polar cap F region are often associated with polar cap patches, and several models have been proposed for the formation of patches, as described in 1.4. However, in the event which we investigate in Chapter 2, the high-to-low density ratio is extremely large compared with previously reported patches. To explain such an extreme density changes, a thorough investigation of the event is necessary, and the result is detailed in Chapter 2.

In Chapter 3, we turn our attention to polar-cap patch airglow. As explained in 1.4.2, polar-cap patches can be observed either with optical instruments or IS radars. Optical instruments measure the brightness of the airglow of a patch whereas IS radars measure the electron density of a patch. Although correlation between airglow brightness and electron density of patches has been studied by several authors for decades, mainly in the low- and mid-latitudes, those in the high-latitude region have not been well understood. In particular, the altitude profile of airglow brightness under a magnetically disturbed condition has not been studied, and there exist uncertainties in estimating (1) the peak altitude of a patch airglow, and (2) plasma density from airglow brightness. To eliminate these uncertainties, we use a set of data obtained by simaultaneous observation of airglow and electron density in the polar cap under magnetically disturbed conditions and analyzed the relationship between them. The results are thoroughly described in Chapter 3.

As stated above, this thesis includes two separate studies of polar cap ionosphere; one is about the dayside polar cap and the other is about the night-side polar cap. By combining the knowledge aquired in these studies we expect to take further steps to draw a full picture of the transportation of plasma structures across the polar cap. Figure 1.13 shows the scope of current and future studies, which will be briefly presented in Chapter 4.

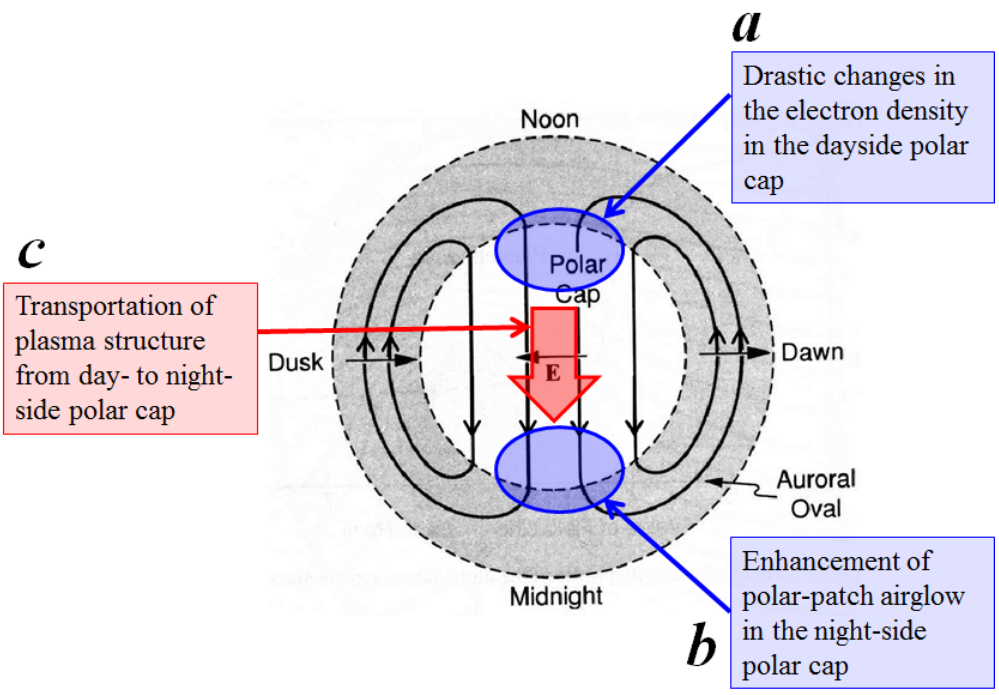

Figure 1.13: A conceptual sketch of current (a and b) and future (c) studies. Base figure (monochrome part) is the same as Figure 1.10; annotation (color part) added by the author of this thesis.

Chapter 2

Steep plasma depletion in dayside polar cap during a CME-driven magnetic storm

2.1 Introduction

A typical structure of the polar cap F region is a convecting region of enhanced plasma density that has horizontal dimensions of ∼100 to ∼1000 km [e.g., *Coley and Heelis*, 1995]. This region is referred to as a polar patch, and the plasma density within a polar patch is often enhanced by a factor of 2–10 compared to that in the surrounding region [*Weber et al.*, 1984]. Numerous studies have investigated the characteristics of polar patches in detail [see comprehensive reviews by *Crowley*, 1996; *Rodger*, 1998; *Basu and Valladares*, 1999], and nowadays, it is known that understanding their characteristics is of importance in applications to space weather forecasting [*Basu et al.*, 2002; *Carlson*, 2012].

Apart from plasma transport, understanding the characteristics of various structures such as a polar patch requires two competing processes: the enhancement and the depletion of the electron density. The electron density enhancement in the day-

side polar cap during an interval of southward interplanetary magnetic field (IMF) is largely due to plasma transportation from the cusp or the latitudes equatorward of the cusp and not in-situ plasma production, with the exception of solar plasma production principally in summer when the whole of the polar cap is in sunlight. Furthermore, at latitudes equatorward of the cusp, i.e., at mid-latitudes, the electron density may enhance during magnetic storms, also called as positive ionospheric storms, although the normal storm response at mid-latitudes is a reduction in electron density.

Another noticeable feature at mid-latitudes is a plume of enhanced plasma called the storm-enhanced density (SED) plume. This appears in the afternoon sector when mid-latitude (occasionally also lower-latitude) plasmas are transported to the afternoon sector by the equatormost part of the high-latitude plasma convection flow in the evening sector. During transportation, the plasma travels for a long time in the sunlit afternoon sector, which results in higher electron density. *Foster* [1993] characterized SED plasmas as being cold and having elevated F region peak altitudes and enhanced topside densities. When SED plasma is entrained into the polar cap through the cusp inflow region, i.e., the throat region, it forms a tongue of ionization (TOI) [e.g., *Sato*, 1959; *Foster*, 1984; *Foster et al.*, 2005; *Hosokawa et al.*, 2010].

Several models have been proposed for the plasma depletion observed in the polar cap. These models basically have two mechanisms: entry of low-density plasma from equatorward of the cusp and depletion of ionization in the cusp. The plasma levels entering the polar cap from the morning sector may be well below those of the afternoon cell plasma [*Rodger*, 1998]. When the proportion of the plasma entering the polar cap from the morning and evening sector changes, localized depletion regions may be seen in the polar cap. *Cowley et al.* [1991] showed that the direction of the y-component of the IMF, i.e., B_Y, affects the longitudinal position of the convection throat. When the convection throat shifts longitudinally, it may entrain low-density plasmas. IMF B_Y also controls the dawn-dusk position of the high-density plasma stream into the polar cap (i.e., TOI), and this may make the configuration of the low-density plasma

complicated [*Sojka et al.*, 1994; *Heelis*, 1984]. The depletion of ionization can be caused by fast plasma flow because of the increased $O^+ + N_2$ reaction rate associated with ion-neutral frictional heating [*Schunk et al.*, 1975]. In the cusp, fast plasma flow originates from flux transfer events (FTEs), and this is thought to be a possible cause of the low-density plasma in the polar cap [*Rodger*, 1998].

Milan et al. [2002] suggested alternating enhancement and depletion in the polar cap as an explanation for the large-scale poleward-propagating feature observed by the high-frequency (HF) radar. *Milan et al.* [2002] suggested that this feature is created in such a manner that high-density mid-latitude plasma enters the polar cap when the convection flow is poleward in the cusp and low-density plasma is entrained behind the high-density plasma when the convection flow becomes zonal. For a similar poleward propagating feature, *Taguchi et al.* [2009, 2010] suggested that it is important that the TOI is deformed by fast azimuthal flow having less dense plasma and that the interface between the deformed TOI and the fast azimuthal flow moves poleward.

While these studies provide the spatial distribution of the electron density in a relatively large area covering the cusp and dayside polar cap, the distribution itself is not based on actual electron density observations. An incoherent scatter (IS) radar is a powerful tool for understanding the electron density and other ionospheric parameters such as the electron and ion temperatures and the line-of-sight ion drift velocity. It also provides the height profiles of these parameters. Studies with IS radar data help a better understanding of the phenomenon in which electron density enhancement and depletion are adjacent. The EISCAT Svalbard Radar (ESR), located at Longyearbyen, Svalbard, is the best IS radar for this purpose and has been used by many authors to investigate polar patches for decades [e.g., *Lockwood and Carlson*, 1992; *Oksavik et al.*,, 2010].

In this paper, we present an ESR observation in which the electron density increased or decreased sharply by a factor of more than 10 several times over the course of 3 h. These events occurred on 14 October 2000, during a coronal mass ejection (CME)-

driven magnetic storm. We show that the observed electron density variations were related to plasma transportation rather than in-situ creation, and we demonstrate that the change in the sign of IMF B_Y triggered the electron density depletions in the TOI during the period of extreme enhancement of electron density.

2.2 Instrumentation

2.2.1 EISCAT Svalbard Radar

The ESR, located at Longyearbyen (78.15°E, 16.02°N), Svalbard, is equipped with two antennas: a fixed 42-m dish antenna (ESR 42 m) and a steerable 32-m dish antenna (ESR 32 m). The 42-m antenna dish is fixed so that its beam is aligned to the magnetic field lines above the ESR site. The 32-m antenna is steerable, both in azimuth (full 360°) and in elevation (>30°), so that it can provide a variable field of view (FOV). Some important parameters of the ESR are as follows: geomagnetic dip angle (ground) = 82.23°, corrected geomagnetic latitude = 75.43°, and magnetic local time (MLT) = UT + 2.75.

In this study, we used a set of ESR common program (CP) data obtained from 0400 UT to 1200 UT, 14 October 2000. Figure 2.1 illustrates the ESR beam configuration (a) and the coverage (b) of both the 42-m and 32-m antennas during this period. The 42-m antenna scans altitudes between 80 and 1200 km along the nearly vertical magnetic field line with a fixed elevation angle of 81.6°. These altitudes correspond to magnetic latitudes between 75.0°N and 75.3°N, indicating that the beam is almost aligned with the magnetic field line. In this observation, the 32-m antenna operated with geographically fixed azimuth and elevation angles. The azimuth angle of the 32-m antenna was 340°, with the beam being directed poleward. The elevation angle of the 32-m antenna was 31° from the ground. The observed altitudes ranged from 78 km to 744 km, which correspond to a ground range of 770 km. In terms of magnetic coordinates, the beam covered the latitudes between 76°N and 83°N. As shown in

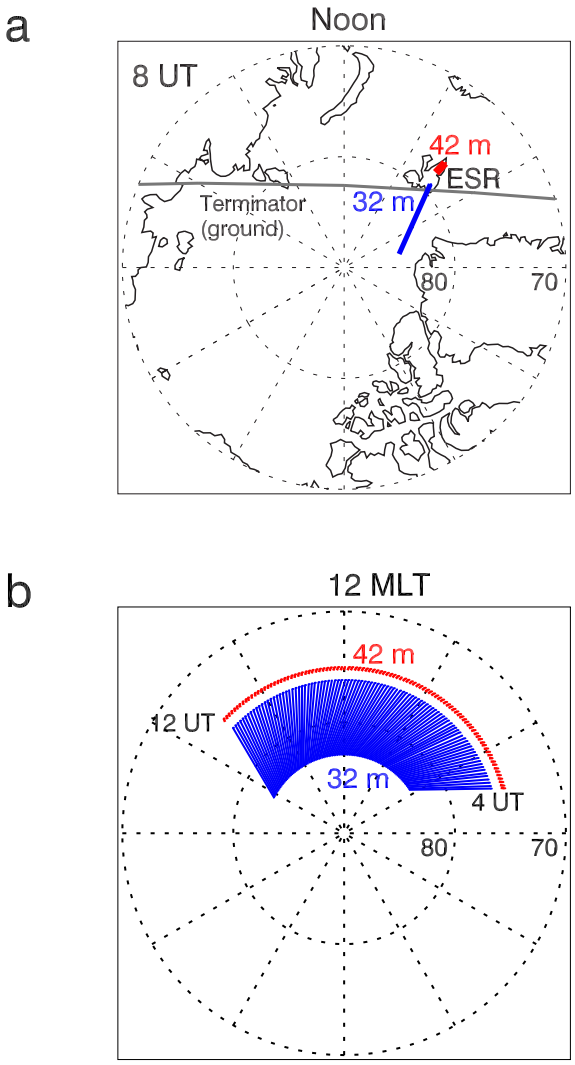

Figure 2.1: (a) Beam configuration (in geographic coordinates at 0800 UT) and (b) coverage (in magnetic latitude and magnetic local time) of the EISCAT Svalbard Radar. A thick grey line in (a) indicates the terminator at ground level. The 42-m antenna (blue) is fixed with an elevation angle of 81.6° and azimuth angle of 181.0°. The 32-m antenna is steerable. During the observation, the elevation and azimuth angles were adjusted to 31° from the ground and 340.0°, respectively. Note that the 42-m antenna beam was directed along the magnetic field lines almost vertically while the 32-m antenna beam was directed towards the North Magnetic Pole with 31° upward horizontally.

Figure 2.1b, observations were performed using the 42-m antenna from approximately 07:00 MLT to 15:00 MLT. As the bottom and the top of the 32-m beam were at different MLTs, being 1 h apart, the equatorward (bottom) edge of the FOV was from 07:00 MLT to 15:00 MLT, whereas the poleward (top) edge was from 08:00 MLT to 16:00 MLT. The geometry of the fan-like shape in Figure 2.1b shows this condition.

Data processed with 30 s integration were used for most of our analyses. When appropriate, data with 120 s integration were also used in the figures to reduce their size.

2.2.2 DMSP spacecraft

The Defense Meteorological Satellite Program (DMSP) spacecraft data were used to investigate the two-dimensional distribution of the plasma density during the ESR observations. Four DMSP spacecraft—F12, F13, F14, and F15—were operative on 14 October 2000. They were in polar orbits, and each spacecraft passed over the northern polar cap every 100 min. They flew at altitudes of between 840 km and 880 km that overlapped the upper part of the ESR 42-m observation. These DMSP spacecraft were equipped with the Special Sensors-Ions, Electrons, and Scintillation (SSIES) thermal plasma analysis package, and provided, among other things, the ion density data, which we used in this study. The DMSP spacecraft also provided the energy flux spectra of ions and electrons through the SSJ/4 particle detectors. We used the DMSP ion and electron energy flux data in order to determine the latitude of the cusp.

2.3 Observation

2.3.1 Overview of storm that commenced on 12 October 2000

A major CME storm commenced at around 2200 UT on 12 October 2000 and continued for approximately 30 h [*Kataoka and Miyoshi*, 2006]. Figures 2.2a and b show a plot of

three-day IMF data extracted from NASA/GSFC's OMNI data set through OMNIWeb. The plot indicates prolonged southward IMF ($B_Z < 0$) before the event described in this paper. Figures 2.2c and d show the solar wind plasma speed and the SYM-H index, respectively.

In this study, we focused on a 3-h period between 0700 UT and 1000 UT on 14 October 2000. Figures 2.2e–h show the three IMF components measured over this period by the GEOTAIL spacecraft, which was situated approximately on the Sun-Earth line in front of the Earth ($X_{gsm} = 26.8$ R_e, $Y_{gsm} = -1.8$ R_e, and $Z_{gsm} = 5.4$ R_e at 9 UT). For most of the observation period, the IMF B_Z remained significantly negative (approximately -10 nT), whereas the IMF B_Y changed its sign from positive to negative at around 0730 UT and fluctuated thereafter throughout the day. The solar wind velocity V_x was 350–400 km s^{-1} during this period (Figure 2.2c). The solar wind proton density was between 4 cm^{-3} and 10 cm^{-3} during the period (not shown).

To determine the location of the cusp, we investigated the DMSP ion dispersion signatures [*Newell and Meng*, 1988]. Figure 2.3a shows an example of the spectrogram taken by DMSP F12 at around 0700 UT, which shows that the cusp was at ∼66° MLAT at this time. This information is used for estimating the size of the polar cap and for determining whether the ESR was observing the polar cap or the auroral region. This information is also crucial for estimating the IMF propagation delay from GEOTAIL to ESR. A set of DMSP records including the abovementioned example shows that the cusp location during the interval of interest lay between 66° and 68° MLAT, as shown in Figure 2.3b.

Figure 2.4 shows the ion density, obtained from SSIES, along the DMSP flight path as observed by multiple spacecraft from 0600 UT to 1200 UT. A region of high ion density (reddish color) is present in magnetic latitudes between 60° N and 80° N spanned from 11 MLT and 12 MLT. This suggests that there was a TOI during this interval, which occurred during the period of southward IMF. After 1800 UT, when the IMF B_Z became positive, the TOI disappeared (not shown). Figure 2.4 also shows

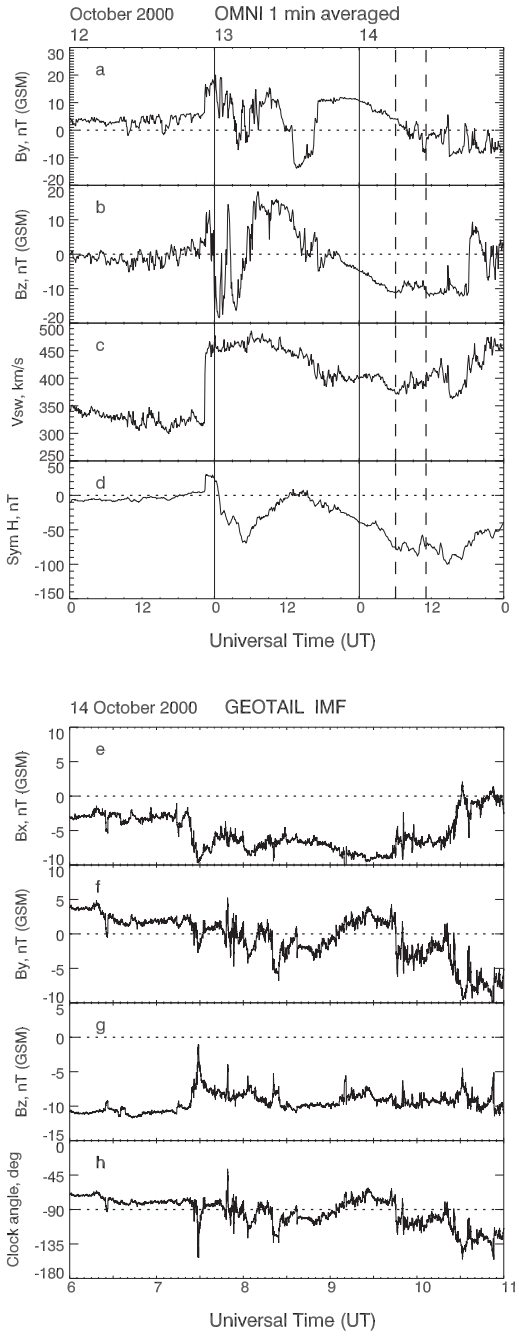

Figure 2.2: (a–d) From top to bottom, (a) the y-component of the interplanetary magnetic field (IMF B_Y), (b) the z-component of the IMF (B_Z), (c) solar wind plasma speed, and (d) the Sym-H (Dst) index during a storm interval from 12 October 2000 to 14 October 2000 taken from OMNI database. Two vertical dashed lines indicate the start and end time for the bottom panel. (e-f) The interplanetary magnetic field components B_X, B_Y, and B_Z and the clock angle measured by the GEOTAIL spacecraft during the period between 0600 UT and 1100 UT, 14 October 2000.

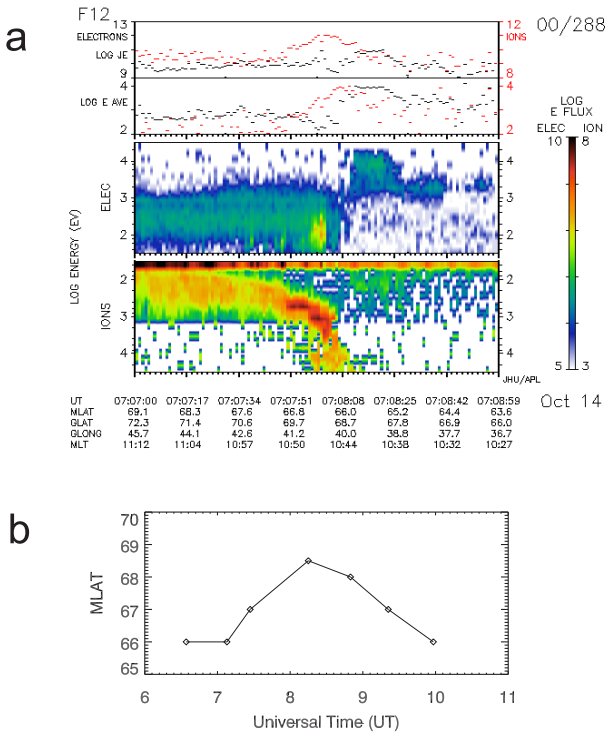

Figure 2.3: Estimation of the cusp location. (a) An example of the DMSP ion and electron energy flux data used to estimate the cusp location, and (b) estimated locations of the cusp between 0630 and 1000 UT on 14 October 2000. The longitudinal displacement (in MLT) of the cusp crossing of DMSP and the ESR lies approximately between -1 h and 1 h depending on the observation time and spacecraft.

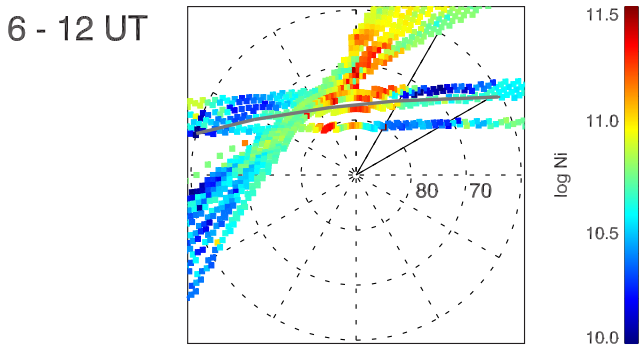

Figure 2.4: Ion density variation observed by DMSP spacecraft between 0600 UT and 1200 UT on 14 October 2000. The panel shows 6-h observations of ion densities by four spacecraft. Data points are binned and averaged over 6 h. Note that there is a distinct low-density region between 08:00 MLT and 10:00 MLT (indicated by two solid lines). The solid grey line indicates the ground level terminator for 8 UT.

that a region of low-density plasma is clearly observed adjacent to the region of high-density plasma. This arises from the data obtained between 0800 UT and 1000 UT. In general, a plasma density at the DMSP height is not correlated with a peak density at altitudes of 300–400 km. For the present event, however, the density enhancement and depletion occurred at a wide range of altitudes over 300 km, as shown below.

2.3.2 The density-cutoff event

Figures 2.5a–d summarize the observation by the 42-m antenna of ESR. From top to bottom, the panels show the electron density $\log N_e$, electron temperature T_e, ion temperature T_i, and line-of-sight (LOS) ion drift velocity V_i. As shown in Figure 2.5a, there was a period of strong enhancement of the electron density accompanied by intermittent depletions. This enhancement period started at around 0700 UT and lasted for more than 2.5 h. The peak density exceeded 10^{12} m^{-3} during this period. During this period, the electron density exhibited abrupt cutoffs five times, depleting the electron density to as low as $\sim 10^{11}$ m^{-3}. Each depletion period continued for about 10 min until the density recovered from the depletion. We refer to those depletions as "major depletions" according to the following criteria: $\log NmF2$ falls by at least 0.5, and the duration of depletion is at least 3 min. In addition to these major depletions,

there were some minor fluctuations between the major depletions.

Figure 2.5b shows the variation in the electron temperature. A clear negative correlation was observed between the electron density and the temperature. When the electron density increased, the electron temperature decreased by 1500 K from its background level of ∼3000 K, whereas the temperature recovered to the background level when the density depleted. As shown in Figure 2.5c, the ion temperature remained rather stable compared with the electron temperature, although there were three distinguishable slits that correspond to the changes in N_e and T_e between 0800 UT and 0900 UT.

Figures 2.5e–h summarize the observation by the 32-m antenna with the same format as in Figures 2.5a–d except for the color scale for the LOS ion velocity V_i. The electron density (Figure 2.5e) began increasing at around 0600 UT, which was almost 1 h before the electron density began increasing in the 42-m observation (Figure 2.5a). There were distinctive slits in the electron density between 0800 and 1000 UT, seemingly corresponding to the N_e depletion observed by the 42-m antenna. As in the 42-m observation, there was a strong negative correlation between N_e and T_e (Figures 2.5e and 2.5f). Figures 2.5e and 2.5f suggest that the variations in N_e and T_e propagated poleward. The ion temperature (Figure 2.5g) remained fairly stable except for a few slits found at later times. The LOS ion velocity observed by the 32-m antenna (Figure 2.5h) at altitudes above 200 km was positive for most of the time, and it varied between ∼300 m s^{-1} and 1 km s^{-1}. This suggests that the plasma being observed was undergoing antisunward convection.

Electron density variation

Figure 2.6a shows the electron density (N_e) variation observed by the ESR 42-m antenna. The electron densities at various altitudes ranging from 214 km to 522 km are presented as a function of time. Each dot, representing a data point, is color-coded according to the altitude, as indicated on the right. This representation gives a more

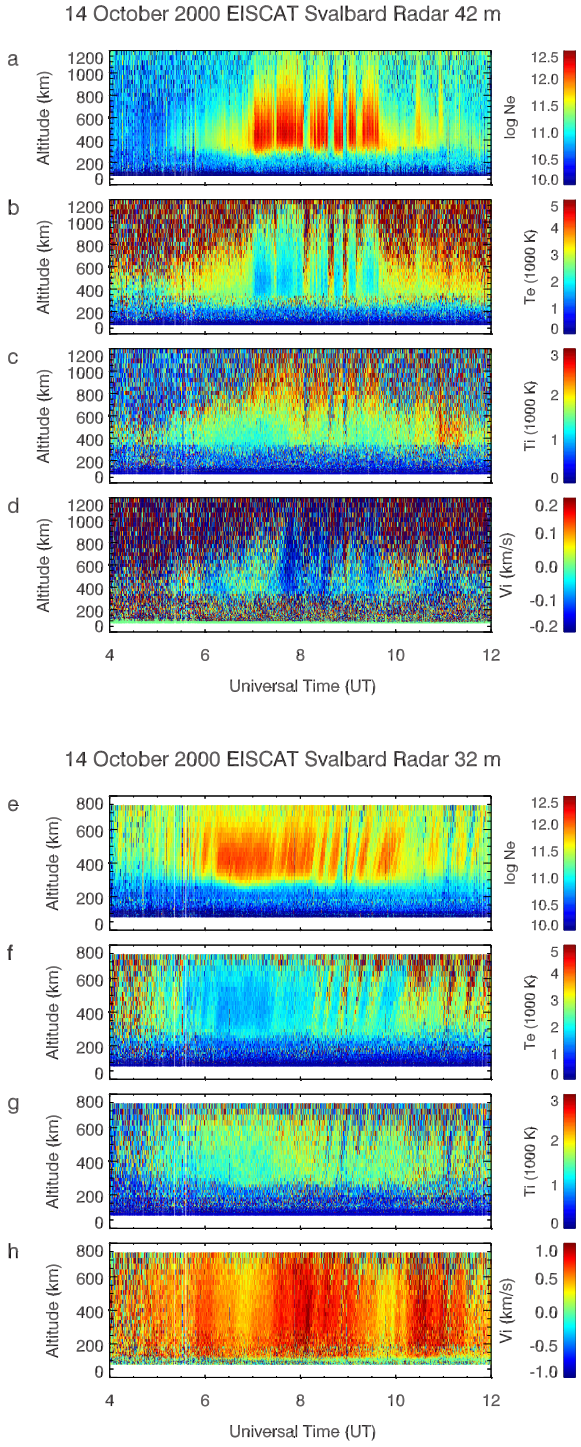

Figure 2.5: (a–d) An overview of the EISCAT Svalbard Radar 42-m antenna observation during the period from 0400 UT to 1200 UT on 14 October 2000: (a) electron density N_e, (b) electron temperature T_e, (c) ion temperature T_i, and (d) line-of-sight ion velocity V_i. (e–h) An overview of the 32-m antenna observation. The format is the same as above except for the color scale for V_i.

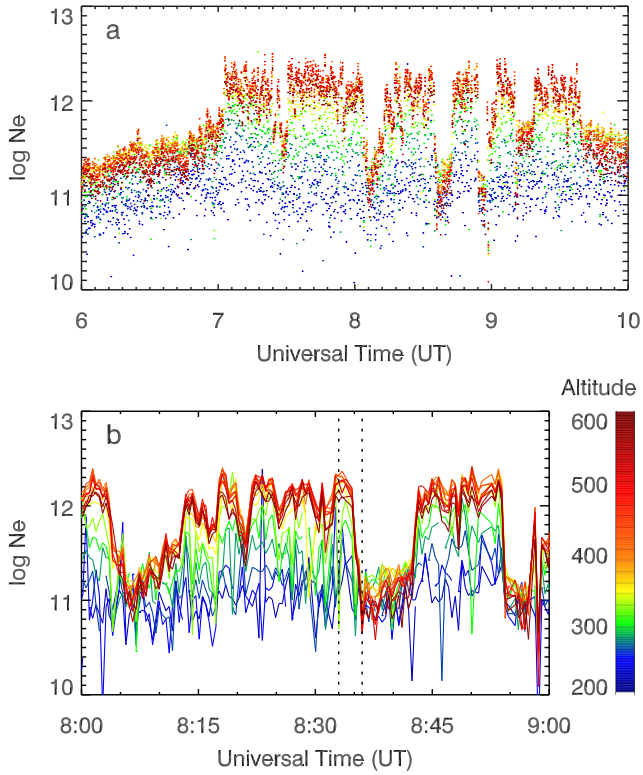

Figure 2.6: Electron density variations at various altitudes (200–600 km). (top) An interval between 0600 UT and 1000 UT, and (bottom) time-expanded (0800–0900 UT) view of the same data. Altitudes are color coded as indicated by the color bar (bottom-left). The two dotted vertical lines correspond to the two profiles in Figure 2.7.

quantitative view of the density fluctuations at various altitudes while providing the general perspective found in a summary plot such as Figure 2.5. For example, the uppermost dot represents the peak electron density ($NmF2$) and its color represents the altitude of the peak density ($hmF2$).

$NmF2$ showed the following trend. At about 0500 UT, the F-region electron density gradually began increasing from below 10^{11} m^{-3}, and by 0700 UT, it reached almost up to $\sim 10^{12}$ m^{-3}. At 0700 UT, the electron density at 439 km suddenly increased and reached a peak value of 3×10^{12} m^{-3} (i.e., $\log N_e = 12.5$). Subsequently, the peak density remained above 10^{12} m^{-3} for 24 min, and then, it decreased to 4×10^{11} m^{-3} at 0725 UT. The peak density recovered soon within 3 min; however, it again decreased and stayed at $\sim 4 \times 10^{11}$ m^{-3} until 0730 UT. During the next 33 min, the peak density remained at $\sim 2 \times 10^{12}$ m^{-3} except for one brief excursion to $\sim 6 \times 10^{11}$ m^{-3} at 0755

UT. After 0800 UT, the electron density decreased more drastically three times in 60 min; we will look into this in detail later in this section.

Figure 2.6b shows the electron density fluctuations between 0800 UT and 0900 UT in detail. The selected altitudes and their color representation are similar to those in Figure 2.6a. In this figure, we used lines, rather than dots, to emphasize the fluctuations. As mentioned above, there were three major depletions in the electron density during this period. The first major depletion occurred at 0803 UT with minimum $NmF2 \approx 1.6 \times 10^{11}$ m^{-3} at 0806 UT. The density soon began to increase gradually over $\sim$8 min before reaching 10^{12} m^{-3}. However, owing to the presence of a subsequent minor depletion and its recovery, the interval of this first major depletion is rather vague. The next major depletion, which started at 0835 UT, is more striking. First, at almost all altitudes, the electron density decreased below 10^{11} m^{-3} and remained at $\sim 2 \times 10^{11}$ m^{-3} for more than 12 min, before increasing again steeply. A significant feature of this interval is that the electron density was less variable with altitude as compared with the enhancement periods. The third major depletion, which occurred at 0854 UT, showed a behavior similar to that of the second depletion, but for a slightly shorter interval. Note that the sharp rise and fall at about 0858 UT are regarded as erroneous.

Peak altitude variation

The electron density profiles at 0833 UT and 0836 UT are shown in Figure 2.7. In Figure 2.6b, these timings are indicated by two vertical dotted lines. As mentioned above, the electron densities are less variable with height when the plasma is depleted (e.g., the profile at 836 UT). It should be noted that $hmF2$ shifted upward when the plasma enhancement occurred (e.g., the profile at 833 UT); $hmF2$ was approximately 400 km when $NmF2$ exceeded 10^{12} m^{-3}, whereas $hmF2$ was approximately 300 km when $NmF2$ was slightly above 10^{11} m^{-3}. Such characteristics can be seen in Figure 2.6b, where, at around 840 UT, the electron densities at altitudes of around 320 km

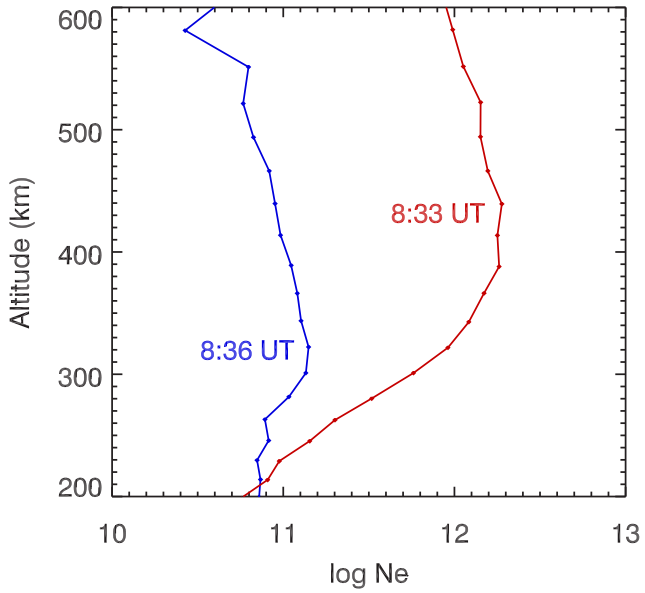

Figure 2.7: Electron density profiles of two different but close times. (red) At 0833 UT when the electron density was enhanced, and (blue) at 0836 UT when the electron density was depleted. A clear shift of hmF2 can be seen.

exceeded those at altitudes of above 400 km.

Poleward propagation of electron density structure

Figure 2.8 (top) shows a time-expanded plot of Figure 2.5e. The dotted lines represent the linear fitting of the high-density variations, which give an average propagation speed. By using these lines, we calculated the propagation speed, V_{prop}, for four particular intervals. The line plot at the bottom of Figure 2.8 shows the LOS ion drift velocity measured by the ESR 32-m antenna together with the estimated propagation speed (dotted lines). Using the LOS velocity measurement, we inferred the horizontal velocity of the moving density structure,

$$V_{hor} = \frac{V_{LOS}}{\cos 31^\circ} = 1.15 \times V_{LOS} \tag{2.1}$$

where V_{hor} is the horizontal velocity and V_{LOS} is the observed LOS velocity. Figure 2.8b indicates that the trends in V_{prop} (dotted lines) and V_{hor} are generally in good agreement. This suggests that the electron density structures were embedded in the

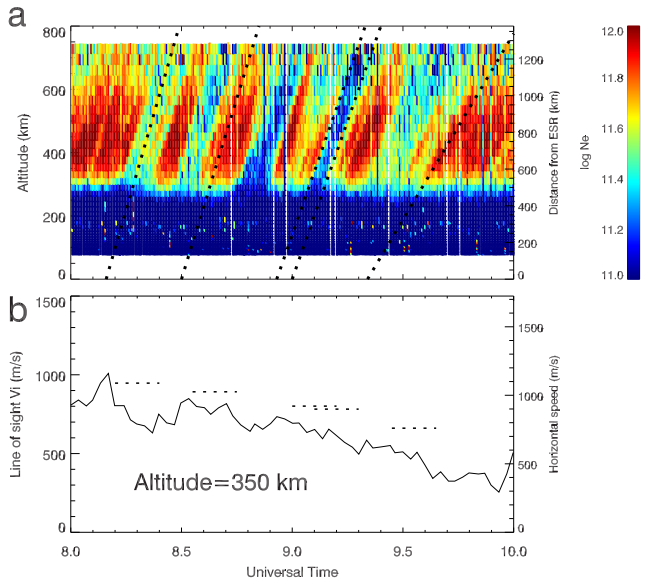

Figure 2.8: Estimation of the propagation speed of electron density structures. (top) Electron density variation observed by the ESR 32-m antenna, and (bottom) the line of sight (LOS) ion velocity at an altitude of 350 km observed by the same antenna. The dotted lines indicate the propagation speeds derived from the top panel. The label on the right vertical axis represents the inferred horizontal speed.

background convection flow. We note that the motion of the density structure would not be exactly parallel to the line of the radar beam on the horizontal plane because V_{prop} is always slightly greater than V_{hor}.

IMF and sequence of events

To investigate the relationship between the IMF and the electron density fluctuation, we estimated the lead time (propagation time from GEOTAIL to ESR) of the IMF observation as follows [e.g., *Stauning et al.*, 1995]. We divide the propagation time from GEOTAIL to ESR into four parts based on the propagation characteristics of each path:

T_1: GEOTAIL to bow shock

T_2: bow shock to magnetopause

T_3: magnetopause to cusp

T_4: cusp to ESR

As noted in Section 2.3.1, GEOTAIL was 26 R_E away from Earth at 0900 UT. We assume that the subsolar distance of the bow shock was 13 R_E, and that of the magnetopause was 10 R_E. Hence, the distance between GEOTAIL and the bow shock was 13 R_E. The x-component of the solar wind was ≈400 km/s at 0900 UT, and this results in $T_1 = 3.5$ min. From the bow shock to the magnetopause (3 R_E), where the flow becomes subsonic, we assume that the solar wind speed was ≈50 km/s, which is one-eighth of the upstream speed [*Khan and Cowley*, 1999; *Lester et al*, 1993], resulting in $T_2 = 6.4$ min. We consider $T_3 = 2$ min assuming Alfven transit between the magnetopause and the cusp [*Clauer and Banks*, 1986; *Freeman et al*, 1990]. We consider the latitude of the cusp to be 68° MLAT, as mentioned in the previous section, and the poleward plasma drift speed to be 700 m/s (Figure 2.8). The propagation time of events from the cusp to ESR, T_4, is then estimated to be 20.9 min at an altitude of 400 km. The total lead time is approximately 33 min. We note that T_4 has the widest possible range, i.e., 13 min–33 min, depending on the choice of the cusp latitude and the drift speed.

In Figure 2.9, we show the ESR 42-m observation of the electron density at an altitude of around 390 km, together with the GEOTAIL IMF observation with a propagation delay of 34 min. Except for the first depletion (at around 0730 UT), a clear correspondence can be observed between the plasma depletion and the IMF B_Y, particularly for the three depletions between 0800 UT and 0900 UT. These depletions were observed after the polarity of B_Y changed from positive to negative. We also note that these B_Y changes were accompanied by spikes in the IMF B_Z (see Figure 2.2g), although B_Z itself remained negative.

2.4 Discussion

We have presented a case of significant electron density variation in the dayside polar cap above the ESR. In order to see the significance of the event, we compare our result

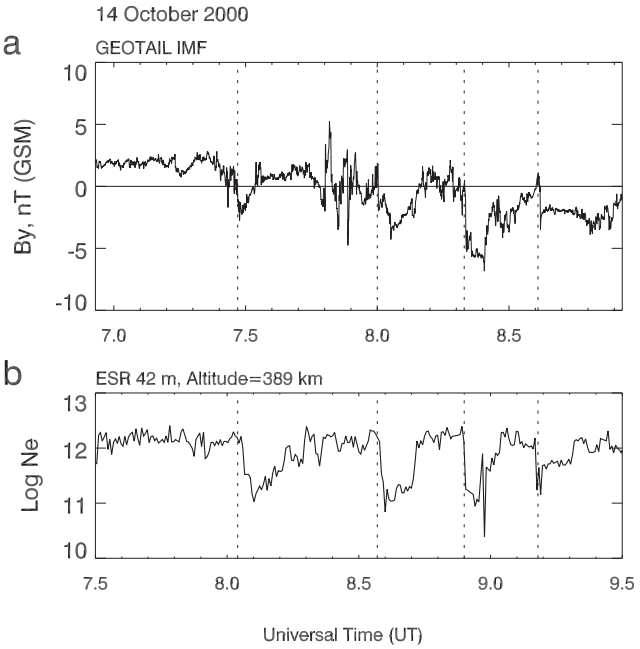

Figure 2.9: Comparison of (a) the IMF B_Y variation observed by the GEOTAIL spacecraft and (b) the electron density variation observed by ESR 42-m antenna. Propagation delay of the IMF variation from the GEOTAIL to the ESR is assumed to be 34 min, which is in good agreement with the estimation in Section 2.3.2.

with a statistical result derived by *Moen et al.* [2008] in which the diurnal $NmF2$ variation above the ESR was obtained by averaging the one-month data set taken in October 2002. As the solar activities in 2000 and 2002 were approximately the same, we use their 2002 statistics as a reference for our study. *Moen et al.* [2008] showed that the average $NmF2$ varied between 1.2×10^{11} m^{-3} and 8×10^{11} m^{-3} in October 2002. They also showed that one standard deviation range extends to 1.2×10^{12} m^{-3}. In our study, we had 3×10^{10} (at 0400 UT) $< N_e < 3 \times 10^{12}$ (0700–0900 UT). The maximum $NmF2$ on 14 October 2000 was well above the average and exceeded one standard deviation. The minimum $NmF2$ was considerably below the average and far below the lower limit of one standard deviation. In what follows, we discuss the sources of high- and low-density plasmas and their switching mechanism using a schematic illustration shown in Figure 2.10.

The reddish and bluish regions in Figure 2.10 represent high- and low-density plasma regions, respectively. We have shown that an extremely high electron den-

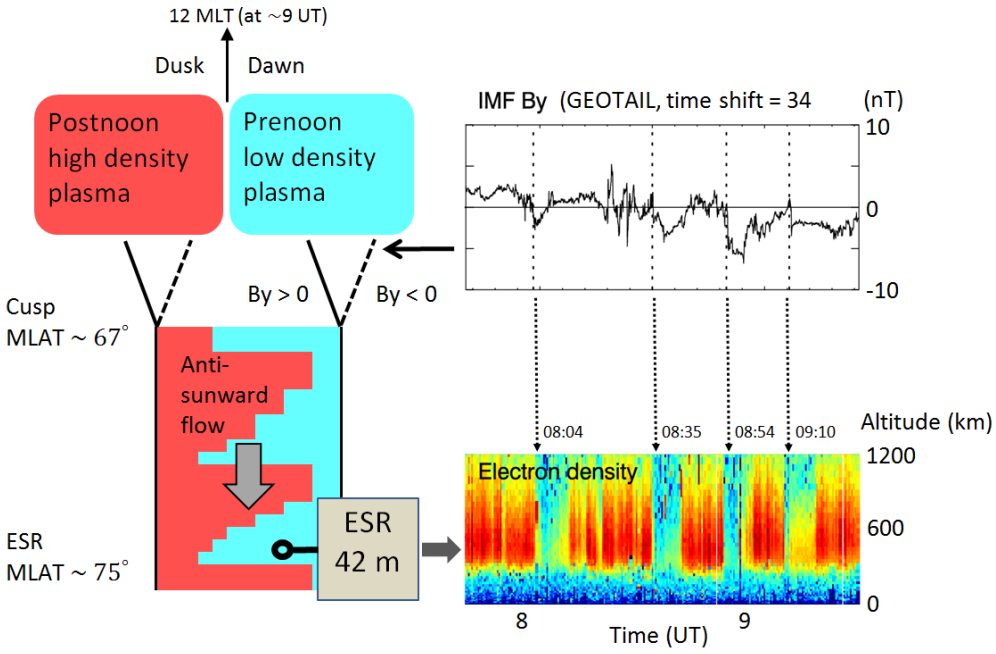

Figure 2.10: Simplified representation of the process of the ESR electron density variation event observed on 14 October 2000. Two sources of plasmas are depicted at the upper left corner. The reddish color and bluish color represent high-density plasma and low-density plasma respectively. Solid lines and dotted lines represent the shifted convection throat for different IMF B_Y conditions, i.e., solid lines for $B_Y > 0$ and dotted lines for $B_Y < 0$. The undulating boundary between the high-density plasma and low-density plasma in the anti-sunward flow, which is caused by the IMF B_Y change (upper right), is responsible for the ESR density variation (lower right).

sity was observed by ESR for approximately 3 h. The negative correlation between the electron density and the electron temperature is commonly observed in mid-latitude plasma. The plasma would be transported into the polar cap with a slight modification at the cusp by particle precipitation (Figure 2.3a). The DMSP ion density data (Figure 2.4) indicate that there was a high-density plasma region across the cusp location ($\sim$67°) at around 12:00 MLT when the IMF was southward ($B_Z < 0$). The ESR 32-m data showed a continued antisunward ion drift as well as poleward-moving electron density features. There had been a prolonged southward IMF due to a CME-driven storm [*Kataoka and Miyoshi*, 2006], which was likely to have caused stormtime enhanced density (SED). The prolonged negative B_Z also supports the occurrence of two-cell convection in which antisunward flow appears. From these observations, we infer that this high-electron-density region was a part of the TOI, i.e., sunlit plasma transported from lower latitudes by $\vec{E} \times \vec{B}$ drift, which is shown with the reddish region in Figure 2.10.

In Section 2.3.2, we described that $hmF2$ shifted upward when the electron density increased. This can be explained by plasma transportation from lower-latitude regions due to $\vec{E} \times \vec{B}$ drift. In mid-latitude regions, the geomagnetic field has a horizontal component, i.e., the $\vec{E} \times \vec{B}$ drift vector has an vertical (upward) component as well as a horizontal component. As a result, the sunlit high-density plasma is lifted during transportation to high-latitude regions before entering the polar cap region. In addition, because the rate of recombination at lower altitudes is greater than that at higher altitudes, the transportation time allows the low-altitude (<250 km) plasma to become less dense compared with the high-altitude (>250 km) plasma.

During the period of plasma enhancement, we observed sharp cutoffs of electron density, as shown in Figures 2.5. This feature was observed using both 42-m and 32-m antennas. This suggests that regions of low-density plasma were embedded in the convection flow and transported antisunward. As shown in Figure 2.4, there was a region of low-density plasma in the pre-noon sector adjacent to the region of high-

density plasma, which we attributed to a TOI. As can be seen in Figure 2.6a, the profiles of electron density in the depletion periods (e.g., at 803 UT and 836 UT) resemble the profiles of electron density at around 0600 UT. It is likely that low-density plasma, which is illustrated with the bluish region in Figure 2.10, was entrained into the convection flow from the morning sector. We do not present the detailed account of the creation of this low-density plasma in the prenoon/morning sector, but if the morning cell plasma from the nightside of the terminator has shorter exposure to sunlight than the afternoon cell plasma, presumably because of the short path on the dayside of the terminator, density depletion would occur in the prenoon/morning sector.

We now consider the process by which the high- and low-density plasmas were observed alternately in the ESR. As described in Section 2.3.2 (Figure 2.8), both high- and low-density plasmas were sequentially transported poleward while embedded in the antisunward convection flow. We need a mechanism that switches the sources of plasmas entrained into the polar cap and embeds them into the antisunward convection flow. In Figure 2.9, we have shown that the electron density decreased sharply immediately after the IMF B_Y became negative. This unprecedented clear correlation leads to the following process triggered by the change in the IMF B_Y direction.

When the direction of IMF B_Y changes from a small positive to a negative, the position of the convection throat (Figure 2.10) shifts to the prenoon sector. For example, *Zhou et al.* [2000] estimated the longitudinal (MLT) displacement of the center of the cusp to be about 30 min toward the morning sector for $B_Y \sim$ -5 nT when IMF is southward. The direction of the convection flow in the cusp/polar cap changes from northward to northeastward. Consequently, the low-density plasma originating in the morning sector is entrained into the cusp, and the dawnside boundary of TOI is deformed. When B_Y returns to a small positive, the throat region returns to the original near-noon sector so that the TOI appears over a wide extent again. This process causes the undulating boundary of the TOI, which is shown as the boundary of the reddish and bluish regions in Figure 2.10. This undulation is created in the cusp, and it would

take roughly 20 min (= T_4) to drift to the field of view of the ESR 42-m antenna, which is located in the polar cap for the present stormtime event.

We have interpreted the steep plasma depletion observed with ESR as the spatial structure of the TOI boundary. Because the typical "time rate" of the density depletion was $\sim 4 \times 10^{10}$ m^{-3} s^{-1} (Figure 2.6b), we can infer the spatial gradient of the undulating TOI boundary to be approximately $\times 10^{10}$ m^{-3} km^{-1} by using the propagation speed derived in Section 2.3.2. This means that a ten-fold change in electron density, from 10^{12} m^{-3} to 10^{11} m^{-3}, can occur within 20 km. The significance of this sharp density gradient for a rapid growth of the gradient drift instability must be studied.

2.5 Conclusions

In this chapter, we presented an ESR observation in which electron density variations showed extremely steep dropoffs several times in the dayside polar cap. The dropoffs are from 3×10^{12} m^{-3} to 1×10^{11} m^{-3}, i.e., a high-to-low ratio of 30. This ratio is much higher than that of polar patches previously reported in the literature. The dropoffs have an unprecedentedly clear one-to-one correspondence to the brief excursions of IMF B_Y to negative values. To explain the cause of these events detected by ESR measurements, we have derived the following conclusions.

1. A CME-driven storm that occurred on 12 October 2000 resulted in a period of prolonged negative IMF B_Z. This negative B_Z condition caused SED, which became the source of high-density plasma in the post-noon sector. A low-density plasma region was also created in the morning sector. As a result, there were two sources of plasmas with extremely different densities on the equatorward side of the cusp.

2. The direction of IMF B_Y changed several times between 0800 UT and 0930 UT. When B_Y was positive, the high-density plasma in the post-noon sector was entrained into the polar cap through the convection throat and formed a TOI.

When the direction of IMF B_Y changed from positive to negative, the position of the convection throat also shifted to the prenoon sector and the direction of the convection flow in the cusp/polar cap changed from northward to northeastward. Consequently, the low-density plasma originating in the morning sector was entrained into the cusp, and the dawnside boundary of TOI was deformed.

3. When B_Y returns to a small positive, the convection throat returns to the original near-noon so that TOI appears over a wider extent again. This undulation is created in the cusp, and it takes roughly 20 min to drift to the field-of-view of the ESR 42-m antenna.

Chapter 3

Storm-time enhancements of 630.0-nm airglow associated with polar cap patches

3.1 Introduction

Polar-cap patches, or patches in short, are structures of high-density plasma occasionally observed in the polar cap. They appear during both quiet and magnetically disturbed periods. Patches can be observed by the use of radio techniques such as ionosondes, incoherent scatter (IS) radars, and HF radars. At the same time, patches are observed optically at night as they emit 630.0-nm airglow. Recent advances in optical imaging technology enabled the observation of patches with high spatial and temporal resolution, thus allowing researchers to explore the detailed structure and dynamics of patches [*Shiokawa et al.*, 1999; *Shiokawa et al.*, 2009; *Hosokawa et al.*, 2013]. To investigate the structure and dynamics of polar cap patches quantitatively, it is important know the extent and velocity of a patch. To satisfy this requiremet, accurate identification of the position of a patch is necessary. In order to map an all-sky image onto a geographical plane, it is necessary to know the altitude of patch emission

[*Hosokawa et al.*, 2011], but this information can not be obtained from a single-ASI observation alone. The common practice is to assume that the emission altitude is at ∼250 km [e.g., *Hosokawa et al.*, 2009b], but that assumption could be less accurate under magnetically disturbed conditions because both the F-region ionosphere and the neutral gases in the polar cap tends to rise during magnetic storms. For example, if the actual emission peak altitude is 400 km, the above assumption will lead to a 40%-underestimation of drift velocity [e.g., *Yin et al.*, 2008], and hence of the electric field strength.

Characteristics of polar patches have been studied by many authors [see comprehensive reviews by *Crowley*, 1996; *Rodger*, 1998; *Basu and Valladares*, 1999], and it is well recognized today that knowledge of polar cap patches is important for space weather applications [e.g., *Basu et al.*, 2002; *Carlson*, 2012]. A polar cap patch is observed in the polar cap F region with typical horizontal size of ∼100 to ∼1000 km [e.g., *Coley and Heelis*, 1995]. The plasma density within a patch is often enhanced by a factor of 2–10 compared to that in the surrounding region [*Weber et al.*, 1984]. This high density plasma is plasma convected from lower latitudes [*Hosokawa et al.*, 2010], but cusp precipitation may also create isolated high-density plasma regions. Several patch-creation mechanisms have been proposed, and it is believed that they are not necessarily mutually exclusive. For example, one of the widely accepted mechanisms is that the sudden changes in east-west component of the interplanetary magnetic field (IMF B_Y) controls the entry of high-density plasma into the polar cap from lower latitude regions. Recently, *Sakai et al.* [2013] showed a clear observational evidence for the above mechanism, and showed that a sudden change of B_Y from positive to negative may result in a steep decrease in the local electron density observed by the EISCAT (European incoherent scatter) Svalbard Radar (ESR).

Polar cap patches were first studied in detail using ground-based optical instruments supplemented with other techniques such as ionosondes and satellite based plasma measurements [*Weber et al.*, 1984]. Ground-based optical measurements record the

brightness of received emission coming from luminous gas clouds that are distributed over a certain range of altitudes in the upper atmosphere. The altitude distribution of this optical emission cannot be obtained using ground-based measurements. As a result, all-sky imager data cannot determine the two-dimensional spatial extent of patches without assuming the altitude of the emission layer. Radio techniques such as the ionosonde or the IS radar provide altitude profiles of electron density of the F region, but the peak altitude of optical emission and electron density can be different. *Garner et al.* [1996] studied the altitude profile of the red-line emission from patches using the Fabry-Perot interferometer (FPI) on the Dynamic Explorer 2 spacecraft and reported that optical patches occurred in the altitude range from below 300 km to 400 km. However, the correlation between the optical peak altitude and the ionization peak was not revealed because the corresponding electron density profile was not available.

The F-region night-time airglow (or nightglow) had been studied for decades even before detailed polar patch studies were initiated [e.g., *Peterson et al.*, 1966; *Hays et al.*, 1978; and references therein]. *Barbier et al.* [1962] showed, empirically, that the brightness of 630.0-nm airglow is proportional to $(f_o\mathrm{F2})^2 \times \exp\left[-(h'\mathrm{F2} - 200)/41.3\right]$, where f_oF2 is the critical frequency of the F2 layer and h'F2 is the virtual height of the F2 layer. As $(f_o\mathrm{F2})^2$ is directly proportional to the peak electron density of the F2 layer, the above expression means that the brightness is proportional to the F2 layer density and negatively correlated to the F2 layer altitude. The brightness of the 630.0-nm airglow, I_{630}, can be calculated by integrating volume emission rate, V_{630}, along the line of sight. Several authors have used a model to simulate brightness of patches and demonstrated the relationship between brightness and ionospheric parameters [e.g., *Cogger et al.*, 1980; *Link and Cogger*, 1988; *Sobral et al.*, 1993; *Sojka et al.* 1997]. The results were presented only for limited K_p values. Although several models had been established by previous authors, there have not been systematic estimates of the patch brightness under various disturbed conditions in the polar cap. Moreover, previous studies have not demonstrated how the peak emission altitude varies under

disturbed conditions. Although the physics and chemistry of 630.0-nm airglow are well established, the storm-time behavior of the patch airglow has not been well understood. Consequently, the estimation of emission altitude is particularly challenging in the study of polar cap patches under storm conditions.

In this paper, we present observations of polar cap patches with simultaneous optical and IS radar measurements conducted during a magnetic storm on 22 January 2012. The observations were performed in Longyearbyen, Svalbard, using an all-sky imager (ASI) and the EISCAT Svalbard Radar (ESR). To provide a control case, we also show another patch event that occurred on 21 December 2011, in a relatively quiet period. These two events brought us valuable case studies because successful simulteneous observations of optical and radar patches have been rare in the polar cap. We calculated volume emission rate and brightness of patches using electron density measured by ESR and neutral gas density derived from the MSIS E90 model and compared the results with observations. The model calculation showed that the observed brightness very often exceeds the calculated brightness by a factor of two, except for periods during which the electron temperature (T_e) is relatively low. In the latter case, the results of the calculation were in good agreement with the observed, and suggest that a magnetic storm may enhance the 630.0 nm optical emission from polar cap patches.

3.2 Instrumentation and model description

3.2.1 Svalbard all sky imager and EISCAT Svalbard Radar

A highly sensitive all-sky airglow imager (ASI), located at Longyearbyen (78.2°N, 15.6°E), Svalbard, has been operational since October 2011 [*Taguchi et al.*, 2012]. The imaging device on the ASI, which is equipped with an EMCCD camera (Hamamatsu, C9100-13), has 512×512 pixels. The design of the instrument, the method of calibration, and the calibration facility are the same as detailed in [*Taguchi et al.*, 2004], and we have performed our calibration according to the procedure described in

[*Shiokawa et al.*, 2000]. Assuming the mapping altitude of 250 km, the imager has a geographical field of view (FOV) of about 800 km (with the zenith angle limit of 80°) from Longyearbyen; this FOV covers, for example, Tromsø(equatorward) and near the North Pole (poleward). At altitude of 250 km near the zenith, one pixel corresponds to a spatial extent of $\sim$ 1 km, which is comparable with the ESR beam width at 250 km. The imager has two different passband interference filters for airglow observation; one for the 630.0-nm red line and the other for the 557.7-nm green line. The imager takes 14 consecutive 630.0-nm images with an exposure time of 4 s and one 557.7-nm image with an exposure time of 1 s by rotating the filter turret and the complete cycle takes 1 min.

In this study, the 630.0-nm red-line data have been used. The imager provides high-resolution imaging capability, which enables us to study the structure of fast-moving polar cap patches [*Hosokawa et al.*, 2013]. To compare the ASI brightness data with the IS radar data from ESR, we chose an imager pixel with the same line of sight as the ESR beam. The brightness data for this specific pixel are averaged over a period corresponding to the ESR data integration period, which is typically 1 min as described below.

The EISCAT Svalbard Radar (ESR) is located at Longyearbyen, Svalbard, and is composed of two antennas: a fixed 42-m dish antenna (ESR 42 m) and a steerable 32-m dish antenna (ESR 32 m). Data obtained using the 42-m antenna are used in this study. The 42-m antenna dish is fixed so that its beam points along the field line at the ESR site.

In this study, we used the ESR data obtained on 21 December 2011 and 22 January 2012. On 21 December 2011, the 42-m antenna sampled 35 altitude ranges, which covered the altitudes from 77 km to 540 km, along the nearly vertical magnetic field line with a fixed elevation angle of 81.6°. Data processed with 64-s integration were used for our analyses. On 22 January 2012, the observed altitudes were between 77 km and 467 km with 32 samples, and the data processed with 60-s integration were used for the

analysis. In order to crosscheck the ESR electron density, the ESR peak electron density data were compared with the NmF2 data derived from the EISCAT Svalbard Ionogram (Dynasonde). The comparison showed that, for these two observation periods, the Dynasonde NmF2 was about 1.5 times larger than ESR peak electron density. Based on this, we have adjusted ESR electron density values accordingly for our brightness calculation.

3.2.2 Brightness calculation model

Model calculations are performed to estimate the volume emission rate of 630.0 nm airglow (V_{630}), which can be used to interpret the observations described below. The model is based on the following equation [*Cogger et al.*, 1980].

In this model, V_{630} is given by

$$V_{630} = 0.76\,\epsilon_1\,k_3\,[\mathrm{O}^+]\,[\mathrm{O}_2]\,D_1\,F_1\,, \tag{3.1}$$

where

$$D_1 = \frac{A_{1D}}{A_{1D} + k_2[\mathrm{N}_2]},\ A_{1D} = A_{6300} + A_{6364} \tag{3.2}$$

and

$$F_1 = \frac{\alpha_1[\mathrm{e}]}{\alpha_1[\mathrm{e}] + k_4[\mathrm{N}]}\ \approx 1. \tag{3.3}$$

The notation $[s]$, where s denotes particle species, is used to express the number density of particle s. Note that the electron density is denoted by [e], rather than N_e, in this paper. In this equation, $k_3\,[\mathrm{O}^+]$ represents production, while D_1 represents quenching. The fraction of O_2^+ ions that undergo dissociative recombination is represented by F_1, but we assume $F_1 = 1$ because F_1 is close to unity within the range of interest [*Cogger et al.*, 1980]. The relevant coefficients are summarized in Table 1 with numerical values.

Table 3.1: Coefficients used in V_{630} calculation

Coefficient	Numerical value	Related reaction
k_2	$2.30 \times 10^{-11}\mathrm{cm^3 s^{-1}}$ [(a)]	$O(^1D)+N_2 \rightarrow O(^3P)+N_2$
k_3	$1.06 \times 10^{-11}\mathrm{cm^3 s^{-1}}$ [(a)]	$O_2+O^+ \rightarrow O_2^+ + O$
ϵ	1.3 [(b)]	efficiency of $O(^1D)$ production in $O_2^+ + e \rightarrow O+O$
A_{6300}	5.63×10^{-3} [(a)]	Einstein transition coefficient for $O(^1D)$ state
A_{6364}	1.82×10^{-3} [(a)]	Einstein transition coefficient for $O(^1D)$ state
A_{1D}	7.45×10^{-3} [(a)]	$A_{1D} = A_{6300} + A_{6364}$

[(a)] [*Sobral et al.*, 1993]
[(b)] [*Hays et al.*, 1978]

V_{630} can be readily calculated for various combinations of plasma and neutral gas profiles by substituting numerical values of coefficients into the above equation. However, to illustrate the role of neutral gas profile and ion density profile in this model, we rearrange the equation as follows.

$$V_{630}(h) = \frac{A\,[O_2](h)}{1 + B[N_2](h)}\,[O^+](h) \tag{3.4}$$

where A and B are constants. Here, we explicitly introduce the variable h to express the altitude dependence of each parameter. The first part of the right-hand side (RHS) of this equation is a function of h and can be written as $G(h)$. Consequently, the altitude profile of V_{630} is expressed as

$$V_{630}(h) = G(h) \cdot [O^+](h) \tag{3.5}$$

where

$$G(h) = \frac{A\,[O_2](h)}{1 + B[N_2](h)}. \tag{3.6}$$

In this equation, $G(h)$ represents the conversion rate of airglow production, which is determined by neutral gas density profiles, $[O_2](h)$ and $[N_2](h)$. In this paper, $G(h)$ will be referred to as the rate of conversion of $[O^+]$ to V_{630}, or conversion rate for short,

whose unit is (photons) s^{-1}. In equation (5), $G(h)$ and $[O^+](h)$ respectively represent the effect of neutral atmosphere and the effect of plasma on the calculated V_{630}.

In this study, altitude profiles of neutral O_2 and N_2 are derived from MSIS E90 (available at http://omniweb.gsfc.nasa.gov/vitmo/msis_vitmo.html) for each observation period. Atomic oxygen ion density, $[O^+](h)$, is determined by the following method: the ratio of O^+ density to electron density, $[O^+]/[e]$, is derived from IRI 2012 (available at http://omniweb.gsfc.nasa.gov/vitmo/iri2012_vitmo.html); electron density is obtained from ESR observation data; the density of atomic oxygen ions is obtained via the multiplication of $[O^+]/[e]$ ratio with the observed electron density.

3.3 Observations and model calculations

In this study, we investigate the brightness of polar cap patch airglow observed during a magnetic storm on 22 January 2012. In order to provide a reference case during a relatively quiet period, we also investigate an event of successive polar cap patches observed on 21 December 2011. Figure 3.1a and 3.1b show the *Dst* indices for these two days: on the quiet day, 21 December 2011, the *Dst* index was about -10 nT, whereas on the disturbed day, 22 January 2012 the *Dst* index decreased to -70 nT.

Figures 3.2 and 3.3 show the result of observations performed on 21 December 2011 and 22 January 2012, respectively. These figures include the results of ESR observations and Svalbard ASI observations. They also contain the results of the model calculation described in 2.3. The format of these figures is explained in the caption of Figure 3.2.

3.3.1 Observation on 21 December 2011

As noted above, the *Dst* index was about -10 nT, which indicates that the observation was performed under quiet conditions. The keogram shown in Figure 3.2a indicates a series of polar cap patches passing through Longyearbyen during the 4 h period from 19 UT to 23 UT on 21 December 2011. The vertical axis represents the geographic

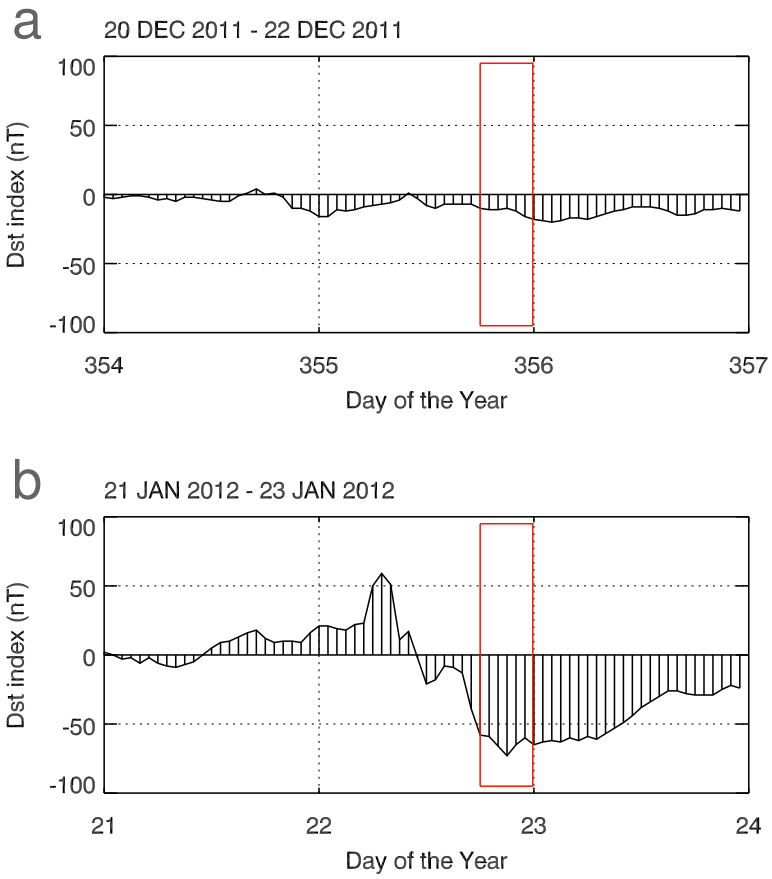

Figure 3.1: *Dst* index variations for three-day periods that include the periods of this study. (a) The quiet period from 20 December 2011 to 22 December 2011. (b) The disturbed period from 21 January 2012 to 23 January 2012.

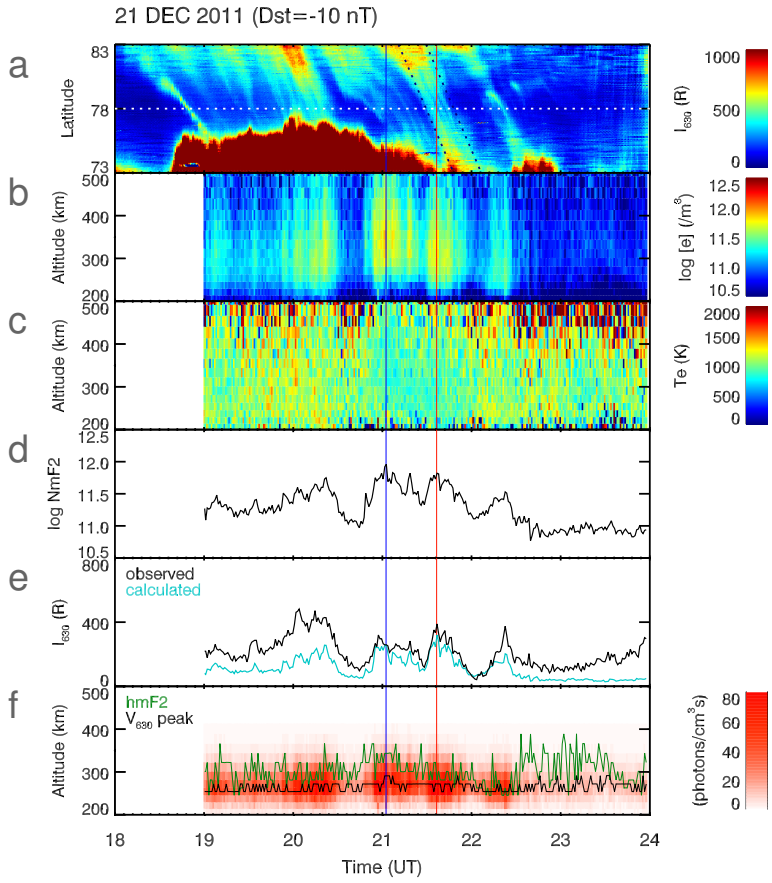

Figure 3.2: Observed and calculated results of polar cap patches on 21 December 2011 over the time period 1800 UT - 2400 UT. The EISCAT Svalbard Radar (ESR) data are available after 1900 UT. The vertical blue (2102 UT) and red (2136 UT) lines correspond to the two sample profiles in Figure 4. **(a)** A false-color north-south keogram created from the all sky imager (ASI) data. The range of geographic latitude (vertical axis) is from 73°N to 83°N. The dotted white line indicates the location where the ESR beam passes at an altitude of 250 km. Two slanted dotted lines around 2130 UT indicate the approximate boundaries of a patch. **(b)** Electron densities measured by the ESR (78°N 16°E). **(c)** Electron temperatures measured by the ESR. **(d)** F-region peak electron density (NmF2) variation derived from the ESR data. **(e)** Brightness of 630.0 nm airglow, I_{630}, measured by the ASI (black) and calculated using the model (cyan). **(f)** Height distribution of the volume emission rate, V_{630} (shaded in red), the peak altitude of the emission (black), and the F-region peak altitude, hmF2 (green).

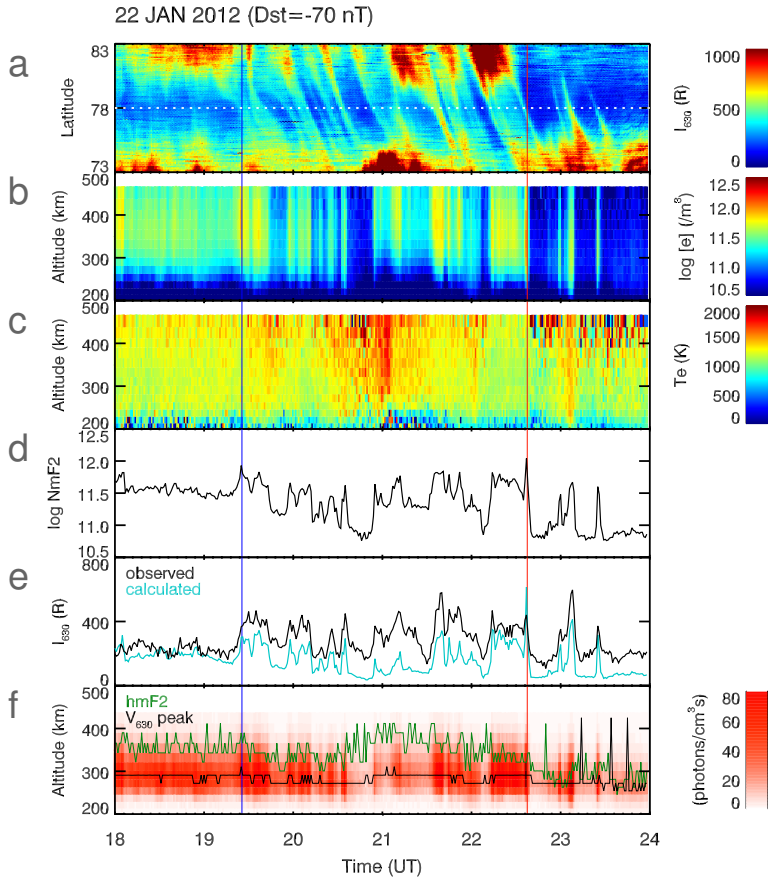

Figure 3.3: Observed and calculated results of polar cap patches on 22 January 2012 over the time period 1800 UT - 2400 UT in the same format as Figure 3.2. The vertical blue (1925 UT) and red (2237 UT) lines correspond to the two sample profiles in Figure 3.5.

latitude, and the geographic latitude of observation site (78.2° N) is marked by a white horizontal line. The latitude of the ASI field of view is determined with an assumption that the emission altitude is 250 km. Note that the meridional distance corresponding to 10° latitude is about 1150 km at an altitude of 250 km. There is a continuous high brightness region (painted in dark red, which indicates saturation) at the bottom half of the panel. This suggests that the auroral oval was situated equatorward of the observation site. The keogram contains a series of slanted stripes, which indicates a series of bright patches moved equatorward with velocities ranging from 300 m/s to 600 m/s. To determine the horizontal extent and the boundary of a patch, we tentatively define the lower limit of the brightness of an optical patch to be 200 R. According to this definition, Figure 3.2a and all-sky images (not shown) suggest that the horizontal extent of the patch observed at around 2140 UT over Longyearbyen was $\sim$ 500 km. Note that the above definition of a patch is rather arbitrary and used here only to roughly estimate the size of the patch.

As shown in Figure 3.2b, the variation of the electron density observed using ESR is generally consistent with that of brightness at geographic latitude of 78°N shown in Figure 3.2a. As the ESR data have been integrated over 1-min intervals, the time resolution of electron density data is not as fine as that of ASI data. The altitude of electron-density peak, hmF2, fluctuated between 250 km and 350 km, as shown in Figure 3.2f. The ESR electron temperature data (Figure 3.2c) indicates that the electron temperature did not increase when electron density increased significantly (e.g., around 21 UT), suggesting that the observed increase in electron density did not arise from auroral particle precipitation but was due to plasma transportation from the low temperature region. The correspondence between the brightness and electron density can be perceived clearly by comparing Figure 3.2d and Figure 3.2e. Peak electron density, NmF2, fluctuated between $\sim 6 \times 10^{11}$ m^{-3} and $\sim 10^{12}$ m^{-3} during the observation period. The observed brightness, I_{630}, plotted in black in Figure 3.2e, fluctuated between 50 R and 500 R. Except for the period between 2045 UT and 2215

UT, the observed brightness exceeded the calculated brightness significantly. We will discuss the causes of this excess brightness in 3.4.1.

The height profile plot (Figure 3.2f) of calculated volume emission rate, V_{630}, shows variations in both emission intensity and peak emission altitude. The peak emission altitude was around 260 km, which is 50 km lower than hmF2.

3.3.2 Observation on 22 January 2012

Figure 3.3 shows the results obtained during the period between 1800 UT and 2400 UT on 22 January 2012 in the same format as Figure 3.2. The geospace environment was more disturbed in this period compared with the previous case. Figure 3.3a indicates that a series of patches moved equatorward with a speed between 500 m/s and 700 m/s. These speeds were relatively faster than those observed on 21 December 2011. Note that the keogram in Figure 3.3a is created with an assumption that the emission altitude is 250 km. The figure also suggests that the poleward edge of the auroral oval, which is presented by the saturated color, was shifted equatorward to about 73°N. Similar to Figure 3.2a, the keogram shown in Figure 3.3a contains a series of stripes and each stripe has a series of finer substructures.

From Figure 3.3b, it is obvious that on 22 January 2012, F region was higher than that observed on 21 December 2011 by about 50 km. The F-layer peak altitude, hmF2, fluctuated between 300 km and 400 km before 2245 UT, and then decreased below 300 km, as shown in Figure 3.3f. The peak electron density, NmF2, fluctuated between $\sim 5 \times 10^{11}$ m^{-3} and $\sim 10^{12}$ m^{-3}, as shown in Figure 3.3d. The transient behavior of electron density variation is easily noticed.

The brightness and electron density varied almost in tandem with time, at least qualitatively, throughout the observation period. However, there were some quantitative inconsistencies between them particularly between 2030 UT and 2130 UT. The cause of the inconsistencies will be discussed in 3.4.1.

The peak emission altitude (Figure 3.3f) was around 280 km, which is about 20 km

higher than that of the quiet day, 21 December 2012. In this disturbed case, hmF2 was around 350 km, and the difference between the peak emission altitude and hmF2 was $\sim$ 70 km, which is larger than that in the quiet day. Note that the peak emission altitude is about 30 km higher than that assumed in Figure 3.3a. Hence, the speed of the equatorward motion of the patches inferred from the keogram should be corrected such that it is 12 % greater. It should be also noted that, considering the magnitude of the error, it may be necessary to reexamine the results of previous statistical studies on patch motion that assumed the emission altitude to be at $\sim$250 km [e.g., *Hosokawa et al.*, 2009b].

3.3.3 Results of model calculation

Figure 3.4 shows a summary of $V_{630}(h)$ calculation procedure for the quiet day, 21 December 2011. Figure 3.4a shows the density profile of molecular oxygen, $[O_2](h)$. Note that the production term of volume emission rate (equation (3.4)) is directly proportional to this profile. Figure 3.4b shows the density profile of molecular nitrogen, $[N_2](h)$. This density profile determines the quenching rate, $1 - D_1$, which is shown in Figure 3.4c. Figure 3.4d shows the conversion rate, $G(h)$, defined by equation (3.6). Figure 3.4e shows the electron density profiles observed by ESR at 2102 UT (in blue) and 2136 UT (in red). These two instances respectively correspond to the blue and red vertical lines in Figure 3.2. The altitude profile of the ratio of O^+ ion density to electron density, $[O^+]/[e]$, is shown in Figure 3.4f. Using the values depicted in panels e and f, the altitude profiles of $[O^+]$ at the above-mentioned instances are calculated and plotted in Figure 3.4g. Figure 3.4h shows the calculated $V_{630}(h)$ for the two instances mentioned above.

Having compared Figure 3.4 with Figure 3.5 we find that both O_2 and N_2 were lifted on the disturbed day, 22 January 2012. Table 3.2 summarizes the numerical values of $[O_2]$, $[N_2]$, and $G(h)$ at an altitude of 262 km for the quiet day and the disturbed day. For later reference, data for a severe storm event (30 Oct 2003) are also included in

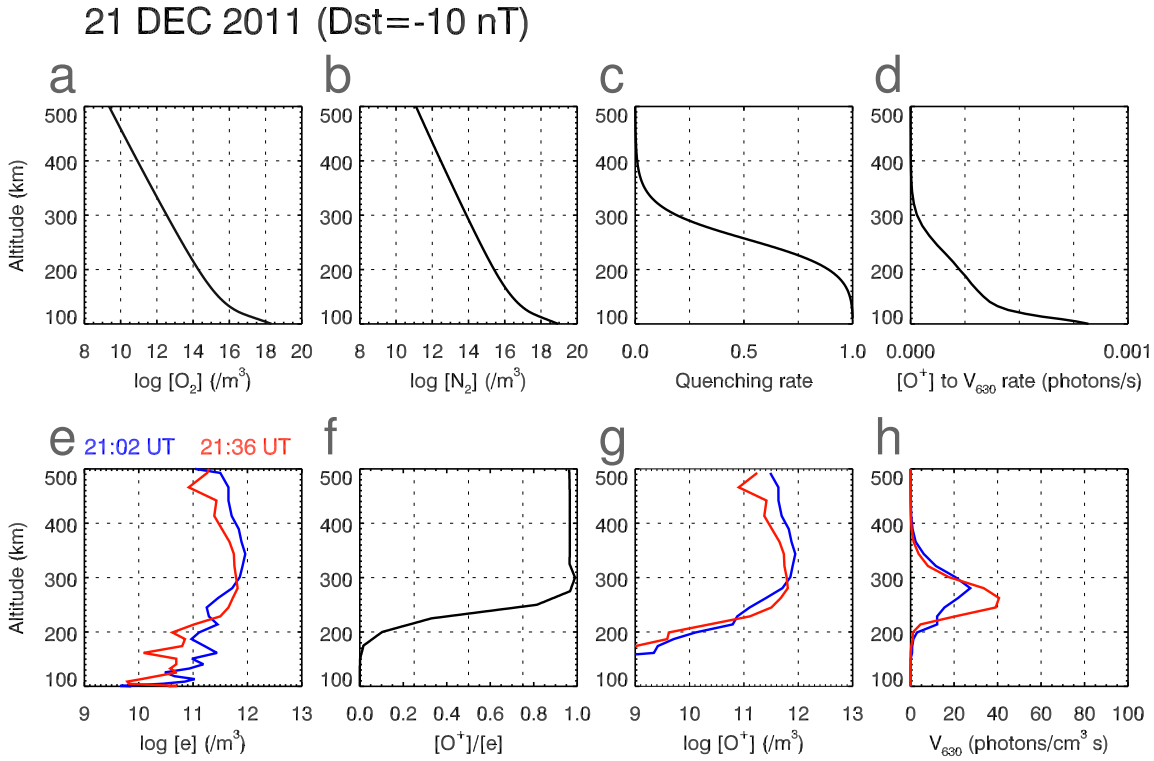

Figure 3.4: Calculation of the volume emission rate, V_{630}, for 21 December 2011. Input parameters, intermediate calculation results, and the final results are shown. All vertical axes in the figure indicate altitude in km. **(a)** Height profile of molecular oxygen density, $[O_2]$, at 2100 UT, derived from MSIS E90 model. **(b)** Height profile of molecular nitrogen density, $[N_2]$, at 2100 UT, derived from MSIS E90 model. **(c)** Rate of quenching due to molecular nitrogen, N_2. **(d)** Rate of conversion from ion density, $[O^+]$, to volume emission rate, V_{630}. **(e)** Electron density profile observed by the ESR at 2102 UT (blue) and 2136 UT (red). **(f)** Ion to electron density ratio, $[O^+]/[e]$, derived from IRI 2012 model. **(g)** Densities of atomic oxygen ion, $[O^+]$, calculated from the data in (e) and (f). Colors correspond to those in panel (e). **(h)** Volume emission rate, V_{630}. Colors correspond to those in panel (e) and (g).

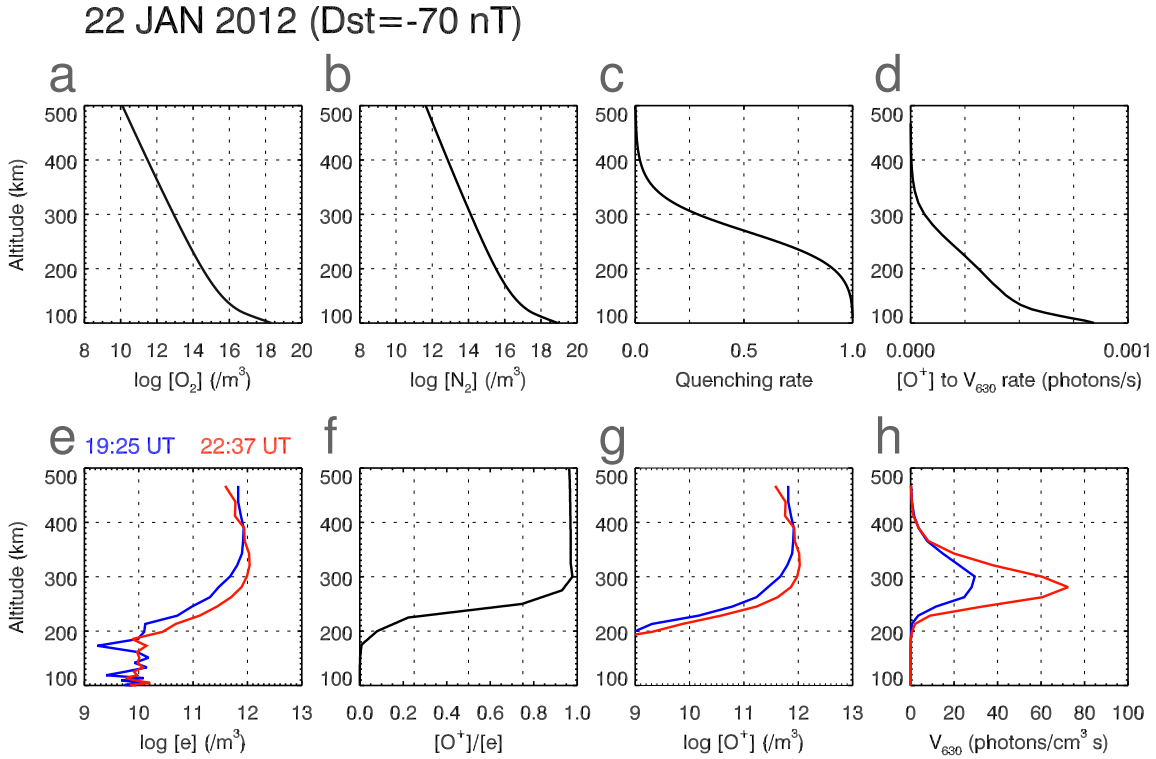

Figure 3.5: Calculation of the volume emission rate, V_{630}, for 22 January 2012. The format is the same as that for Figure 3.4. Sampled instances are 1925 UT (blue) and 2237 UT (red).

Table 3.2: Neutral gas parameters at an altitude of 262 km

Date	Oxygen $[O_2]$ (m^{-3})	Nitrogen $[N_2]$ (m^{-3})	Conversion rate $G(h)$ (photons s^{-1})
21 Dec 2011	1.5×10^{13}	2.8×10^{14}	8.5×10^{-5}
22 Jan 2012	3.2×10^{13}	4.2×10^{14}	14.4×10^{-5}
30 Oct 2003	2.5×10^{14}	1.6×10^{15}	43.5×10^{-5}

the table. The density of O_2 on the disturbed day is about 2.4 times higher than that of the quiet day, while the N_2 density on the disturbed day is about 1.7 times higher than that of the quiet day.

The F region was higher on the disturbed day (figure 3.3f). For example, at 2135 UT on 22 January 2012, the peak altitude reached above 400 km, about 50 km higher than the maximum peak altitude of high-density patches on 21 December 2011 (Figure 3.2f). Figures 3.4f and 3.5f show that the curve of $[O^+]/[e]$ ratio was also shifted upwards slightly on 22 January 2012. As a result, O^+ density profile curve for the disturbed day (Figure 3.5g) is clearly shifted upward compared with that for the quiet day (Figure 3.4g).

Figure 3.5h shows the volume emission rates at 1925 UT and 2237 UT on 22 January 2012. Although the peak O^+ density at 1925 UT is almost the same as that at 2237 UT, the volume emission rate at 1925 UT is significantly less than that at 2237 UT. This can be attributed to the difference between F-region profiles at these two instances, as shown in Figure 3.5e. Figure 3.5h also shows that the peak altitude of V_{630} shifts in accordance with the shift in F-region altitude: hmF2 at 1925 UT was about 390 km whereas hmF2 at 2237 UT was about 320 km. However, the peak altitudes of V_{630} for these two cases were almost the same, about 280 km, and this is well below the hmF2. As can be seen from Figure 3.3f, the altitude and the magnitude of airglow emission depended on both NmF2 and hmF2 as stated in Section 3.1.

The brightness of airglow, I_{630}, is calculated by integrating the volume emission rate, V_{630}, with respect to altitude, h. Lines plotted in cyan in Figures 3.2e and 3.3e represent the calculated I_{630} for the respective days. The time variation of the calculated I_{630}

is generally consistent with the observation, but there are some discrepancies between the observed brughtness and the calculated brightness.

3.4 Discussion

In the previous section, we presented observations and the results of model calculations of volume emission rate for both quiet and disturbed conditions. Comparison between two days shows that on the disturbed day (1) molecular neutral gas density has increased and the conversion rate, $G(h)$ is enhanced: (2) the altitude of the F-region peak is higher by more than 50 km, which causes the peak altitude of volume emission rate to be higher, but it is well below the F-region peak: and (3) even though the peak is higher, I_{630} is enhanced owing to the enhanced $G(h)$.

3.4.1 Differences between observations and model calculations

As mentioned in 3.3.1 and 3.3.2, the observed brightness frequently exceeded the calculated values (Figures 3.2e and 3.3e). To determine what is responsible for the inconsistencies between observation and calculation, we separate two possibilities. The first possibility is that the observed brightness consisted of 630.0 nm light from some sources other than polar patch airglow; the second possibility is that the calculated value is underestimated.

We examine the first possibility mentioned above with the aid of Figure 3.6. Other than the airglow emission from polar cap patches, the observed 630.0 nm light might have contained auroral 630.0 nm emission and lights scattered by clouds. *Meier et al.* [1989] showed that the primary processes responsible for producing $O(^1D)$ at high altitudes are direct electron impact excitation of O and dissociative recombination of O_2^+. *Roble and Rees* [1977] demonstrated that soft electron precipitation increases electron temperature in the F2 region and enhances 630.0-nm airglow emission rate. Figure 3.6a indicates that the difference between the observation and the calculation

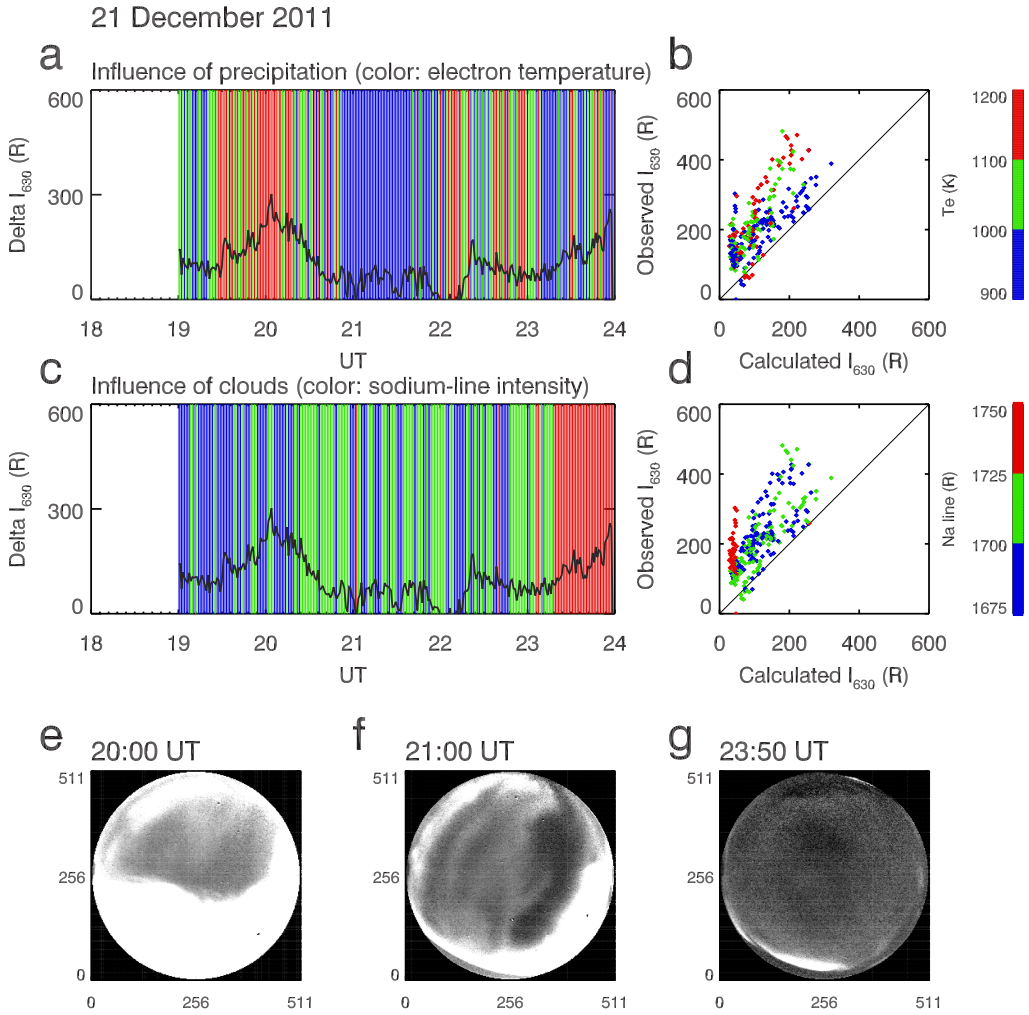

Figure 3.6: Causes of the difference between observed and calculated brightness on 21 December 2011. Panels in the first raw suggest the influence of particle precipitation to the observation. (a) Difference between the observed and the calculated brightness (ΔI_{630}). The background color represents the ESR electron temperature (T_e) averaged over an altitude range between 250 and 350 km. (b) Correlation between the observed and the calculated brightness with colors representing T_e. Panels in the second raw show the influence of cloud. (c) The same as Panel a, but the background color represents the intensity of the sodium (Na) line observed by an auroral spectrograph (ASG) in Longyearbyen. (d) The same as Panel b except for the color scheme. Third raw: All-sky images corresponding to (e) high T_e and less cloudy, (f) low T_e and less cloudy, and (g) cloudy sky periods.

(ΔI_{630}) increased when the electron temperature (T_e) increased. From this, we infer that the increase in the observed I_{630} is a signature of 630.0 nm emission originated from a region of particle precipitation. In particular, around 20 UT on 21 December 2011, the poleward boundary of the auroral oval was close to Longyearbyen (see Figure 3.2a), and it is very likely that there was significant particle precipitation in the observed region; this period coincides with the period during which ΔI_{630} increased the most. It is also possible that heat conduction from the magnetosphere increased the F region electron temperature and excited the 630.0 nm emission [*Rees and Roble*, 1975]. Whichever the case, we suppose that, in addition to dissociative recombination, thermal excitation played a significant role in enhancing the observed 630.0 nm emission during the high T_e periods. In contrast to these high T_e periods, when T_e is relatively low, the observed I_{630} approaches the calculated value. For example, on 21 December 2011, during the period between 21 UT and 22 UT, T_e was relatively low as shown in Figure 3.6a, and the calculated values were in good agreement with the observed values. During this period, the origin of observed I_{630} is likely to be patch airglow because less precipitation is expected considering the relatively low T_e. This suggests that when electron temperature is relatively low, our model calculation can be applied to estimate the profile of polar patch airglow, even though the applicable period may be short. Similarly, on 22 January 2012, T_e increased significantly when the poleward boundary of the auroral oval was close to Longyearbyen around 21 UT (Figures 3.3a and 3.3c). The period coincides with the period of increased ΔI_{630} (Figure 3.3e). As shown in Figure 3.3c, T_e was relatively low during the period between 2200 UT and 2230 UT on 22 January 2012. Figure 3.3e indicates that ΔI_{630} was relatively small during this period.

Figure 3.6a also suggests that there were some periods during which T_e was low but ΔI_{630} is large. For example, on 21 December 2011, T_e was relatively low after 2300 UT but ΔI_{630} was large. All-sky images suggest that the sky above Longyearbyen was covered with clouds during this period (Figure 3.6g compared with 6e and 6f), and

we suspect that clouds scattered auroral emission. To examine the influence of cloud quantitatively, we compared the ΔI_{630} with the sodium D line (589 nm) brightness (I_{589}) observed by an auroral spectrograph in Longyearbyen [*Taguchi et al.*, 2002]. Figure 3.6c shows that there is a clear correlation between ΔI_{630} and I_{589} after 2300 UT. Note that there is a distinct branch (in red) in Figure 3.6d. This correlation seems to suggest that the clouds affected the I_{630} observation during this period. However, as Figure 3.2c indicates, T_e at higher altitudes (above 400 km) was relatively high after 2230 UT, which suggests that there was 630.0-nm emission caused by low-energy particle precipitation at higher altitudes. Hence, we infer that precipitation played a major role in producing the excess brightness and, to some extent, clouds affected the observation. Similar conditions existed, though less distinctive, after 2230 UT on 22 January 2012.

By examining the likely causes of ΔI_{630} mentioned above, we identified the periods to investigate the characteristics of the patch airglow using model calculations. The major discrepancies can be eliminated by this process, but there is still a chance that the model has underestimated the I_{630}. Although quantitative evaluation requires further study, equation (3.5) suggests two possibilities of the underestimation. One is that the electron density measurement was inaccurate, and the other is that MSIS parameters, namely $[O_2]$ and $[N_2]$, do not represent the actual neutral gas density profiles.

3.4.2 Correlation between peak electron density and brightness

The relationship between the ionospheric electron density and airglow brightness has been studied for decades as mentioned in Section 3.1. It is known that I_{630} is positively correlated to NmF2, but negatively correlated to hmF2. However, it has not been well tested in the polar cap whether this relationship continues to hold when ionospheric conditions change. Figure 3.7a shows the correlation between NmF2 and observed I_{630}

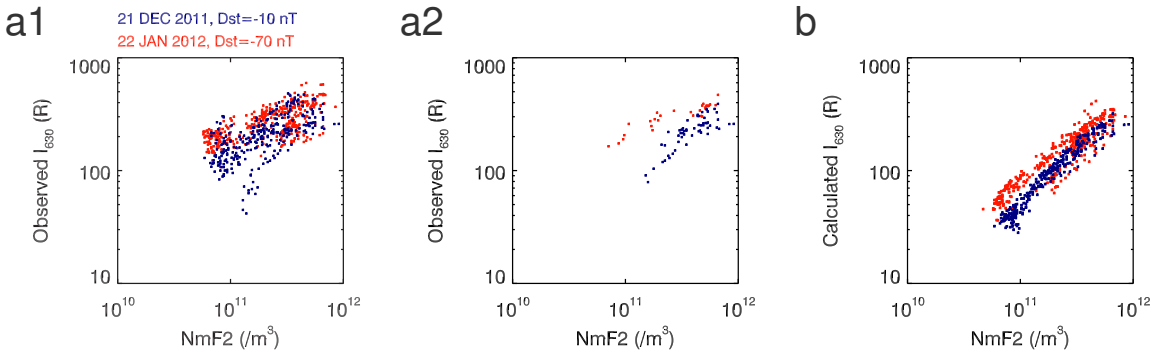

Figure 3.7: Correlation between F-region peak electron density, NmF2, and 630.0-nm airglow brightness for the quiet day (blue) and the disturbed day (red). **(a)** Observed I_{630} versus NmF2 (a1: full data points, a2: low T_e periods) **(b)** Calculated I_{630} versus NmF2.

for quiet (blue) and disturbed (red) conditions. Panel a1 shows the full data points, and a2 shows the data obtained during the low-T_e periods described in 3.4.1. The correlation between NmF2 and calculated I_{630} is shown in Figure 3.7b. These scatter plots show the positive correlation between NmF2 and I_{630}. Moreover, it is clear from the figures that, for the same electron density values, airglow becomes more intense under disturbed conditions. As shown in Figure 3.7b, our calculation indicates that disturbed-time (Dst=-70 nT) I_{630} is about 1.5-2 times larger than that of quiet time (Dst=-10 nT). It is also noted that the calculated I_{630} values are more scattered on 22 January 2012 compared with 21 December 2011. This effect can be explained by comparing hmF2 values observed on these two days. As shown in Figure 3.3f, the hmF2 fluctuated more significantly on 22 January 2012 than on 21 December 2011 (Figure 3.2f). As a result, the calculated I_{630} spread widely for same NmF2 values. This is consistent with the results shown in previous studies [*Barbier et al.*, 1962; *Sojka et al.*, 1997].

To explain the I_{630} enhancement under the disturbed conditions described above, we compare Figures 3.4d and 3.5d, which describe the altitude dependency of $[O^+]$ on V_{630} conversion rate, $G(h)$. The ratio of conversion rates (disturbed/quiet) is 1.6 at altitude 250 km, and 2.2 at 300 km. Hence, the volume emission rate is much higher on the disturbed day, as shown in Figure 3.5h, and this leads to higher brightness shown

in Figure 3.7b. As we noted in Table 3.2, at an altitude of 262 km, the density of O_2 on the disturbed day is about 2.4 times higher than that on the quiet day while the N_2 density on the disturbed day is about 1.7 times higher than that on the quiet day. Consequently, our calculation shows that $G(262\text{ km})$ is about 2.2 times larger on the disturbed day compared with the quiet day, which means that $G(262\text{ km})$ is more productive on the disturbed day, as depicted in Figure 3.5d.

The enhancement process of the airglow brightness under disturbed conditions is summarized below. First, significant energy dissipation, which is caused by enhanced energy input in the high latitude regions, heats the neutral gases in the polar cap atmosphere. This will lift the neutral gases and increase the neutral gas densities, $[O_2]$ and $[N_2]$, in the F region. Since storm-time enhancement of gas density is more significant in heavier species than in lighter species [*Prölss*, 1981], it is expected that the ratio $[O_2]_{disturbed}/[O_2]_{quiet}$ is greater than the ratio $[N_2]_{disturbed}/[N_2]_{quiet}$. From equation (3.6), this enhances $G(h)$ during a disturbed period, which means that the $[O^+](h)$ to $V_{630}(h)$ conversion rate increases. Next, under disturbed conditions, F region tends to lift. As a result, at the lower part of F region, $[O^+](h)$ decreases and consequently $V_{630}(h)$ becomes less significant in that region, as equation (3.5) suggests. Furthermore, the combination of enhanced $G(h)$ and lifted $[O^+](h)$ results in higher emission peak altitude.

3.4.3 V_{630} in severe storm conditions

The results of above two case studies suggest that polar patch airglow may significantly be enhanced during a period of severe magnetic storm. *Hosokawa et al.* [2009a] reported an event of bright 630.0 nm airglow plume with brightness of $\sim$ 1 KR under a disturbed (Dst$\approx$-146 nT) condition at Resolute Bay, Canada. *Yin et al.* [2008] showed that a series of bright ($\sim$ 1600 R) polar cap patches were observed over Qaanaaq, Greenland, during the Halloween 2003 storm. Based on the electron density observations, *Yin et al.* [2008] also suggested that the assumption of emission altitudes above

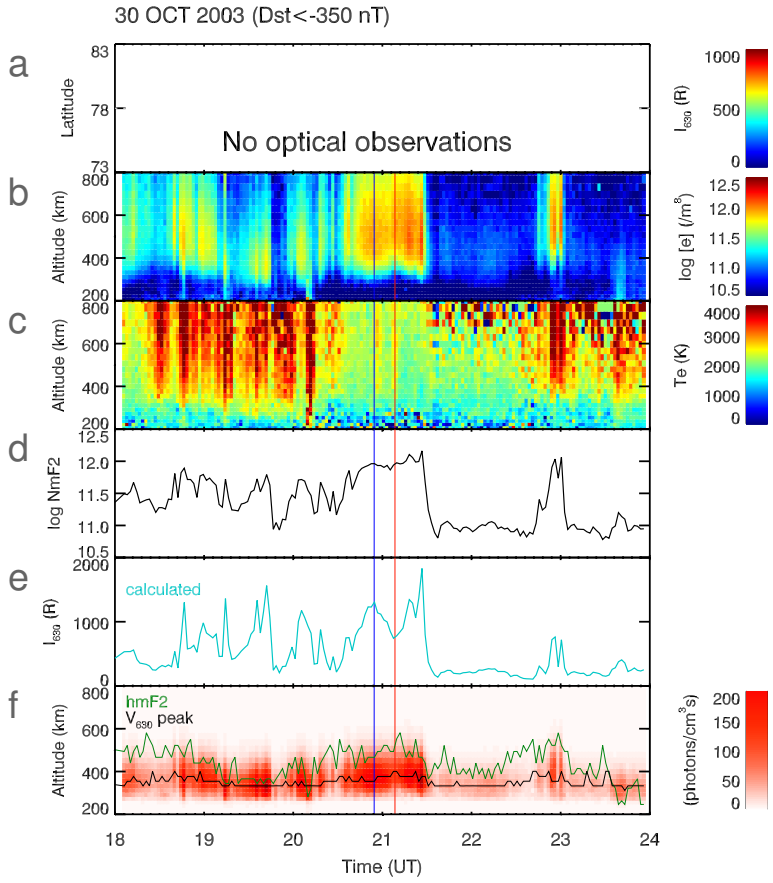

Figure 3.8: ESR observation (b and c) and calculated results of polar cap patches on 30 October 2003 over the time period 1800 UT - 2400 UT in the same format as Figure 2 except for scales. The vertical blue (2054 UT) and red (2108 UT) lines correspond to the two sample profiles in Figure 3.9

400 km was not unrealistic for that storm event.

Under severe storm conditions, neutral gas densities tend to increase significantly [*Fuller-Rowell*, 2011]. This enhances both production (by O_2) and quenching (by N_2) as described in 4.2. To investigate the altitude profile of 630.0 nm airglow under severe storm conditions, we calculated the volume emission rate, V_{630}, using the ESR electron density data obtained during the Halloween storm, of which *Dst* index values reached below -350 nT. Figures 3.8 and 3.9 show the calculation results in the same format as Figures 3.2 and 3.4, respectively. The red line in Figure 3.10a shows the calculated V_{630} for a patch observed at 2054 UT on 30 October 2003.

The results from the previous two cases are also shown in this figure. Numerical

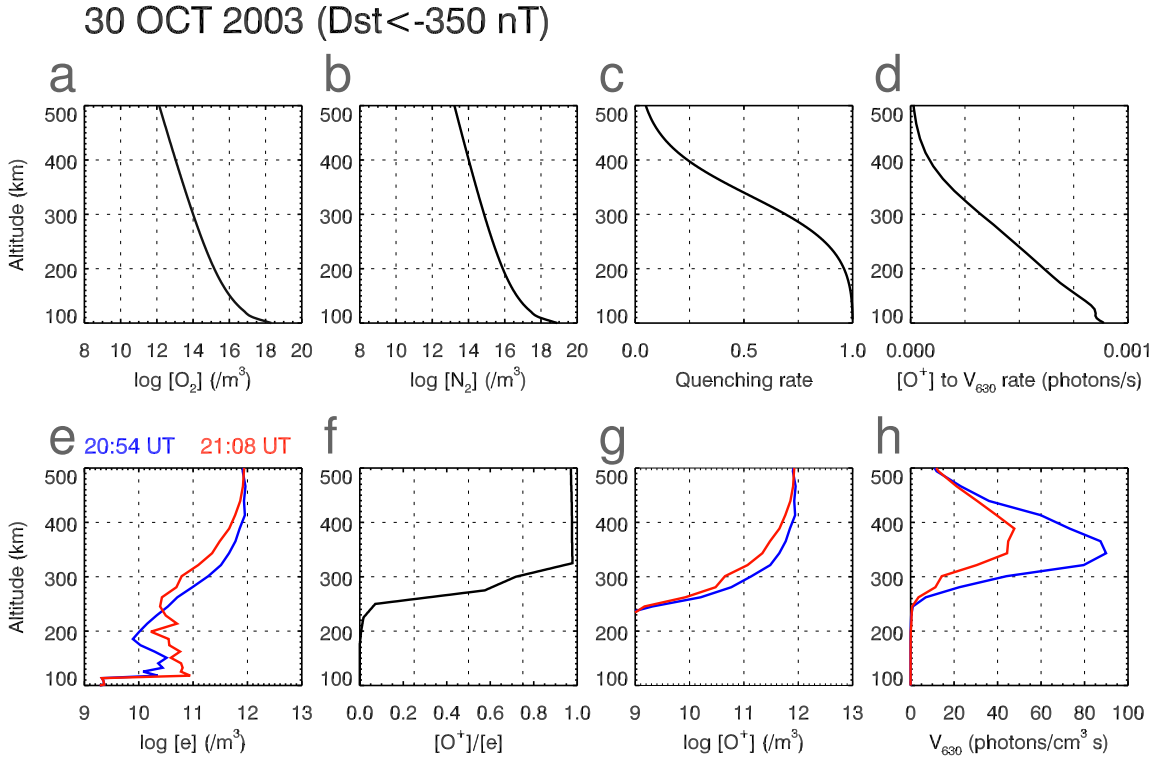

Figure 3.9: Calculation of the volume emission rate, V_{630}, for 30 October 2003. The format is the same as that for Figure 3.4. Sampled instances are 2054 UT (blue) and 2108 UT (red).

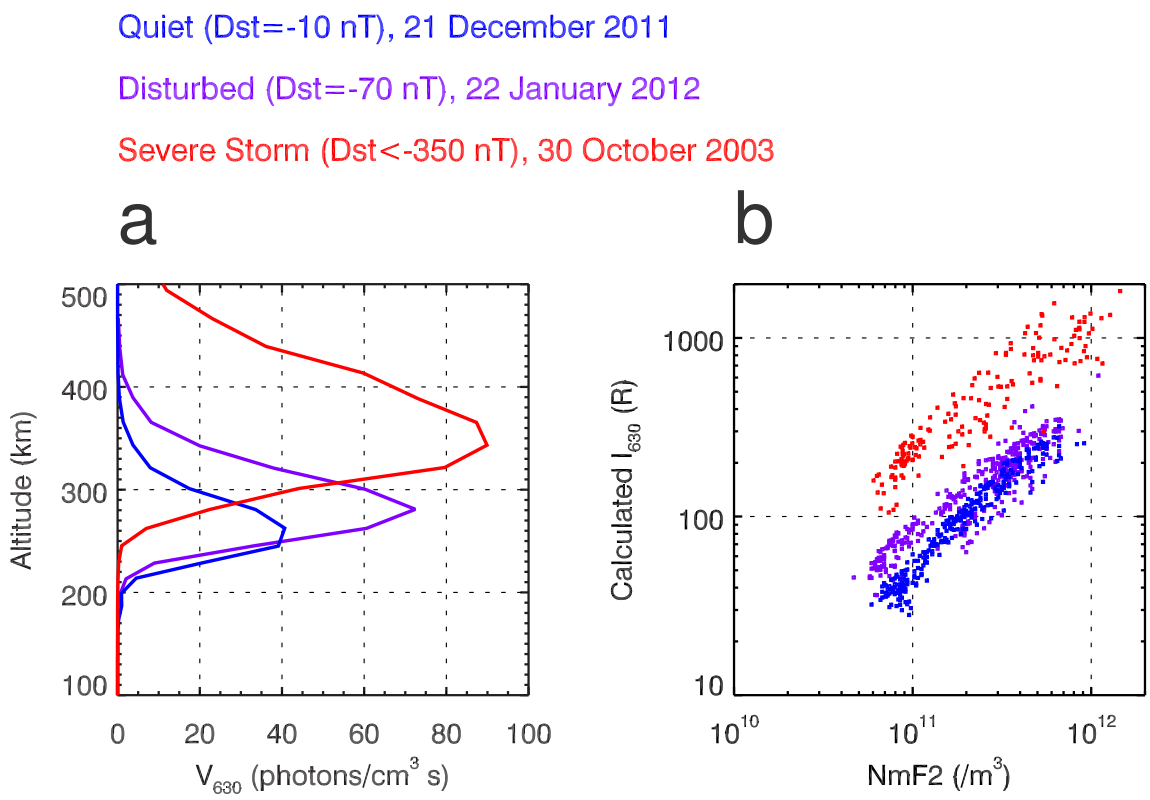

Figure 3.10: **(a)** Altitude profiles of volume emission rate calculated for quiet (blue), disturbed (violet), and severe storm (red) conditions. **(b)** Calculated I_{630} values versus NmF2 for these conditions.

Table 3.3: Typical numerical results of volume emission rate calculations

Date	Time (UT)	Dst (nT)	Peak value (photons cm^{-3})	Altitude (km)	Thickness [(a)] (km)	log NmF2 (m^{-3})	hmF2 (km)
21 Dec 2011	21:36	-10	40	260	70	11.8	280
22 Jan 2012	22:37	-70	72	280	75	12.0	320
30 Oct 2003	20:54	-350	90	340	130	11.7	410

[(a)] Full width at half maximun (FWHM) value

values are summarized in Table 3.3.

The corresponding NmF2 was close to 10^{12} m^{-3}, and hmF2 was about 410 km. As can be seen from Figure 3.9, the enhancement in V_{630} is mainly due to the uplift of neutral gases. At an altitude of 300 km, $[O_2]$ is about 29 times larger than that on the quiet day, 21 December 2011, and is about 12 times larger than that on the disturbed day, 22 January 2012. The density of molecular nitrogen, $[N_2]$, is about 9.5 times and 5.5 times larger, respectively, than that on the quiet and disturbed days. The enhancement of molecular oxygen is far more salient than the enhancement of molecular nitrogen, and this implies that production by O_2 overwhelms quenching by N_2.

The main feature of this extreme case is as follows. Firstly, the calculated dissociative-recombination emission is enhanced due to an increase not only in V_{630} but also in the thickness of emission altitudes. The peak V_{630} value reaches almost 90 photon cm^{-3} s^{-1}, which is more than twice as high as the quiet-day peak value. The emission layer is roughly 1.8 times thicker than that of the quiet day. Due to the effects of these two factors, we may expect three-fold enhancement of brightness during severe storms. Our calculation showed that the brightness, I_{630}, which is obtained by integrating V_{630} along altitude, becomes very large. The calculated I_{630} ranges from 100 R to 1830 R for an NmF2 range between 5×10^{10} m^{-3} and 1.4×10^{12} m^{-3}, as shown in Figure 3.10b. The high brightness values are consistent with the observation by *Yin et al.* [2008]. Secondly, due to the uplift of the F2 layer, the altitude of V_{630} peak moves upward to $\sim$ 350 km, which is more than 70 km higher than that of the quiet case. Noting that

this peak altitude is considerably below hmF2 (460 km), estimating emission altitudes based only on hmF2 may lead to an overestimation.

The caveat of this calculation is that we rely solely on MSIS-derived neutral parameters. It has been pointed out that MSIS may not always reproduce observed density enhancement under severely disturbed conditions [e.g., *Liu and Lühr*, 2005]. The underestimation of neutral densities may vary from a factor of 2 to 5 [*Vickers et al.*, 2013, and references therein]. A simple calculation shows that if we increase both $[O_2]$ and $[N_2]$ by a factor of N, the I_{630} enhancement is roughly proportional to $\sqrt{N}$. This means that if the MSIS underestimation factor is 5, our calculation will underestimate I_{630} by a factor of 2.2. This may be the worst case. However, our results are consistent with the observation by *Yin et al.* [2008] within a factor of 1.2, which indicates that the factor of underestimation of neutral densities is less than 1.5 in this case. To eliminate this uncertainty, future studies should address the improvement of neutral atmosphere models under magnetic storms, especially for the polar cap atmosphere.

3.5 Conclusions

In this chapter, we examined the brightness of 630.0-nm airglow, I_{630}, emitted from polar cap patches under quiet and disturbed conditions. We calculated volume emission rates of airglow, V_{630}, using electron density observed by EISCAT Svalbard Radar, molecular oxygen and nitrogen densities derived from MSIS E90 model, and O^+ density to electron density ratio derived from IRI 2012 model. The results are summarized in Table 3.3, as mentioned in 4.3. Brightness was calculated by integrating the volume emission rate along altitude, and the results were compared with the all-sky imager observations. We found that the observed brightness was often much higher than the calculated brightness due to the extra emission caused by particle precipitation. However, in limited periods when there was less particle precipitation, the results of model calculation were consistent with the observations, both in the quiet and the

disturbed periods.

From these investigations, we have derived the following conclusions. Under the magnetically disturbed conditions during our observations, the model calculation showed that (1) the altitude of V_{630} peak increases, (2) the thickness of the emission layer increases, and (3) patch brightness increases. Unstructured particle precipitation may increase observed brightness, which is comparable with the patch brightness. If electron temperature data are available, it is possible to determine whether there is extra emission due to precipitation. This is particularly important when interpreting the patch brightness data taken in the polar cap.

Chapter 4

Concluding remarks

Summary of the research. In the previous two chapters, we have described some notable features of the polar-cap ionosphere under magnetically disturbed conditions. We studied the plasma density in the dayside polar cap in Chapter 2, and we investigated the airglow brightness and the plasma density in the night-side polar cap in Chapter 3.

In Chapter 2, we investigated a horizontal structure of dayside polar cap ionosphere during a magnetic storm. A series of steep plasma depletions was observed in the dayside polar cap during an interval of highly enhanced electron density through EISCAT Svalbard Radar (ESR) measurements. Each depletion started with a steep decrease of electron density at F2 region altitudes, and it continued for 10 - 15 min before returning to the enhanced level. These depletions moved poleward at a speed consistent with the observed ion drift velocity. DMSP spacecraft observations indicate that a region of high ion densities extended into the polar cap from the equatorward side of the cusp, and that the ion densities were very low on its prenoon side. Solar wind observations show that a sharp changes in IMF B_Y polarity is associated with an sharp decrease of electron density. These facts present the first observational evidence for some of the previously speculated theories on patch formation. We also proposed an additional scenario that the series of plasma density depletions is a result of the poleward drift of

the undulating boundary of the tongue of ionization.

In Chapter 3, we studied the vertical structures of both neutral and ionized gases in the polar cap. We examined the brightness of 630.0-nm airglow, I_{630}, associated with polar cap patches observed during a magnetic storm using an all sky imager (ASI) in Svalbard. The observed I_{630} showed a good correlation with the F-region electron density observed by ESR. To estimate the brightness and the altitude of the airglow, we performed model calculations of the volume emission rate, V_{630}, under quiet and disturbed conditions, using MSIS-modelled neutral gas profiles and the electron density profile obtained from the ESR data. The calculations revealed that, under disturbed conditions, (1) the altitude of V_{630} peak is increased, (2) the thickness of the emission layer is increased, and (3) the magnitude of V_{630} peak is increased. The results clearly show the previously unknown vertical structure of polar-patch airglow under magnetic storms.

Future research. As explained in 1.4.5, ionospheric plasma in the dayside polar cap is transported to the nightside polar cap within a few hours, during which the density of F-region plsama is considered not to decrease significantly. It is expected that extremely large-amplitude changes in plasma density in the dayside polar cap, such as that observed on 14 October 2002 (Chapter 2), can propagate across the polar cap and can be observed in the nightside, either optically or with IS radars. If we can trace a plasma plume from dayside entry near the cusp to nightside exit, our understanding of the polar-cap ionosphere will be greatly improved (Figure 1.13). Firstly, we will be able to picture the life of a polar cap patch, which has been partially understood to date. Secondly, we will be able to estimate the decay of the patch during the transportation from the dayside to the night-side polar cap, and on the sunward return flow after exiting from the polar cap. This will give us an improved overall picture of ionospheric convection. Thirdly, we are particularly interested in the lifelong process of plasma irregularities associated with steep densty gradient of polar patches. The

study of these irregularities is an important topic of ionospheric physics in connection with plasma instabilities. It will also give a sound basis for the improvement of the accuracy of GPS navigation in the polar region and the quality of trans-polar radio communications.

References

[*Baumjohann and Treumann* (1997)] Baumjohan, W., and R. Treumann (1997) *Basic Space Plasma Physics,* Imperial College Press, London, UK.

[*Barbier et al.* (1962)] Barbier, D., F. E. Roach, and W. R. Steiger (1962), The summer intensity variations of [OI] 6300 Å in the tropics, *J. Res. NBS – D. Radio Propagation, 66D*(1), 145–152.

[*Basu and Valladares* (1999)] Basu, S., and C. Valladares (1999), Global aspects of plasma structures, *J. Atmos. Terr. Phys., 61*, 127–139.

[*Basu et al.* (2002)] Basu, S., K. M. Grovesa, Su. Basu, and P. J. Sultan (2002), Specification and forecasting of scintillations in communication/navigation links: Current status and future plans, *J. Atmos. Sol. Terr. Phys., 64*, 1745.

[*Campbell* (2003)] Campbell, W. H. (2003) *Introduction to Geomagnetic Fields,* Cambridge University Press, Cambridge, UK.

[*Carlson* (2012)] Carlson, H. C. (2012), Sharpening our thinking about polar cap ionospheric patch morphology, research, and mitigation techniques, *Radio Sci., 47*, RS0L21, doi:10.1029/2011RS004946.

[*Chapman* (1950)] Chapman, S. (1950) Upper atmospheric nomenclature, *J. Atmos. Sol. Terr. Phys., 1*(2), 121–124, ISSN 0021-9169, doi:10.1016/0021-9169(50)90026-2.

[*Chen* (1974)] Chen, F. F. (1974), *Introduction to plasma physics,* Plenum Press, New York, USA.

[*Clauer and Banks* (1986)] Clauer, C. R., and P. M. Banks (1986), Relationship of the interplanetary electric field to the high-latitude ionospheric electric field and currents: Observations and model simulation, *J. Geophys. Res., 91*(A6), 6959–6971, doi:10.1029/JA091iA06p06959.

[*Cogger et al.*(1980)] Cogger, L. L., J. C. G. Walker, J. W. Meriwether Jr., and R. G. Burnside (1980), F region airglow: Are ground-based observations consistent with recent satellite results?, *J. Geophys. Res., 85*(A6), 3013–3020, doi:10.1029/JA085iA06p03013

[*Coley and Heelis* (1995)] Coley, W. R., and R. A. Heelis (1995), Adaptive identification and characterization of polar ionization patches, *J. Geophys. Res., 100*(A12), 23,819–23,827, doi:10.1029/95JA02700.

[*Cowley et al.* (1991)] Cowley, S. W. H., J. P. Morelli, and M. Lockwood (1991), Dependence of convective flows and particle precipitation in the high-latitude dayside ionosphere on the X and Y components of the interplanetary magnetic field, *J. Geophys. Res., 96*, 5557–5564, doi:10.1029/90JA02063.

[*Crowley* (1996)] Crowley, G. (1996), Critical review of ionospheric patches and blobs, in *Review of Radio Science 1993-1996*, edited by W. R. Stone, pp.619–648, Oxford University Press, Oxford, U.K.

[*Dungey* (1961)] Dungey, J. W. (1961), Interplanetary magnetic field and the auroral zones, *Phys. Rev. Lett., 6*(47).

[*Foster* (1984)] Foster, J. C. (1984), Ionospheric signatures of magnetospheric convection, *J. Geophys. Res., 89*(A2), 855–865, doi:10.1029/JA089iA02p00855.

[*Foster* (1993)] Foster, J. C. (1993), Storm time plasma transport at middle and high latitudes, *J. Geophys. Res., 98*(A2), 1675–1689, doi:10.1029/92JA02032.

[*Foster and Burke* (2002)] Foster, J. C., and W. J. Burke (2002), SAPS: A new characterization for sub-auroral electric fields, *EOS*, *83*, 393-394, 2002.

[*Foster* (2005)] Foster, J. C., et al. (2005), Multiradar observations of the polar tongue of ionization, *J. Geophys. Res., 110*, A09S31, doi:10.1029/2004JA010928.

[*Freeman et al.* (1990)] Freeman, M. P., C. J. Farrugia, S. W. H. Cowley, and A. Etemadi (1990), The response of dayside ionospheric convection to the Y-component of the magnetosheath magnetic field: A case study, *Planet. Space Sci., 38*, 1,13–41.

[*Fuller-Rowell*(2011)] Fuller-Rowell, T. J. (2011), Storm-time response of the thermosphere-ionosphere system, in *Aeronomy of the Earth's Atmosphere and Ionosphere*, edited by M. A. Abdu, D. Pancheva, co-edited by A. Bhattacharyya, pp.419–435, Springer, doi:10.1007/978-94-007-0326-1_32.

[*Garner et al.*(1996)] Garner, T. W., T. L. Killeen, A. G. Burns, J. D. Winningham, and W. R. Coley (1996), Examination of the oxygen red line signature of a polar cap ionization patch as seen from the Dynamics Explorer 2 satellite, *Radio Sci., 31*(3), 607–618, doi:10.1029/96RS00617.

[*Hays et al.*(1978)] Hays, P. B., D. W. Rusch, R. G. Roble, and J. C. G. Walker (1978), The O I (6300 Å) airglow, *Rev. Geophys., 16*(2), 225–232, doi:10.1029/RG016i002p00225.

[*Heelis* (1984)] Heelis, R. A. (1984), The effects of interplanetary magnetic field orientation on dayside high-latitude ionospheric convection, *J. Geophys. Res., 89*(A5), 2873–2880, doi:10.1029/JA089iA05p02873.

[*Heppner and Maynard* (1987)] Heppner, J. P., and N. C. Maynard (1987), Empirical high-latitude electric field models, *J. Geophys. Res., 92*(A5), 4467–4489, doi:10.1029/JA092iA05p04467.

[*Hosokawa et al.*(2009a)] Hosokawa, K., T. Tsugawa, K. Shiokawa, Y. Otsuka, T. Ogawa, and M. R. Hairston (2009a), Unusually elongated, bright airglow plume in the polar cap F region: Is it a tongue of ionization? *Geophys. Res. Lett., 36*, L07103, doi:10.1029/2009GL037512.

[*Hosokawa et al.*(2009b)] Hosokawa, K., T. Kashimoto, S. Suzuki, K. Shiokawa, Y. Otsuka, and T. Ogawa (2009b), Motion of polar cap patches: A statistical study with all-sky airglow imager at Resolute Bay, Canada, *J. Geophys. Res., 114*, A04318, doi:10.1029/2008JA014020.

[*Hosokawa et al.*(2010)] Hosokawa, K., T. Tsugawa, K. Shiokawa, Y. Otsuka, N. Nishitani, T. Ogawa, and M. R. Hairston (2010), Dynamic temporal evolution of polar cap tongue of ionization during magnetic storm, *J. Geophys. Res., 115*, A12333, doi:10.1029/2010JA015848.

[*Hosokawa et al.*(2011)] Hosokawa, K., J. I. Moen, K. Shiokawa, and Y. Otsuka (2011), Decay of polar cap patch, *J. Geophys. Res., 116*, A05306, doi:10.1029/2010JA016297.

[*Hosokawa et al.*(2012)] Hosokawa K., S. Taguchi, Y. Ogawa, and T. Aoki (2012), Periodicities of polar cap patches, *J. Geophys. Res. Space Physics, 118*, 447–453, doi:10.1029/2012JA018165.

[*Hosokawa et al.*(2013)] Hosokawa K., S. Taguchi, Y. Ogawa, and T. Aoki (2013), Periodicities of polar cap patches, *J. Geophys. Res. Space Physics, 118*, 447–453, doi:10.1029/2012JA018165.

[*Kataoka and Miyoshi* (2006)] Kataoka, R., and Y. Miyoshi (2006), Flux enhancement of radiation belt electrons during geomagnetic storms driven by coronal mass ejections and corotating interaction regions, *Space Weather, 4*, S09004, doi:10.1029/2005SW000211.

[*Khan and Coeley* (1999)] Khan, H., and S. W. H. Cowley (1999), Observations of the response time of high-latitude ionospheric convection to variations in the interplan-

etary magnetic field using EISCAT and IMP-8 data, *Ann. Geophys., 17*, 1306-1335, doi:10.1007/s00585-999-1306-8.

[*Lester et al.* (1993)] Lester, M., O. de la Beaujardiere, J. C. Foster, M. P. Freeman, H. Luehr, J. M. Ruohoniemi, and W. Swider (1993), The response of the large scale ionospheric convection pattern to changes in the IMF and substorms: Results from the SUNDIAL 1987 campaign, *Ann. Geophys., 11*, 556.

[*Link and Cogger*(1988)] Link, R. and L. L. Cogger (1988), A reexamination of the O I 6300-A nightglow, *J. Geophys. Res., 93*(A9), 9883–9892, doi:10.1029/JA093iA09p09883.

[*Liu and Lühr*(2005)] Liu, H., and H. Luhr (2005), Strong disturbance of the upper thermospheric density due to magnetic storms: CHAMP observations, *J. Geophys. Res., 110*, A09S29, doi:10.1029/2004JA010908.

[*Lockwood and Carlson* (1992)] Lockwood, M. and H. C. Carlson Jr. (1992), Production of polar cap electron density patches by transient magnetopause reconnection, *Geophys. Res. Lett., 19*(17), 1731–1734, doi:10.1029/92GL01993.

[*Meier et al.*(1989)] Meier, R. R., D. J. Strickland, J. H. Hecht, and A. B. Christensen (1989), Deducing composition and incident electron spectra from ground-based auroral optical measurements: A study of auroral red line processes, *J. Geophys. Res., 94*(A10), 13541–13552, doi:10.1029/JA094iA10p13541.

[*Milan et al.* (2002)] Milan, S. E., M. Lester, and T. K. Yeoman (2002), HF radar polar patch formation revisited: Summer and winter variations in dayside plasma structuring, *Ann. Geophys., 20*, 487–499, doi:10.5194/angeo-20-487-2002.

[*Moen et al.* (2008)] Moen, J., X. C. Qiu, H. C. Carlson, R. Fujii, and I. W. McCrea (2008), On the diurnal variability in F2-region plasma density above the EISCAT Svalbard radar, *Ann. Geophys., 26*, 2427–2433, doi:10.5194/angeo-26-2427-2008.

[*Newell et al.* (1989)] Newell, P. T., C.-I. Meng, D. G. Sibeck, and R. Lepping (1989), Some low-altitude cusp dependencies on the interplanetary magnetic field, *J. Geophys. Res., 94*(A7), 8921–8927, doi:10.1029/JA094iA07p08921.

[*Newell and Meng* (1988)] Newell, P. T., and C. .-I. Meng (1988), The cusp and the cleft/boundary layer: Low-altitude identification and statistical local time variation, *J. Geophys. Res., 93*(A12), 14,549–14,556, doi:10.1029/JA093iA12p14549.

[*Oksavik et al.* (2010)] Oksavik, K., V. L. Barth, J. Moen, and M. Lester (2010), On the entry and transit of high-density plasma across the polar cap, *J. Geophys. Res., 115*, A12308, doi:10.1029/2010JA015817.

[*Peterson et al.*(1966)] Peterson, V. L., T. E. VanZandt, and R. B. Norton (1966), F-region nightglow emissions of atomic oxygen: 1. Theory, *J. Geophys. Res., 71*(9), 2255–265, doi:10.1029/JZ071i009p02255.

[*Prölss*(1981)] Prölss, G. W. (1981), Latitudinal structure and extension of the polar atmospheric disturbance, *J. Geophys. Res., 86*(A4), 2385–2396, doi:10.1029/JA086iA04p02385.

[*Prölss*(1995)] Prölss, G. W. (1995), Ionospheric F-Region Storms, in *Handbook of atmospheric electrodynamics*, edited by H. Volland, pp.195–248, CRC Press, Boca Raton, USA, ISBN:0-8493-2520-X

[*Rees and Roble*(1975)] Rees, M. H., and R. G. Roble (1975), Observations and theory of the formation of stable auroral red arcs, *Rev. Geophys., 13*(1), 201–242, doi:10.1029/RG013i001p00201.

[*Rishbeth and Garriot*(1969)] Rishbeth, H.,and O. Garriot (1969), *Introduction to Ionospheric Physics,* Academic Press, New York, USA

[*Roble and Rees*(1977)] Roble, R.G. and M.H. Rees (1977), Time-dependent studies of the aurora: Effects of particle precipitation on the dynamic morphology of ionospheric and atmospheric properties, *Planet. Space Sci., 25*(11), 991–1010.

[*Rodger*(1998)] Rodger, A. S. (1998), Polar patches - outstanding issues, in *Polar Cap Boundary Phenomena*, edited by J. Moen, A. Egeland and M. Lockwood, pp.281–288, Kluwer Academic Publishers, Dordrecht, Netherlands.

[*Sakai et al.*(2013)] Sakai, J., S. Taguchi, K. Hosokawa, and Y. Ogawa (2013), Steep plasma depletion in dayside polar cap during a CME-driven magnetic storm, *J. Geophys. Res. Space Physics, 118*, 462–471, doi:10.1029/2012JA018138.

[*Sato* (1959)] Sato, T. (1959), Morphology of ionospheric F2 disturbances in the polar regions, A linkage between polar patches and plasmaspheric drainage plumes, *Rep. Ionos. Res. Space Res. Jpn., 131*, 91.

[*Schunk et al.* (1975)] Schunk, R. W., W. J. Raitt, and P. M. Banks (1975), Effect of electric fields on the daytime high-latitude E and F regions, *J. Geophys. Res., 80*(22), 3121–3130, doi:10.1029/JA080i022p03121.

[*Shiokawa et al.*(1999)] Shiokawa, K., Y. Katoh, M. Satoh, M. K. Ejiri, T. Ogawa, T. Nakamura, T. Tsuda, and R. H. Wiens (1999), Development of optical mesosphere thermosphere imagers (OMTI), *Earth Planets Space, 51*, 887.

[*Shiokawa et al.*(2000)] Shiokawa, K., Y. Katoh, M. Satoh, M.K. Ejiri, and T. Ogawa (2000), Integrating-sphere calibration of all-sky cameras for nightglow measurements, *Adv. Space Res., 26* (6), 1025–1028, doi: 10.1016/S0273-1177(00)00052-1.

[*Shiokawa et al.*(2009)] Shiokawa, K., Y. Otsuka, and T. Ogawa (2009), Propagation characteristics of nighttime mesospheric and thermospheric waves observed by optical mesosphere thermosphere imagers at middle and low latitudes, *Earth Planets Space, 61*, 479.

[*Sobral et al.*(1993)] Sobral, J. H. A., H. Takahashi, M. A. Abdu, P. Muralikrishna, Y. Sahai, C. J. Zamlutti, E. R. de Paula, and P. P. Batista (1993), Determination of the quenching rate of the O(1D) by O(3P) from rocket-borne optical (630 nm) and electron density data, *J. Geophys. Res., 98*(A5), 7791–7798, doi:10.1029/92JA01839.

[*Sojka et al.* (1994)] Sojka, J. J., M. D. Bowline, and R. W. Schunk (1994), Patches in the polar ionosphere: UT and seasonal dependence, *J. Geophys. Res., 99*(A8), 14,959–14,970, doi:10.1029/93JA03327.

[*Sojka et al.*(1997)] Sojka, J. J., R. W. Schunk, M. D. Bowline, and D. J. Crain (1997), Ambiguity in identification of polar cap F-region patches: contrasting radio and optical observation techniques, *J. Atmos. Sol. Terr. Phys., 59*(2), 249–258.

[*Stauning et al.* (1995)] Stauning, P., C. R. Clauer, T. J. Rosenberg, E. Friis-Christensen, and R. Sitar (1995), Observations of solar-wind-driven progression of interplanetary magnetic field BY-related dayside ionospheric disturbances, *J. Geophys. Res., 100*(A5), 7567–7585, doi:10.1029/94JA01825.

[*Taguchi et al.*(2002)] Taguchi, M., S. Okano, T. Sakanoi, N. Koizumi, T. Aso and M. Ejiri (2002), A new meridian imaging spectrogarph for the auroral spectroscopy, *Adv. Polar Upper Atmos. Res., 16*, 99-110.

[*Taguchi et al.*(2004)] Taguchi, M., M. Ejiri, and K Tomimatsu (2004), A new all-sky optics for aurora and airglow imaging, *Adv. Polar Upper Atmos. Res., 18*, 140-148.

[*Taguchi et al.* (2009)] Taguchi, S., K. Hosokawa, A. Nakao, M. R. Collier, T. E. Moore, N. Sato, and A. S. Yukimatu (2009), HF radar polar patch and its relation with the cusp during BY-dominated IMF: Simultaneous observations at two altitudes, *J. Geophys. Res., 114*, A02311, doi:10.1029/2008JA013624.

[*Taguchi et al.* (2010)] Taguchi, S., K. Hosokawa, S. Suzuki, A. S. Yukimatu, and N. Sato (2010), Initial development of HF radar polar patch caused by azimuthal flow burst in the cusp, *J. Geophys. Res., 115*, A05305, doi:10.1029/2009JA014631.

[*Taguchi et al.*(2012)] Taguchi, S., K. Hosokawa, Y. Ogawa, T. Aoki, and M. Taguchi (2012), Double bursts inside a poleward-moving auroral form in the cusp, *J. Geophys. Res., 117*, A12301, doi:10.1029/2012JA018150.

[*Vickers et al.*(2013)] Vickers, H., M. J. Kosch, E. Sutton, Y. Ogawa, and C. La Hoz (2013), Thermospheric atomic oxygen density estimates using the EISCAT Svalbard Radar, *J. Geophys. Res. Space Physics, 118*, 1319–1330, doi:10.1002/jgra.50169.

[*Weber et al.* (1984)] Weber, E. J., J. Buchau, J. G. Moore, J. R. Sharber, R. C. Livingston, J. D. Winningham, and B. W. Reinisch (1984), F-layer ionization patches in the polar cap, *J. Geophys. Res., 89*(A3), 1683–1694, doi:10.1029/JA089iA03p01683.

[*Yin et al.*(2008)] Yin, P., C. N. Mitchell, P. Spencer, I. McCrea, and T. Pedersen (2008), A multi-diagnostic approach to understanding high-latitude plasma transport during the Halloween 2003 storm, *Ann. Geophys., 26*, 2739–2747, doi:10.5194/angeo-26-2739-2008.

[*Zhou et al.* (2000)] Zhou, X. W., C. T. Russell, G. Le, S. A. Fuselier, and J. D. Scudder (2000), Solar wind control of the polar cusp at high altitude, *J. Geophys. Res., 105*(A1), 245–251, doi:10.1029/1999JA900412.

List of publications

Publications Related to the Thesis

Sakai, J., S. Taguchi, K. Hosokawa, and Y. Ogawa (2013), Steep plasma depletion in dayside polar cap during a CME-driven magnetic storm, *J. Geophys. Res. Space Physics, 118*, 462--471, doi:10.1029/2012JA018138.
(The contents of Chapter 2)

Sakai, J., K. Hosokawa, S. Taguchi, and Y. Ogawa (submitted, 2013), Storm-time enhancements of 630.0-nm airglow associated with polar cap patches, submitted to *J. Geophys. Res. Space Physics.*
(The contents of Chapter 3)